IN SITU CELL DEATH MONITORING IN 3D TISSUE CULTURES USING SURFACE ENHANCED RAMAN SPECTROSCOPY

by

Mine Altunbek

Submitted to Graduate School of Natural and Applied Sciences

in Partial Fulfillment of the Requirements

for the Degree of Doctor of Philosophy in

Biotechnology

Yeditepe University

2017

IN SITU CELL DEATH MONITORING IN 3D TISSUE CULTURES USING SURFACE
ENHANCED RAMAN SPECTROSCOPY

APPROVED BY:

Prof. Mustafa Çulha ……………………………

(Thesis Supervisor)

Assoc.Prof. Bahattin Koç ……………………………

Assoc. Prof. Hande Sipahi ……………………………

Assist. Prof. Hüseyin Çimen ……………………………

Assist. Prof. Kaan Keçeci ……………………………

DATE OF APPROVAL: …./…./2017

ACKNOWLEDGEMENTS

ABSTRACT

IN SITU CELL DEATH MONITORING IN 3D TISSUE CULTURES USING SURFACE ENHANCED RAMAN SPECTROSCOPY

Three dimensional (3D) *in vitro* cultures used in drug discovery and tissue regeneration studies can circumvent the difficulties of destructive, labor intensive and high cost *in vivo* studies. However, the conventional techniques to monitor cellular response of 3D cultures depend on fixation and dependently destruction of the 3D structure, which results with loss of the spatially distributed valuable real time information. Surface enhanced Raman spectroscopy (SERS), one of the Raman spectroscopy (RS) modes have recently gained interest in living cell analysis due to the non-destructive and label free detection nature. In this thesis, a SERS based approach was evaluated to monitor *in situ* cell death in 3D cultures. Gold nanoparticles (AuNPs) with 50 nm of average size were used as SERS substrates. The AuNPs were placed into the cells via endocytosis in monolayer culture. Transmission electron microscopy (TEM) images showed that the AuNPs were uptaken and aggregated in endosomal vesicles. Then, the preparation of cells for SERS analysis, optimization of instrumental parameters for spectral acquisition and data processing steps were evaluated in monolayer culture. The cellular response to anti-cancer drugs was monitored from the biochemical changes in endolysosomal vesicles reflected on SERS spectra. Then, 3D spheroid culture was prepared by incubating the AuNP-treated-cells in hanging drop. The prepared spheroids were characterized with bright field microscopy, scanning electron microscopy (SEM) and TEM. When the response of intact spheroid to anti-cancer drugs was analyzed through the depth layers into the spheroids using SERS, the peaks corresponding to endosomal membrane structures, which were collagen, phosphate and C-C vibrations of lipids, were arised around 550 cm^{-1}, 590 cm^{-1} and 710 cm^{-1} in addition to spectral variations in protein structures from the layers closer to the surface of the spheroids due to the induced apoptotic cell death. The results show that SERS-based approach can be used to monitor the efficacy of anti-cancer drugs in 3D spheroid culture depending on the drug penetration rate.

ÖZET

YÜZEYDE ZENGİNLEŞTİRİLMİŞ RAMAN SPEKTROSKOPİSİ KULLANILARAK 3 BOYUTLU DOKU KÜLTÜRÜNDE HÜCRE ÖLÜMÜNÜN YERİNDE İZLENMESİ

İlaç keşfi ve doku rejenerasyon çalışmalarında kullanılan üç boyutlu (3B) *in vitro* kültürler, yıkıcı, yoğun emek gerektiren ve yüksek maliyetli *in vivo* çalışmaların zorluklarını atlatabilirler. Ancak, 3B kültürlerde hücresel tepkiyi izlemek için kullanılan geleneksel teknikler, mekansal olarak dağıtılmış gerçek zamanlı değerli bilginin kaybedilmesiyle sonuçlanan 3B yapının fiksasyonuna ve buna bağlı olarak 3B yapının bozulmasına bağlıdır. Raman spektroskopi (RS) modlarından biri olan yüzeyde zenginleştirilmiş Raman spektroskopisi (SERS), tahribatsız ve etiketsiz algılama niteliğinden dolayı, son zamanlarda canlı hücre analizine kullanımı büyük ilgi kazandı. Bu tezde, SERS'e dayalı bir yaklaşım, 3D kültürlerdeki hücre ölümünü yerinde izlemek üzere değerlendirildi. Ortalama boyutu 50 nm olan altın nanopartiküller (AuNP'ler) SERS substratı olarak kullanıldı. AuNP'ler, tek katmanlı kültürde hücrelere endositoz yoluyla yerleştirildi. Geçirimli elektron mikroskobu (TEM) görüntüleri, AuNP'ler hücre içine alındığını ve endosomal veziküllerde toplandığını gösterdi. Daha sonra SERS analizi için hücrelerin hazırlanması, optimum spektral elde edilmesi için enstrümantal parametrelerin optimizasyonu ve veri işleme adımları tek katmanlı kültürde değerlendirildi. Kanser ilaçlarına hücrelerin yanıtının, endozomal veziküllerdeki biyokimyasal değişikliklerden SERS spektrumuna yansımasıyla izlendi. Ardından, 3B sferoit kültürü, AuNP-almış hücrelerin asılı damla içinde inkübasyonu ile hazırlandı. Oluşan sferoitler, ışık mikroskobu, taramalı elektron mikroskobu (SEM) ve TEM ile karakterize edildi. Bütünlüğü korunan sferoitin derinlik katmanlarına göre kanser ilaçlarına verdiği yanıt SERS ile analiz edildiğinde, indüklenen apoptotik hücre ölümünden dolayı sferoidin yüzeyine yakın tabakalardan endolizozomal zara ait 550 cm^{-1}, 590 cm^{-1} ve 710 cm^{-1} civarında kolajen, fosfat ve C-C lipid piklerin ortaya çıkmasına ek olarak protein yapılarına karşılık gelen piklerde değişikliklere neden olduğu gözlemlendi. Sonuçlar, SERS'e dayalı yaklaşımın, 3B sferoit kültürde bir ilacın etkinliğini ilaç penetrasyon oranına bağlı olarak izlenebileceğini göstermiştir.

TABLE OF CONTENTS

LIST OF FIGURES

LIST OF TABLES

LIST OF SYMBOLS/ABBREVIATIONS

AuNPs	Gold Nanoparticles
DLS	Dynamic Light Scattering
DMEM	Dulbecco's Mordified Eagle Medium
ELISA plate reader	Enzyme-Linked Immunosorbent Assay plate reader
FT-IR Spectroscopy	Fourier transform infrared Spectroscopy
LDA	Linear Discriminant Analysis
NADH	Nicotinamide Adenine Dinucleotide
nm	nanometer
PCA	Principle Component Analysis
PI	Propidium Iodine
RS	Raman Spectroscopy
SEM	Scanning Electron Microscopy
SERS	Surface Enhanced Raman Spectroscopy
SPR	Surface Plasmon Resonance
TEM	Transmission Electron Microscopy
UV/Vis spectroscopy	Ultraviolet/Visible Spectroscopy
WST-1	4-[3-(4-iodophenyl)-2-(4-nitrophenyl)- 2H-5-tetrazolio]-1,3-benzene disulfonate

1. INTRODUCTION

Cell death has an important role starting from the embryonic development to organogenesis, formation of multicellular tissues, and maintenance of cellular function [1-3]. Dead cells are in equilibrium with the live cells to retain normal tissue homeostasis. The distortion of tissue function with either external or internal stress may influence the regulation of live/dead balance in normal tissue homeostasis [4]. The mechanisms of induced cell death can change regardless of cell type including apoptosis, necrosis, and autophagy [5]. Depending on dysregulation of death pathway, particular diseases evolve [4-9]. Therefore, understanding the mechanism of cell death is important to re-modulate the cellular functions and body homeostasis [10]. The prevention of cell death is sometimes a desired goal for the treatment of diseases such as ischemia, stroke, myocardial infarction and neurodegenerative diseases [11, 12] while the promotion of cell death is crucial for the treatment of some diseases such as cancer [13, 14]. Pharmaceutical industry is in an enormous effort to develop new drugs to target a particular cell death pathway for treatment of a specific disease without specific toxicity to the other cells among the millions of potential drugs [15, 16].

The routes of death mechanism distinguish from both morphological changes and biochemical processes inside a cell [5, 17-19]. Apoptosis is a controlled cell death mechanism with well characterized biochemical changes; which are phosphatidylserine (PS) localization at outer surface of cell membrane, mitochondrial membrane permeabilization and release of cytochrome-c, caspase activation, and inter-nucleosomal DNA cleavage. Morphological changes of the apoptotic cell death are distinguished with plasma membrane blebbing, chromatin condensation, nuclear fragmentation and formation of apoptotic bodies [17, 20]. Apoptotic cells are cleared through phagocytotosis by macrophages [21]. Autophagy is also a controlled cytoprotective cell death mechanism induced upon starvation and hypoxia, which is thought to be an alternative way to apoptotic pathway [22-27]. A secondary lipid membrane is formed with lipidation of microtubule associated protein 1 light chain (LC3), which surrounds cytoplasm and intracellular organelles [28]. These membranes combine with lysosomes, where the entrapped intracellular contents are degraded. For necrotic cell death, these processes are known as uncontrollable [29-32]. However, findings also showed that cell death exhibiting

the morphological characteristic of necrosis can be also induced with programmed biochemical processes [33, 34]. During necrosis, permeabilization of mitochondrial membrane and endoplasmic reticulum lumen cause release of Ca^{2+} ions, decrease in amount of ATP, and increase in reactive oxygen species (ROS) production. The activation of proteases and endonucleases damaging cytoskeleton elements and chromatin, respectively, are also the markers of necrosis [5, 35]. Early plasma membrane rupture with the activation of proteases causes the release of intracellular components to extracellular environment and induces an inflammatory reaction, which is detrimental to surrounding cells [30].

Live and dead cells are currently quantified based on the measurement of fluorescent or colored dyes by selectively labeling [36-39]. However, understanding the sub-route of cell death is more critical for development of disease specific therapeutic strategies. The discrimination of cell death mechanisms depends on the monitoring of cell death pathway specific biochemical changes [40, 41]. Fluorescence based methods are sensitive and more intensively used for the analysis. The assessment depends on the measurement of fluorescence signals to figure out the "yes or no" questions, or intensity evaluation or structural and dynamic information from targeted molecules. However, the techniques mostly depend on destruction of cells [42-44]. The limited photo-stability of fluorescence labels can also limit the obtained information from cells [45, 46]. The interaction of tested material with assay dyes or detection system is another issue leading misinterpretation about toxicity [47-50]. In addition, even though it is possible to perform multiple detection using more than one laser source, broad fluorescence emission band of fluorescence dyes restricts specificity of multiplex detection [45].

Vibrational spectroscopic techniques such as Fourier transform infrared (FT-IR) and Raman spectroscopy are intensively investigated for their potential use in molecular biology and medicine. The capability of FT-IR spectroscopy for real time monitoring of cell cycle stages, live and dead cells based on spectral changes in nucleic acid and protein peaks were reported [51-53]. However, interference of water with the absorption of IR light by covering almost all spectral region limits this technique for living systems. Raman spectroscopy is another vibrational technique uses UV, visible or near IR region monochromatic laser source capability of biomolecule detection in native cellular conditions with limited interference from water. This technique relies on the measurement

of the inelastically scattered incident light from the molecules [54]. Using this technique, more than one molecular species in a specimen can be identified from narrow and sharp non-overlapping bands without labeling [55-57]. However, the technique suffers from inefficiently scattered photons. The enhancement can be achieved by bringing molecules into contact or close proximity of plasmonic nobel metal nano structures such as gold and silver, which is called surface-enhanced Raman Scattering (SERS) [58, 59]. The mechanism of signal amplification is attributed to the contribution of both chemical and electromagnetic enhancement which depend on their size, shape and aggregation status of plasmonic nanostructured surfaces [60-62]. The progresses have been made in development of newly advanced substrates and sample preparation methods to obtain better SERS enhancement from biomolecules at low concentrations and even at a single molecule level [63-67].

In recent year, use of the technique for single cell analysis has gained interest. In this approach, a SERS substrate is introduced into cells through endocytosis. The choice and administration of SERS substrate into cells, and adaptation of optical properties of measurement system are crucial to obtain efficient intracellular information without inducing substrate-based toxicity or photo-induced damage. AuNPs are mostly preferred due to biocompatibility and non-toxicity [68-71]. The excitation wavelength for living cell analysis is suggested in the range of 633 to 785 nm to avoid photodamage. In addition, the excitation wavelength in near IR region has better choice to excite the electron system of the aggregated AuNPs by also helping to reduce possibility of auto-fluorescence [72]. The size, shape, surface chemistry, and surface charge of AuNPs influence their intracellular uptake, localization, and aggregation status as well as the enhancement of SERS signals [73-76]. Spherical AuNPs with 50 nm average diameter are demonstrated to be the most effective to enter into cells [76, 77]. AuNPs are uptaken by energy dependent endocytotic pathway and they are commonly entrapped in endosomes unless they are modified with a targeting molecule [70, 78-81]. The modification of AuNP surface with targeting agents may influence their uptake route and localization such as in nucleus, mitochondria or cytoplasm [82-84]. Direct approaches such as microinjection and electroporation are also emerged to internalize NPs in order to increase their aggregation in the cells, and thus SERS enhancement, and to directly target the cytosol by avoiding endosomes [85-88]. Implementation of SERS for living cell analysis has been demonstrated in several reports

monitoring cell cycle and death, death stages and differentiation in *in vitro* monolayer culture [71, 82, 84, 89, 90].

Analysis of cells in 3-dimentional (3D) culture is an immense interest in a variety of applications especially in drug discovery studies to study tumors [91-93]. Tumors are known as a mass of cells formed by uncontrolled proliferation with disorganized vascularization in which oxygen and nutrient cannot be delivered to the cells at the central regions sufficiently in 3D structure. The change in oxygen and nutrient amount causes the formation of different regions including proliferating, non-proliferating, and necrotic cells, which influence the drug metabolism and their stimulating response [94, 95]. The drug penetration rate also changes with cellular response in 3D cultures as well [96, 97].

A range of approaches have been emerged to generate 3D tissue cultures such as spontaneous aggregation in hanging drop [98], non-adhesive plates [99], scaffolds [100] and microwells [101], or microcarrier beads [102]. Depending on employed method, the quantity and homogeneity of 3D cell structure changes. Among them, scaffold free spheroid culture model is superior representing a tumor environment and is commonly used for drug discovery studies [103, 104]. Viability, proliferation and differentiation of cells in 3D tissue structures are monitored and analyzed through their proteins, DNA, and RNA levels by complex and long molecular procedures including freezing and paraffin-embedding techniques coupled with fluorescence or immune-histochemical analysis [105]. The other available techniques used for the analysis are adopted from 2D culture, which cannot be suitable for 3D cultures [40, 106]. The information obtained from 3D culture studies sometimes fails due to low reproducibility and efficiency so as to the morphological characteristics of spheroids such as volume and shape [107]. The compactness and permeability of spheroids can also cause variability in results [107, 108]. In order to decrease the variation among the several reports, the clinically relevant spheroid size is determined between 200 µm and 500 µm with spherical shape without secondary necrosis in the central regions [103]. The pre-selection of spheroids with the suggested characteristics can also diminish data variation [107].

In this thesis, a SERS based 3D culture model was evaluated for *in situ* detection of cell death in a nondestructive and label-free approach. The approach was firstly optimized by analyzing living cells cultured in monolayer. Citrate reduced spherical AuNPs with an

average size of 50 nm was used due to efficient intracellular uptake and SERS activity. HeLa, cervical tumour cell line, was used for the evaluation of SERS based spheroid model. The AuNPs were introduced into HeLa cells by exposing at non-toxic concentration for 24 h in monolayer cell culture. The internalization and localization of AuNPs were monitored using TEM. Then, the experimental parameters such as laser power, objective magnification and adjustment of objective focus were optimized in monolayer cell culture. Once the parameters were optimized, spectral reproducibility was evaluated. Finally, the molecular response of HeLa cells to drug exposure was analyzed at single cell level. Doxorubicin (Dox) and cisplatin, most commonly used anti-cancer drugs inducing apoptosis, were selected for the evaluation. After exposure of the drugs, the cells were collected from culture plate and placed on CaF_2 slide surface. An average of 36-64 spectra were collected from a square area covering almost whole single cell surface. The average of spectra collected from 20 cells was used for interpretation of the molecular changes as a results of drug response with respect to control cells, prepared in the same way but without drug treatment. Then, the capability of SERS analysis in 3D culture was evaluated. First of all, a SERS based 3D spheroid culture was prepared. After 50 nm AuNPs were internalized into HeLa cells in monolayer culture, the cells were collected and incubated in fresh medium containing hanging drop. The formed spheroids were characterized using SEM and TEM for the evaluation of the cell to cell interactions, organization of cells in spheroids, and the distribution and intracellular localization of AuNPs. SERS spectra from the spheroids were collected by scanning a volume of intact and living spheroids. Scanning was started from deepest point of the spheroid possible and gradually decreasing the depth towards the surface with 10µm steps. Then, the performance of SERS based spheroid model on monitoring of drug response was analyzed. After the acquisition of SERS spectra from different depth positions of a spheroid, the spectra from each layer were evaluated separately. Principle component analysis (PCA) was utilized to find the spectral variations within the layers of spheroid and between the control and Dox treated spheroids. Linear discrimination analysis (LDA) was used to monitor discrimination of the PCs of spectra according to both the layers of a spheroid and between the control and Dox treated spheroids.

2. THEORETICAL BACKROUND

2.1. CELL DEATH MECHANISMS

The cells are in balance between live and death in a tissue homeostasis. Any flaw either by intrinsic or extrinsic factors cause disruption of this balance as represented in Figure 2.1. The induction or protection of cell death become a desire to restore the normal cell homeostasis. Although the result is cell death, the induced signaling pathways are resulted in discernible morphological and biochemical changes in cells' homeostasis. The understanding and discrimination of signaling pathway can help with the development of cytotoxic or cytoprotective agents. The approaches recognizing the biochemical changes of cell death and techniques used for identification pave the way for efficiency of treatment.
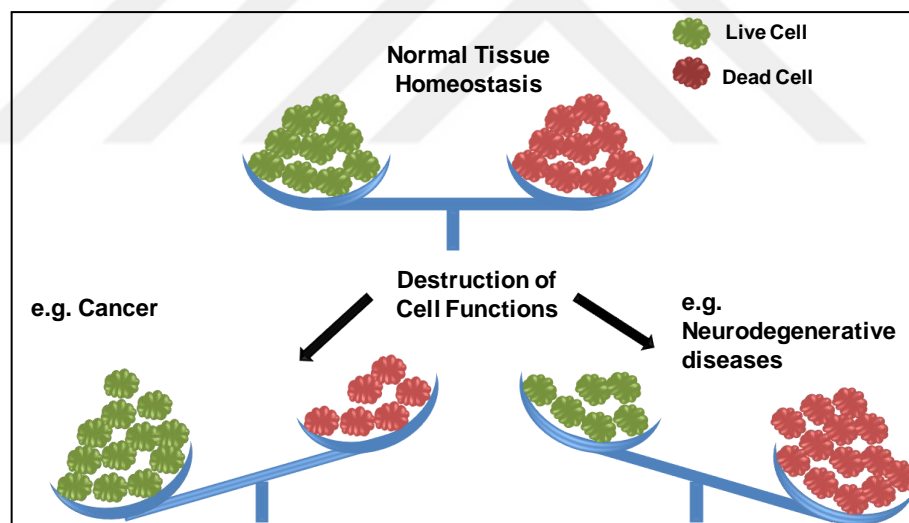
Figure 2.1. Representation of balance of live and death cell in a healthy and diseased tissue**.**

2.1.1. Apoptosis

Apoptosis is a controlled cell death mechanism induced by two different mechanisms, which are intrinsic and extrinsic pathways [19, 40, 109]. The mechanisms are demonstrated in Figure 2.2. The intrinsic pathway is initiated by internal signals due to DNA damage,

endoplasmic reticulum stress or microtubule destruction [110]. The sense of the damage causes activation of serine/threonine kinases, which are ataxia telangiectasia mutated (ATM) or ataxia telangiectasia and Rad3 related (ATR) [111]. Either ATM or ATR phosphorylates and activates the other serine/threonine kinases; check point kinase 1,2 (chk1, chk2). Then, chk1 and chk2 phospharylate serine/threonine residues of p53 protein. P53 binds the promoter region for the pro-apoptotic proteins, which are B cell lymphoma 2 (Bcl-2) homology 3 (BH-3) proteins; Puma and Noxa [112, 113]. BH-3 proteins activate Bcl-2-associated X protein (Bax) and Bcl-2 antagonist or killer (Bak) by inhibiting the anti-apoptotic protein Bcl-2 [114]. Activated Bax and Bak proteins form aggregate in mitochondrial outer membrane and cause the mitochondrial outer membrane permeabilization (MOMP) [115]. When the MOMP is occurred, cell death is irreversibly induced by release of cytochrome c (Cyt-C), which activates apoptotic protease-activating factor 1 (APAF1) and initiation of caspase 9, 3-7 cascade [116, 117].

The extrinsic pathway is initiated by external stimulus of FAS death receptor [118]. The stimulation activates dimerization of FAS-associated death domain (FADD) with FADD adaptor protein, which has free death effector domain (DED) in cytoplasm [119]. DED domain of FADD mount with DED domain of procaspase 8 or procaspase 10 and death inducing signaling complex (DISC) is formed [120]. Then, caspase 8 or 10 is activated. Dimerization of caspase 8 initiates caspase 3-7 cascade and resulted in apoptosis [121].
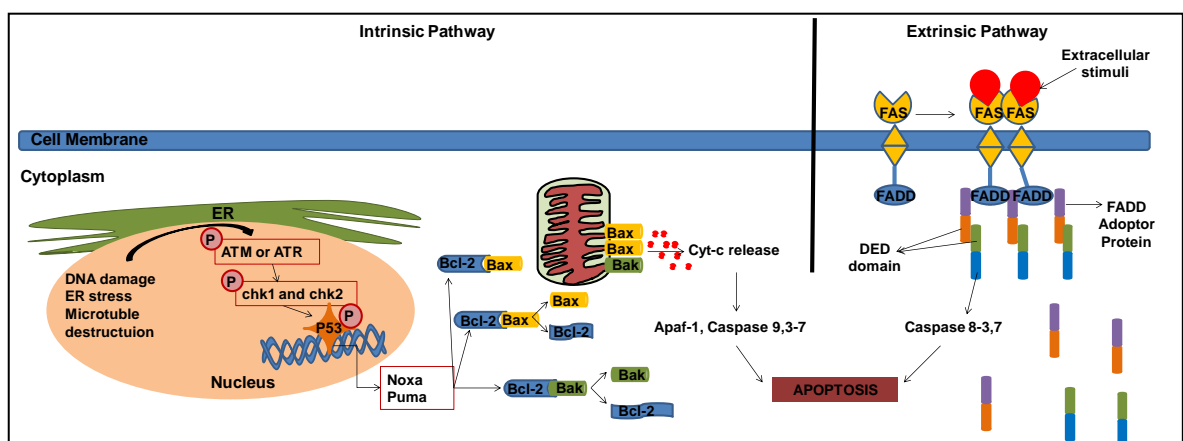
Figure 2.2. Mechanism of intrinsic and extrinsic apoptotic pathways.

Despite different pathways exist, the observable morphological changes are typical for a apoptotic cell including cell shrinkage, cell surface blebbing, nuclear chromatin

condensation, and apoptotic body formation [20]. Schematic representation for the morphological and biochemical changes in an apoptotic cell shown in Figure 2.3.
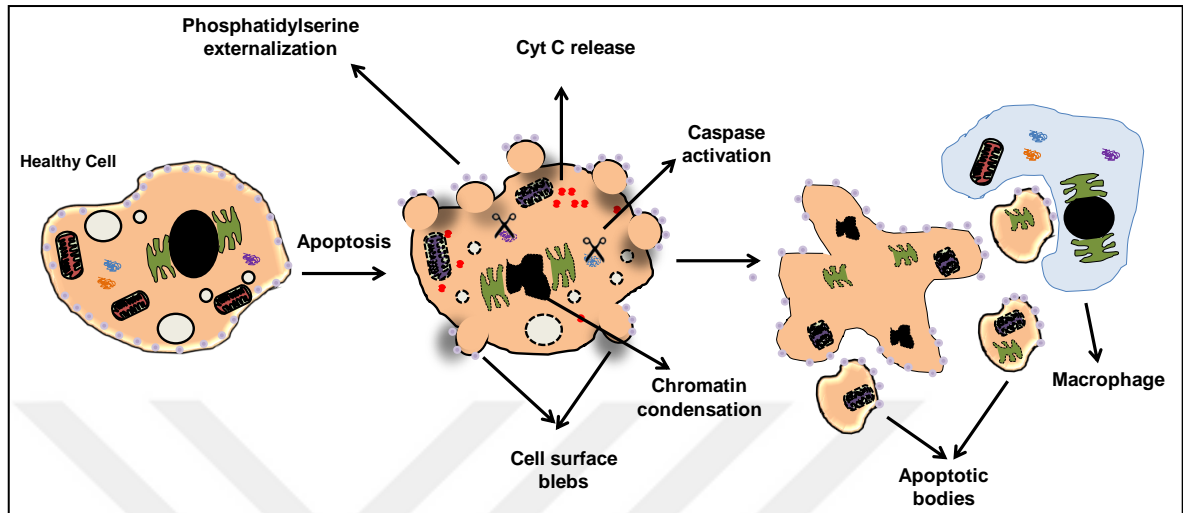
Figure 2.3. Schematic representation for morphological and biochemical changes in an apoptotic cell.

Apoptosis can be detected by monitoring underlying biochemical processes. Table 2.1 shows parameters and techniques used for the apoptotic cell detection. As seen, most of the techniques based on fluorescence measurement. The analysis of MOMP based signals such as cyt-C level, mitochondrial membrane potential, production of reactive oxygen species (ROS) or ATP level are all indicator, but they do not directly reveal the apoptotic cell death [122, 123]. In addition, the analysis of caspase activation cannot differentiate apoptotic cell death [43]. Therefore, the analysis has to be coupled with other apoptosis discriminating factors. Most commonly used discriminating method is Annexin V staining, in which a fluorescent or enzymatic label conjugated to Annexin V protein binds to phosphatidylserine (PS) located on the outer membrane of the apoptotic cells [124]. The monitoring morphological changes such as nuclear condensation, apoptotic bodies, and DNA fragmentation can also be helpful for the discrimination of the apoptotic cell death from the other death mechanisms.

Table 2.1. Parameters and techniques used for apoptosis detection.

Parameters	Technique
Cyt-C release	Transgenic cell lines expressing Cyt-C fused with fluorescent proteins monitored with fluorescence microscopy [125].
	Expression level of Cyt-c by using Western blot analysis.
Mitochondrial membrane potential, ROS	Accumulation of labeling dye into mitochondrial membrane changes with change in the membrane potential [123]. Emission of cell permeable dyes changes with oxidation of dyes [126].
ATP consumption	Determination of ADP/ATP levels by measurement of a phosphorylated product with bioluminescence, colorimetric or fluorometric detection [127-129].
Caspase activation	Monitoring of fluorescent labeled substrates of caspase using fluorescence microscopy or flow cytometry [43, 123, 130].
	Analysis of protein cleavage using Western blot analysis.
Detection of anti-apoptotic proteins	Expression level of Bcl-2 family proteins using Western blot analysis [131].
Nuclear condensation	Monitoring of nucleus by staining with propidium iodide or 4´,6-diamidino-2-phenylindole (DAPI) with fluorescence microscopy, flow cytometry.
DNA fragmentation	Detection with terminal deoxynucleotidyl transferase mediated dUTP nich end labelling (TUNEL) by fluorescence microscopy or gel electrophoresis [43]
PS externalization	Monitoring of fluorochrome conjugated Annexin V, a placental protein specifically binds to PS using fluorescence microscopy or flow cytometry [124].

2.1.2. Autophagy

Autophagy is cytoprotective self-eating mechanism of cells by lysosomal degradation of cytoplasmic contents under stress conditions such as starvation and infection [22-25, 27]. Deficiency in development, differentiation or any neurodegenerative processes can also be the causes of induced controlled autophagic cell death [132, 133]. Autophagy is initiated with the inhibition of mTOR (mammalian target of rapamycin) complex 1 (mTORC1)-kinase activity controlling cell growth and protein synthesis in the cell. After inactivation of mTOR, serine/threonine kinases are activated and control the sequestering of cytoplasm and organelles by a double-membrane vesicle called autophagosome [134]. The activated proteases make microtubule-associated protein light chain 3 (LC3-I) free in cytosol [28]. Then, LC3-1 is lipidated with conjugation of phosphatidylethanolamine (PE) (LC3-II) and

join to the autophagosome. Autophagosome fuses with lysosome forming autolysosomes that degrade contents in the vesicle. The degraded components such as amino acids are prepared to be reused by the cells. Figure 2.4 shows schematic representation for the morphological and biochemical changes in an autophagic cell.
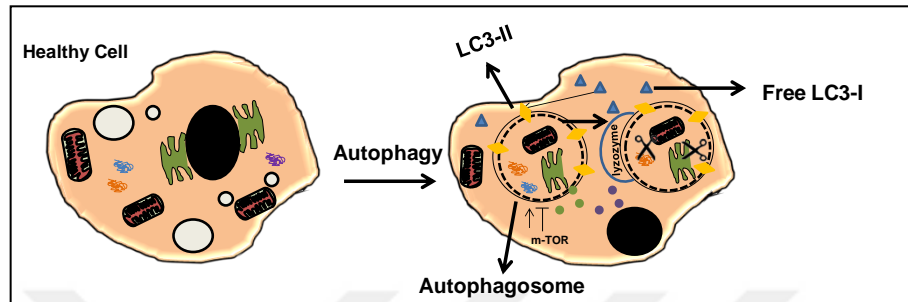
Figure 2.4. Schematic representation for morphological and biochemical changes in an autophagic cell.

Autophagic cell death mechanism can be identified by analysis of expression level of LC3-I and LC3-II. Another indicator is to monitor expression level of the autophagy adaptor protein, p62/SQSTM1, that identifies cytoplasmic contents to be degraded by autophagosomes, and facilitates their uptake and proteolysis by binding to LC3-II [135]. Table 2.2 shows the detection and analysis techniques for autophagic cell death.

Table 2.2. Parameters and techniques used for autophagy detection.

Parameters	Detection&Analysis Technique
Lipidation of LC3-I to LC3-II	Expression level of LC3-I/LC3-II proteins using Western blot analysis [136].
P62 protein	Expression level of p62 protein using Western blot analysis [135].
Measuring the activity of autophagy regulator kinases (mTOR, ULK1, PI3K)	Analysis of phosphorylation levels using enzymatic assays or immunoblot analysis [5, 137, 138].
Morphological determination	Monitoring of autophagosomes using transmission electron microscopy.

2.1.3. Necrosis

Necrotic cell death can be induced with two different modalities, which are primary and secondary necrosis [33]. Primary necrosis is known as induced due to the accidental injury

of the cells [139]. However, the modality of programmed necrosis is also present, which is known as necroptosis [140]. The increase in cytosolic Ca^{2+} level and activation of non-caspase proteases are the descriptive biochemical changes observed in primary necrosis. Some of the biochemical changes in necrotic cells show similarities with apoptosis which are lysosomal or mitochondrial membrane permeabilization, decrease in ATP production and ROS production [141]. Secondary necrosis appears when a phagocytic system is absent at final stage of apoptosis [142, 143]. This type of necrosis is most commonly observed in the cell culture system, which results in release of intracellular content due to the rupture of plasma membrane. The morphological changes in a necrotic cell are differentiated from apoptotic cell [5, 40]. The swelling of cell and cytoplasmic organelles and loss of plasma membrane integrity are the characteristic morphological changes observed in necrotic cells. DNA morphology remains same until later stages. Figure 2.5 represents the morphological and biochemical changes in a necrotic cell.
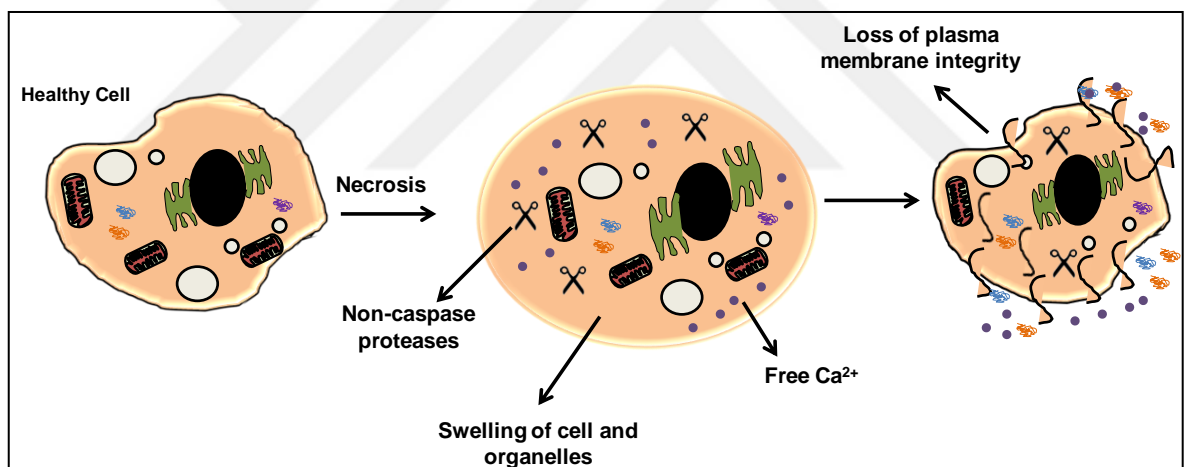
Figure 2.5. Schematic representation for morphological and biochemical changes in a necrotic cell.

To assess necrotic cell death, end point ELISA based approaches have been established to monitor the specifically released proteins and enzymes from necrotic cells, which are non-histone chromatin binding protein (HMGB1) and peptidylprolyl isomerase A (CPYA), respectively [144, 145]. In addition, agarose gel electrophoresis is used to monitor high molecular weight (>50kbp) and nucleosome size (200 bp) of DNA since DNA integrity remain same in necrosis. Another approach is established to discriminate necrosis from apoptosis by flow cytometric detection of propidium iodide negative cells versus Annexin V positive apoptotic cells [139].

Table 2.3. Parameters and techniques used for necrosis detection.

Parameters	Detection&Analysis Technique
HMGB1.	Monitoring of GFP or RFP fused HMGM1 [144].
CPYA released early in necroptotic cells.	CYPA binding and enzymatic assays dependent ELISA kits used for quantitative analysis [146].
Discrimination of primary necrosis and apoptosis.	Annexin V-positive/propidium iodide-negative cells [139].
Detection of DNA integrity.	Gel electrophoresis.

2.1.4. Doxorubicin and Cisplatin: Action of Mechanisms

Doxorubicin is a routinely used anti-cancer drug, produced by *Streptomyces peucetius var. caesius* as a secondary metabolite [147]. It is used in the treatment of ovarian, breast, lung, gastric, thyroid, non-Hodgkin's and Hodgkin's lymphoma [148]. Doxorubicin induces apoptotic cell death and G2/M phase cell cycle arrest. Apoptosis is initiated by two different mechanisms. First one depends on the intercalation of Doxorubicin into DNA, which disturbs DNA repair by interapting the function of topoisomerase-II. The second one depends on the release of ROS damaging the cell membrane, DNA and proteins.

Cisplatin is one of the platinum complexes used in the treatment of many cancer types such as cervical, ovarian, prostate, lung and breast. [149, 150]. Cisplatin induces apoptotic cell death by both intrinsic and extrinsic pathways. In the intrinsic mechanism, cisplatin distrupts DNA replication and transcription by binding guanine bases in DNA structure. In addition, it interferes with the pro-apoptotic Bcl-2 family proteins, causes MOMP [151]. In the extrinsic pathway, cisplatin affects the calcium signaling and death receptor signaling [152]. Cisplatin disturbs the function of all cells regardless cell cycle phase. The action of cisplatin depends on the cell type and exposure concentration.

2.2. RAMAN SPECTROSCOPY (RS)

Raman spectroscopy (RS) is a vibrational technique based on the Raman effect (scattering) named after its discovery by Dr C.V. Raman in 1928 [153]. RS has been intensively investigated and has become a non-destructive method for structural analysis of organic and inorganic materials since 1930s [154]. After the discovery of monochromatic radiation (lasers) in 1960s, the RS based studies were accelerated. [155]. Basically, Raman effect is described as inelastic scattering of radiation upon interaction with molecules. It is used to obtain structural information from molecules by using the frequency of inelastically scattered photons of excited monochromatic light, which shifts with the characteristic energy of molecular bond vibrations [156].
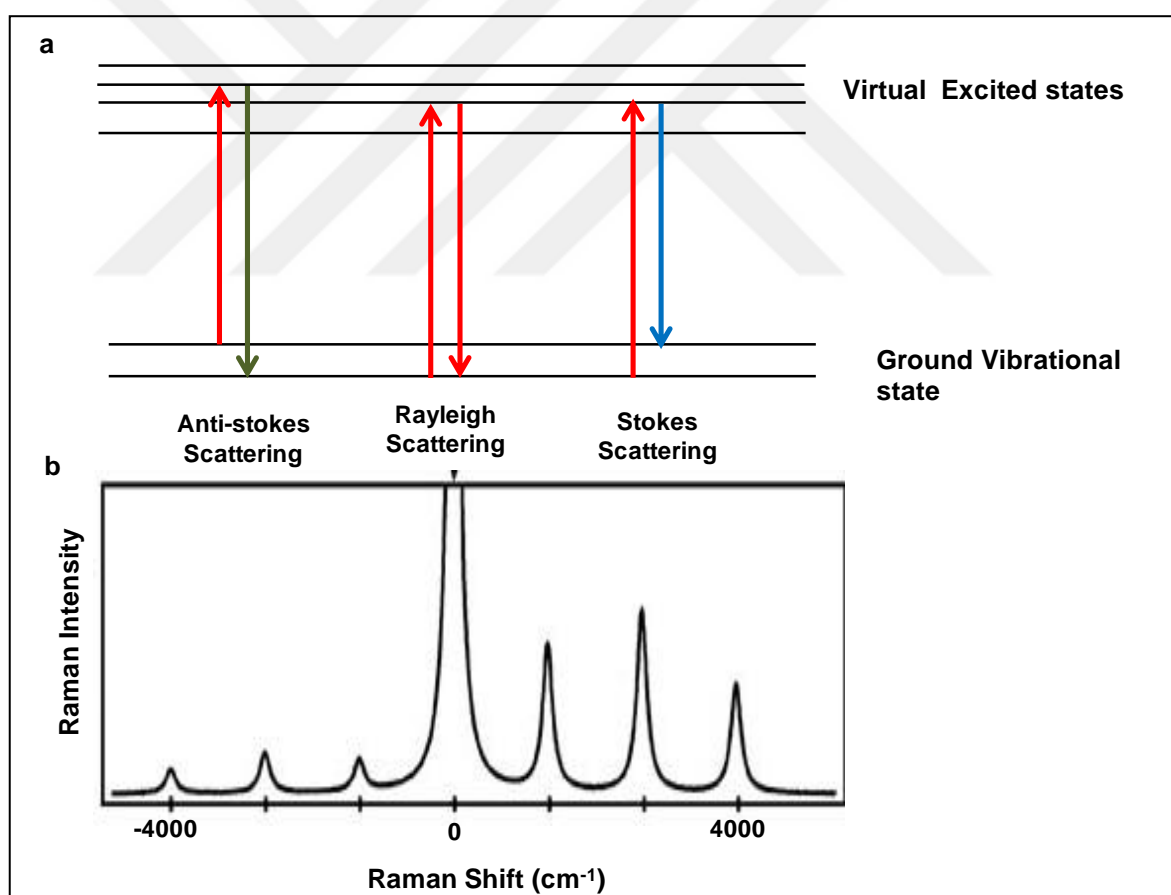
Figure 2.6. (a) Representation of Rayleigh scattering, stokes Raman and anti-stokes Raman scattering energy transfer models and (b) a typical stokes and anti-stokes Raman scattering [157].

RS uses UV, visible or near IR region wavelength laser sources to obtain qualitative and quantitative information in a Raman spectra recorded in 10-4000 wavelength shift (cm^{-1}). The scattered photons can be at lower energy than incident light called "stokes shift" or at higher energy called "anti-stokes shift". If the energy of scattered photons have same energy with the incident light, the phenomenon is called as Rayleigh scattering, which was discovered in 1871 by Dr L. Rayleigh but phenomenon was realized and described later by Dr. A Smekal in 1923 [158]. Figure 2.6-a shows representation of translation of energy levels in Rayleigh, and stokes and anti-Stokes scattering. RS uses the wavenumber of stokes or anti-stokes lines in which the Rayleigh light is rejected, to obtain information about vibrational energy of the molecules depending on chemical structures. The obtained spectrum is demonstrated as Raman intensity vs Raman shift (cm^{-1}) as represented in Figure 2.6-b. Since Raman bands obtained with stokes shifts are more intense than the bands obtained with anti-stokes shifts, the stokes shift is mostly used for the analysis.

RS has been routinely used in various fields including physics, chemistry and biology. Due to its non-destructive, label free and rapid analysis features, RS has also become an attractive technique for analysis of biological samples. The applicability of RS in many biological applications was demonstrated by monitoring molecular constituents such as proteins, nucleic acids, lipids, and carbohydrates [56, 159]. For example, RS is employed for easy, rapid and reliable detection and identification of microorganisms which are important for environmental applications, food technology, and medical diagnostics [160, 161]. The identification of microorganisms depend on monitoring of the biochemical differences in cell wall, endospores constituents or metabolic activities of microorganisms. RS promises to reduce identification time through easy sample preparation with shortened cultivation time due to the identification in small populations [162, 163]. Microorganisms in complex biological samples can sensitively and specifically be identified and discriminated from the established referance data with statistical analysis algorithms [163, 164]. For example, 66 strains of *Bacillus* were discriminated with 88-100 % accuracy from Raman spectra of their endospores [165].

Another promising application of RS is monitoring of cancer diagnosis and prognosis. The potential use of RS for cancer diagnosis and prognostics, malignant transformation or differentiation or as a tool for evaluating new therapies was also demonstrated [166-169]. The biochemical changes as a result of disease progress reflected on Raman spectra is used

for detection of abnormalities. Malignant and healthy tissues were successfully discriminated and classified for various of cancer types from *in vitro* and *in vivo* samples using RS [170-177]. Recently, an endoscopy RS system was also used as a secondary technique to autofluorescence bronchoscopy (AFB) in combination with white light bronchoscopy (WLB) for the analysis of lung lesions *in vivo* [178]. High grade dysplasia (HGD) and malignant lung lesions were differentiated from benign and normal lung tissues 90% sensitivity and 65% specificity. It was indicated that the combination of RS with these two techniques increased the diagnosis of HGD and malignant lesions.

2.2.1. RS in Living Cell Analysis

RS has also been adopted for living cell analysis to collect valuable information real time [55]. Any changes in the spectral pattern with respective to pre-treatment conditions were attributed to the changes of biochemical composition in different cell cycle phases, death and differentiation of cells in monolayer culture [179, 180]. For example, in an *in vitro* study, the spectral changes corresponding to phosphodiester bonds and nitrogenous bases of DNA structure were assigned to cell death signals [179]. In addition, the decrease in phenylalanine and amide III bond peaks, corresponding to protein random coils was indicated as a sign of death cells. In another study, RS was used to characterize necrotic cells based on the time dependent changes in biochemical composition by Kunapareddy *et al*. in 2008 [181]. The significant decrease in relative intensity of the peaks corresponding to lipids, RNA compared to DNA and proteins were used for interpretation. The changes were attributed to the lipid and cytoplasmic content degradation occurring initial step of necrosis. The changes in DNA and protein structures occurred at later stages of necrosis were also reflected on Raman spectra demonstrating sensitivity of the technique. Apoptotic cell death was also monitored by tracking the dynamic release of Cyt-c from the mitochondria using RS [182]. Normally, when Cyt-c is released into the cytosol, it is in reduced form, then oxidized. After cells were induced to apoptosis with Antinomycine D, Raman spectra recorded in 5 min interval during 7 hours showed differences due to the reduced and oxidized forms of Cyt-c. When the experiment was repeated by labeling the reduced and oxidized Cyt-c with Raman active dye, reproducibility and reliability of the spectrum decreased indicating the efficiency of RS in label free detection [182].

The spectral data from living cells compose of multiple variations. The relations between multiple changes in Raman spectra are analyzed with utilization of multivariate statistical analysis methods. The integration of statistical analysis methods to RS technique enable to find the major changes in a large dataset. In a study, multivariate statistical analysis methods, which were principal component analysis (PCA) and linear discriminant analysis (LDA), were utilized the Raman spectra of A549 cells for detection of toxicity of agents by monitoring cell death [183]. The cells treated with ricin (assassination in London, in 1978) and sulphur mustard (used in WWI), which were known toxic materials to the living organisms, were analyzed with RS. The statistical analysis discriminated not only the small changes within large spectral dataset depending on not the type and concentration of toxic agent inside the cell, but also necrotic and apoptotic cell death pathways, compared to initial cellular responses. The other multivariate analysis methods also effectively and specifically provided discrimination and classification of living, apoptotic and necrotic cells [184-186]. For example, viable, apoptotic (according to sub-stages; early or late) and necrotic cells were determined using Raman spectra from single cells in correlation with fluorescence labeling, which were classified with support vector machine (SVM) multivariate analysis in another study [186].

2.2.2. Limitations of RS

As seen, a set of study using RS showed that it is a robust tool for the analysis of viable and death cells. However, some of the technical parameters limit the use of RS in cell analysis. Although NIR laser is utilized for spectral acquisitions to prevent damage to cellular contents, it decreases the scattered of Raman signal from the biomolecules. In order to increase the scattering intensity, the UV or visible range wavelength lasers with high laser power of long measurement time can be used. However, heating of cells with multi-photon excitation damages the biological molecules limiting use of technique in living cell analysis. For example, mouse epithelial cells (MCE-12 cells) were exposed to 488 nm with 5 mV laser power [187]. After 10 and 20 min, cell death was observed due to the photochemical reactions occurring in cytoplasm. In another study, no change in cell viability and morphology was observed after MLE-12 cells were exposed to 785 nm at 115 mV laser-power for 40 min. The alternative RS based techniques were developed to observe effective and enhanced spectra from living cells and tissues such as Coherent anti-

Stokes Raman scattering (CARS) [188-193], Confocal Raman Microscopy [194-199], Kerr-gated Raman Spectroscopy [200-202], Shifted excitation Raman difference spectroscopy (SERDS) [203-205], Spatially Offset Raman Spectroscopy (SORS) [206-208], Surface-enhanced SORS (SESORS) [209-212], Stimulated Raman Scattering (SRS) [213], Transmission Raman Spectroscopy [172] and Surface enhanced Raman Scattering (SERS).

2.3.   SURFACE ENHANCED RAMAN SCATTERING (SERS)

Surface enhanced Raman scattering (SERS) is a sensitive technique, in which Raman signal from molecular vibrations is amplified by placing molecules near or close vicinity to plasmonic noble metal nanostructures such as gold and silver. The phenomenon was surprisingly observed when Raman spectra were collected after pyridine was placed on a roughened silver electrode by Fleischmann *et al.* in 1974 [58]. The enhancement in RS in the order of 10^5 –10^6 was confirmed later by Van Duyne group and Creighton group [59, 214]. The enhancement mechanism is now commonly explained with electromagnetic and chemical enhancements [60-62]. Electromagnetic enhancement provides the largest contribution, which relies on oscillation of the conduction electron cloud of plasmonic nanomaterials known as localized surface plasmon resonance (LSPR) upon excitation with an incidence electromagnetic field, which enhances local electromagnetic field called as "hot spots" [215-217]. The characteristics of frequency and enhancement depend on the material type, its physicochemical properties such as size, shape, surface chemistry and aggregation status and surrounding medium [218-220]. Chemical enhancement is considered a lesser contributing component of the enhancement, which occurs due to the chemical interaction of molecules with nanostructured surface, or changing the molecular polarizability by the formation of charge-transfer complex [58, 59].

The enhancement depends on the properties of SERS substrate and optical settings of instrument [60, 221, 222]. Due to the stability, Au and Ag colloidal NPs are commonly used noble metal nanoparticles to enhance the molecular vibrations [223]. The size, shape and aggregation status determine plasmonic property which is between 520 nm and near IR wavelength range for AuNPs and 350-550 nm range for AgNPs [216]. The selection of SERS substrate with proper properties is also important for the detection sensitivity. A

roughened surface is indicated as a good SERS substrate candidate since they can create greater hot spots with reproducible spectra. The concentrated or aggregated particles also yield higher enhancement and increase sensitivity of detection since as represented in Figure 2.7, the enhancement factor increases as particles come closer [224]. Affinity of molecules on substrate is another factor influencing sensitivity of detection. Therefore, in order to increase sensitive and selective detection of a targeted molecule, surface of the SERS substrate can be modified with agents such as antibody, aptamers. With the advancements in substrate properties for SERS, the amplification of Raman signals amplified with an aspect of 10^6-10^{16} [225-228]. The selection of excitation wavelength within the range of plasmon resonance of substrate provides efficient enhancement.The enhancement can also be improved by using an excitation wavelength that a target molecule absorbs, which is called resonance enhanced Raman Spectroscopy (RRS). The combination of RRS with SERS can further increase the detection sensitivity of targeted molecule [229].

However, un-controlled aggregation of particles limits the reproducibility and reliability of the detection, which are primary requirements to be used in analytical techniques. A highly ordered immobilized nanoparticles on a surface have been developed to increase the density of the hot spots and sensitivity of detection [229]. As seen, a variety of colloidal and non-colloidal substrates was investigated to increase sensitivity, selectivity and reproducibility of SERS detection systems and today it is possible to detect the molecules in single molecular level [63-67]. There is wealth of available information in literature and one can gain in depth information by consulting to the following books and publications [60, 224, 230, 231]. Only a summary of the technique and important reports pertaining to this thesis is provided here.
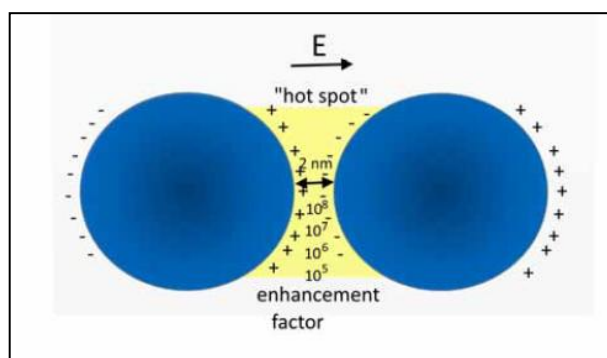
Figure 2.7. Systematic representation of hot spot in interparticle regions [224].

2.3.1. SERS Spectroscopy for Living Cell Analysis

Due to non-destructive and label-free detection nature, SERS has became a powerful tool for the interrogation of living cell function [232, 233]. Two different approaches are used for the understanding of intracellular information. The first approach uses SERS substrate modified with a reporter molecule, whose structural characteristics are used for the detection such as pH or oxidative states [81, 234, 235]. This indirect detection approach is named as "labeled SERS". However, the second approach called as "label-free SERS" provides intrinsic structural information of molecules close in the vicinity to the SERS substrate [78, 82, 89, 236].

The application requires adaptation of the SERS parameters for living cell analysis without interrupting cellular integrity. The cells possess a complex molecular environment containing many organelles enclosed with phospholipid membranes. Since SERS spectra are obtained from the molecules close vicinity to the substrate, one of the important parameters to be considered in living cell-SERS analysis is the selection of SERS substrate with suitable size, shape and surface properties providing high enhancement, nontoxic to living cells and stable in biological environment. The localization of substrates in cells has also important role for the obtained spectral information. The interpretation of spectral changes without knowledge of intracellular location of substrates may cause misleading. Therefore, the delivery of substrate and its intracellular localization are crucial [69]. The delivery mechanism also plays important role in the intracellular destination of NPs. The NPs can internalize by endosomal uptake, which needs long incubation time for uptake and aggregation [70] or by microinjection or electroporation to directly target the cytoplasm, which takes less than one minute [85-88].

Nabiev *et al.*was the first investigated living cell SERS analysis in 1991 [237]. In that study, AgNPs were introduced into the cell and the interaction of anti-cancer drug (Doxorubicin-Dox) with living cancer cells was monitored upon excitation with 514 nm laser wavelength. The obtained spectra were differentiated the localization of Dox in the nucleus or cytoplasm. Kneipp *et al*. demonstrated the suitability of AuNP for the use in living cell SERS studies due to the non-toxicity and providing effective electromagnetic enhancement in near IR region, in 2002 [70]. They selected particle size between 20-60 nm range due to efficient intracellular uptake and higher SERS enhancement of the aggregates

[77, 238]. It was demonstrated that 60 nm AuNPs were internalized into cells via endocytosis and formed aggregates without disturbance of cell viability after 24 h exposure. SERS spectra were obtained from the regions where AuNPs were aggregated. The distinct SERS spectra were obtained from the different regions of cells, which was attributed to heterogeneity of molecules in a single cell. From these observations, spherical AuNPs smaller than 100 nm size was recommended for living cell SERS studies. Since the electromagnetic enhancement is controlled by AuNP aggregates, understanding the role of intracellular AuNP aggregation in living cell-SERS experiments were further investigated by the same group by evaluating the relation between the particle uptake, clustering time and changes in the enhancement of SERS spectra in 2008 [79]. After the cells were treated with AuNPs for 30 min or 60 min (pulse-times), AuNPs containing cell culture medium was replaced with fresh medium and SERS spectra were collected in different time interval during 3 hours (chase-times) in the study. During evaluation, the spectra showed drastic changes which was associated with the changes in both biochemical structures during endocytosis and AuNP-aggregation status. Kawata's group also demonstrated the use of AuNPs in living cell SERS analysis in the same years [236, 239-241]. They performed SERS measurement by tracking the movement of AuNPs using dark field microscope just after addition into the culture plate, which demonstrated capability of SERS to monitor the time-resolved, temporal and spatial changes depending on the NP position. From these observations, it was concluded that SERS signals were sensitive both the biochemical environment and the aggregation status of the NPs in time dependent manner.

Huefner *et al*. monitored endocytic trafficking [242]. In the reported study, distinct spectra were observed from endosomes and lysosomes by controlling the distribution of AuNPs in cells applying a similar AuNPs pulse-depletion approach without labeling This approach enabled to monitor structural changes upon degradation of proteins, lipids and nucleic acids and pH on the SERS spectra. In another study, a labeled approach was used to monitor pH changes in endosomes by Jaworska *et al.* [235]. SERS based pH probe was designed by modification of AuNPs surface with 4-mercaptobenzoic acid (AuNPs-MBA). A pH calibration curve was plotted from the SERS spectra of AuNPs-MBA at 1420 cm^{-1} and 1720 cm^{-1} corresponding to the COO^{-} symmetric stretching and C=O vibrations in the carboxyl group, respectively. The changes in the peak intensities showed a linear response

in 5 and 9 pH range. After AuNPs-MBA probe was introduced into the cells, intracellular endosomal pH was predicted from the pH calibration curve.

AuNPs entrapped into endosomal vesicles inside the cell limits the interrogation of molecular changes from other locations such as in cytosol, nucleus or mitochondria. However, it is possible to obtain spectral information from the other intracellular location by the decorating the surface of plasmonic materials with a targeted moiety, which specifically directs them towards the specific intracellular location. For example, El-Sayed's group developed a plasmonic-Enhanced Raman spectroscopy approach by targeting the AuNPs in nucleus [71, 89, 90, 243-247]. They used spherical, rod and cube shapes of AuNPs in a number of studies in which the AuNPs were firstly coated with poly-ethylene glycol (AuNPs-PEG) to increase stability and to reduce non specific binding of proteins. Then, AuNPs-PEG was modified with RGD (cell penetrating peptide) to target integrins on cell surface to increase intracellular uptake. Finally a nuclear localization signaling (NLS) peptide was attached to target NPs into nucleus, where the changes in molecular structures due to cell cycle, cell death upon drug treatment or photothermal therapy or the dynamic of cancer drug efficiency were effectively monitored using SERS. In the approach, the cells were incubated with fresh serum free medium after AuNP-treatment in order to synchronize the cells in G1 phase to attain a uniform environment around the NPs and to prevent cell cycle phase associated spectral changes. In another study, Huefner *et al.* used also NLS modified AuNPs to characterize the undifferentiated and differentiated neural cell types through SERS imaging [82]. Compared to El-Sayed's reports, the cells were incubated with the modified AuNPs for 72 hours to provide better aggregation of AuNPs in nucleus. The protein peaks in different positions on SERS spectra were obtained from two different neural cells lines. According to PCA, both cells were statistically differentiated. This study suggested that different cell types could be characterized by monitoring cell nucleus using SERS.

With the progresses in nanotechnology, new approaches for the development of the novel SERS substrate for living cell analysis has been emerged. Since the intracellular delivery of the plasmonic NPs is crucial for the SERS information, gold (Au–Magnetite) and silver nanoparticles (Ag-Magnetite) were linked with magnetite particles to increase the intracellular uptake of particles with presence of magnetite by Büchner *et al.* [248]. It was demonstrated that the uptake of Au–Magnetite and Ag-Magnetite increased two or three

times compared to pure AuNPs and AgNPs. However, the intracellular spectra obtained from Au–Magnetite and Ag-Magnetite were different from the pure AuNP and AgNPs due to the difference of the adsorption of biomolecules on the different composite nanostructures. In another study, AgNPs with a fluorescence dye embedded silica spheres (F-SERS dots) were modified with Annexin-V and antibodies recognizing the BAX/BAD proteins to monitor apoptotic cells [249]. Annexin-V conjugated F-SERS dots specifically bound to PS receptor while the intracellular BAX and BAD proteins were selectively recognized by the antibody conjugated F-SERS dots. From the SERS spectra, the distribution of BAX and BAD proteins in cells could be detected. With this approach, the advantages of SERS over immunohistochemistry was demonstrated, which is a destructive technique with long procedure and difficult to detect different proteins at the same time.

The non-colloidal substrates were also fabricated for live cell analysis [250-253]. In a study, cells were seeded on silicon wafer decorated by AgNPs to monitor apoptotic cell death [250]. The sensitive and reproducible SERS spectra corresponding to condensation and fragmentation of DNA structure were observed from the cells in a time dependent manner during apoptosis. In another study, El-Said *et al*. deposited AuNPs on ITO surface in a highly ordered structure in order to escape from the variations arising from the non-uniform arrangement non-colloidal substrates [251]. The SERS spectra of the cells seeded on the prepared substrate were effectively discriminated the cells types, death cells from viable cells and cell cycle phases. In another study, a mechanical trap was decorated with gold nanostars [252]. When cells captured in the mechanical trap, cell-surface contacting with gold nanostars provided 3D spectral information from the cell surface lipids and proteins without any perturbation. In a different approach, SERS enabled nanopipettes were designed by coating 100-500 nm glass capillary tip with AuNPs in a fixed orientation [253]. The probing SERS nanopipette into a single cell enabled *in situ* cell analysis by tracking in nanoliter volume.

The capability of SERS in living cell analysis is clear with a variety of colloidal and non-colloidal based substrates. The attempts for development of novel SERS substrates are still in progress to obtain efficient and detailed SERS information from living cells in real time.

2.4. AIM OF THE THESIS

In vitro 3D spheroid cultures are more realistic tissue mimicking structures for drug discovery studies. The lack of non-destructive analytical tools for *in situ* analysis of living cells in 3D environment results with the loss of valuable biochemical information confined in a spatial arrangement and limits the continuous monitoring. In this thesis, a label free SERS based approach was evaluated to monitor cell death in 3D spheroid culture in a non-destructive manner.

3. MATERIALS AND METHODS

3.1. CHEMICALS AND MATERIALS

Dulbecco's Modified Eagle's Medium (DMEM), Fetal Bovine Serum (FBS) and Trypsin-EDTA (0.25 per cent) were obtained from Sigma-Aldrich (Germany). Phosphate Buffered Saline (PBS) and Penicillin-Streptomycin (10,000 U/mL) were purchased from Gibco (UK). WST-1 Assay (Roche Diagnostic GmbH, Germany), Annexin V-FITC-/PI (Calbiochem, Germany) were purchased to monitor viable and death of cells. Glutaraldeyde and tri-sodium citrate ($C_6H_5Na_3O_7$) were purchased from Merck Millipore (Germany). $HAuCl_4 \cdot 3H_2O$ was purchased from Sigma-Aldrich (Germany). Tissue culture flasks (25 cm^2, 75 cm^2), 12 and 96 well plates, Falcon tubes (15 ml), serological pipettes, were purchased from TPP (Switzerland).

3.2. METHODS

3.2.1. AuNPs Synthesis

AuNPs were synthesized by citrate reduction method [254]. Briefly, 10 mg gold (III) chloride trihydrate in 100 mL dH_2O was heated until boiling with continuous stirring at 1000 rpm. Then, 0.8 mL of one per cent tri-sodium citrate was added into the boiling solution. The solution was kept boiling for 15 min. The synthesized AuNPs were characterized using UV/Vis spectrometer (Lambda 25, Perkin Elmer) and dynamic light scattering (Nanozetasizer, Malvern).

3.2.2. Cell Culture

Human cervical cancer cells (HeLa), Human Umbilical Vein Endothelial cells (HUVEC), U87MG and U373MG glioblastoma cell lines were grown in DMEM supplemented with

10 per cent FBS and 100 units/ml penicillin, 100.0 mg/ml streptomycin and incubated at five per cent CO_2 supplied 37 °C incubator.

3.2.3. Cell Viability and Cycle Evaluation

7500 HeLa cells per well were seeded in a 96-multi-well plate and incubated for 24 h to allow the cells for attachment. The cells were treated with 1.6×10^{15} of 50 nm AuNPs in a mL cell culture medium as reported previously by our research group [255]. After 24 h treatment, the AuNP-containing medium was replaced with fresh medium. Then, the cell viability was evaluated for 24, 48 and 72 h post-treatment times by measuring the mitochondria activity using WST-1 assays. The cells were treated with Dox (2.5, 5, 10 and 20 μM) and cisplatin (0.25, 0.5, 1 and 2 mM) to find effective toxic concentrations.

The cell cycle function of HeLa cells was also analyzed for 24, 48 and 72 h post-treatment times with the AuNPs. Briefly, after cells were seeded in a 24-multi-well plate, the treatment of cells were performed with the same concentration of the AuNPs. The cells were fixed with 70 per cent ice-cold ethanol at -20°C for overnight. After fixation, the cells were permeabilized with 0.1 per cent Triton X-100 for 30 min at room temperature. Then, the cells were incubated with 300 μg/mL of RNase in 1× PBS at 37°C for 30 min. Finally, the cells were stained with 5 μg/mL of propidium iodide (PI) and analyzed using flow cytometry (Guavo® easyCyte, Merck-Millipore).

3.2.4. Preparation of SERS Based 3D Spheroid Culture

SERS based 3D spheroids culture was prepared using hanging drop method in two steps. First, the cells were seeded in 24 well plate and incubated with an approximately 1.6×10^{15} of 50 nm AuNPs in one mL of DMEM for 24 h in monolayer culture. Then, the cells were detached from the surface and 250, 500 or 1000 cells in 20 μl DMEM were dropped on a lid of cell culture plate, which was inverted on the top of plate. 1×PBS was placed into the bottom of plate to provide humidity and to prevent the drops from drying. After 72 h incubation period, the spheroids were transferred into non-adherent-PDMS coated 24-well plate, where they were treated with 5 μM of Dox for 24 h.

3.2.5. TEM and SEM Imaging

For the preparation of cells for electron microscopy, the monolayer and 3D spheroid cultures were washed with 1×PBS and prefixed in 2.5 per cent (v/v) gluteraldehyde at 4°C. Afterwards cultures were washed with PBS. For transmission electron microscopy, post-fixation step was performed with one per cent OsO_4 solution at 4°C. Then OsO4 was removed and samples rinsed with buffer. After centrifugation, low melting agarose which was kept at 45°C was poured onto the culture's pellets. They were cooled and solidified in refrigerator. Then, the samples were dehydrated in ascending series of ethanol, placed in propylene oxide and embedded in Araldite [256]. Leica EM UC6 Ultramicrotome was used for sectioning of araldite blocks. The ultrathin sections were stained with lead citrate and uranyl acetate [257]. The samples were examined in Jeol JEM 1400 Transmission Electron Microscope at an accelerating voltage of 80 kV.

For SEM imaging, fixed and washed cultures were dehydrated in ascending series of ethanol and transferred to amyl acetate. After critical point drying with CO_2 (Polaron CPD 7501), samples were coated with gold in a Polaron SC 502 sputter coater. The coated samples were examined with JEOL JSM 6060 LV SEM at accelerating voltage 10-15 kV.

3.2.6. SERS Measurements

SERS spectra were collected by Renishaw's Raman Microscopy with StreamLine™ Plus Raman imaging system using Olympus 20× (0.40 NA) long distance microscope objective and Olympus 50× (0.75 NA) long distance microscope objective with 2 s exposure from 830 nm excitation with 150 mW laser power between 470 cm^{-1} and 1470 cm^{-1} spectral range. The laser spot size was calculated using diameter=1.22 λ/NA formula which was found 2.5 μm for 20× long distance objective and 1.35 μm for 50× long distance objective. The depth resolution of an optical microscope is calculated from the formula $\lambda/(NA)^2$ [258]. From the formula, the resolvable depth profile can be observed in the range of five μm.

After AuNP treatment and drug exposure steps in monolayer culture, the cells were trypsinized and placed on CaF_2 slide in an appropriate volume of DMEM. The cells were allowed to settle down on CaF_2 slide for a while. Then, SERS spectra of single cells were

collected from a square area covering almost the a whole single cell with two and 1.5 μm ascending steps using 20× and 50× long distance objectives, respectively. An average of 36-64 spectra were collected from a single cell. The obtained SERS data were processed using Wire 4.1 software by substracting baseline to eliminate background slope, smoothing to remove noise peaks. After the spectra were averaged, the spectrum normalized to 1. The average of spectra from 20 single cells were used for the evaluation.

The spheroids were placed on CaF_2 slide within appropriate volume of DMEM for SERS measurement. The un-treated spheroids were used as control. Three μm steps in *x-y* axis and 10-μm steps through inner layers of a spheroid in *z*-axis were set to map a volume of a spheroid. SERS spectra were collected using 20×long distance objective with 2 s exposure from 830 nm excitation with 150 mW laser power between 470 cm^{-1} and 1470 cm^{-1} spectral range. The obtained SERS data were processed by substracting baseline, smoothing and normalization. Then, the spectra obtained from each layer in *z* axis were averaged and compared with the spectra of other layers in the spheroid.

3.2.7. Statistical Analysis

The coefficient of variation (CV) values is calculated after the data pre-processing steps. For monolayer culture, average spectra of 20 cells were used. The standard deviation of intensity corresponding Raman shifts was divided by their mean. The results were multiplied by 100 and then all data was averaged. For spheroid culture, the deviation of spectral intensity corresponding Raman shifts obtained from same layer of spheroid was divided by their mean. The results are multiplied by 100 and then all data was averaged.

The variables in SERS spectra from different layers of control and Dox treated spheroid were reduced to most overwhelming variables using principle component scores (PCA) utilizing IBM SPSS 20.0 software. Then, linear discriminant analysis (LDA) was utilized in order to observe the discrimination of the intra-layer spectra from interlayer spectra of a spheroid as well as the between the layers of different spheroids.

4. RESULTS AND DISCUSSION

4.1. PREPARATION OF GOLD NANOPARTICLES AND INTRACELLULAR UPTAKE

AuNPs are noble metal nanomaterials used in a range of biomedical applications due to biocompatibility, non-toxicity, and stability. The plasmonic properties of AuNPs can be tuned by altering size and shape. They also allow easy surface chemistry modifications with a variety of ligands through Au-S bond, which enables imaging of targeted cellular organelles [89, 259]. In this thesis, 50 nm average size of citrate reduced spherical AuNPs was used since they are effectively uptaken by cells and their aggregates provide superior SERS enhancement [70]. TEM image of the AuNPs is provided in Figure 4.1-a. The plasmon absorption band of AuNPs was observed at 527 nm as seen in Figure 4.1-b. Dynamic light scattering (DLS) measurements showed that the average hydrodynamic size of AuNP in colloidal suspension is 58 nm as seen in Figure 4.1-c. The hydrodynamic size was obtained larger than the size obtained with TEM because DLS measures the hydrodynamic diameter of AuNPs by also measuring the citrate ions associated with NPs surface.
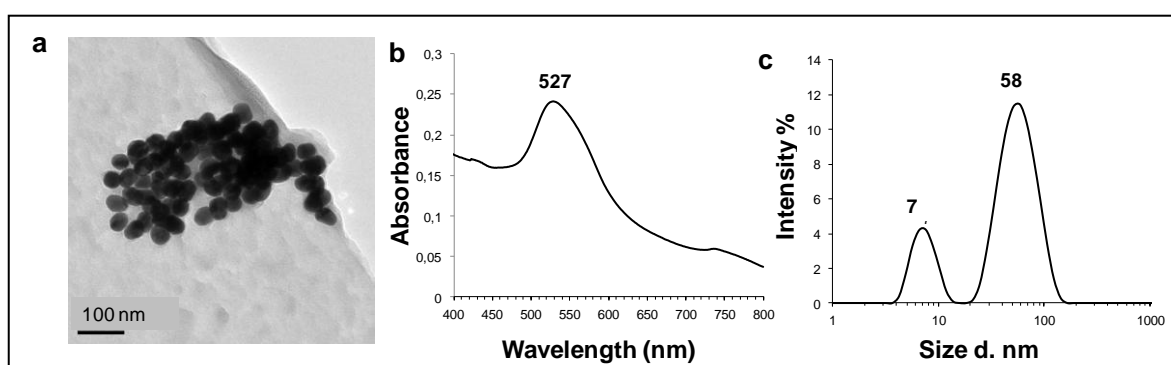
Figure 4.1. (a) TEM images, (b) UV-Vis spectra and (c) DLS spectra of AuNPs synthesized with citrate reduction method.

The interperation of the obtained spectra from a cell requires an understanding of intracellular uptake, localization and aggregation of AuNPs. Several studies were utilized at different incubation times for the intracellular AuNPs uptake [71, 81, 82, 89, 235, 242].

As a common consensus, an equilibrium of AuNPs uptake and synchronization of the biochemical environment are needed for the interrogation of cell for death to avoid from the bias arising from cell phase and NP-aggregation-based spectral changes [71, 82, 89]. Therefore, a pulse/chase approach was used by incubating the cells with AuNPs for 6 h, 12 h and 24 h (pulse) and replacing with fresh medium for 24 h (chase) as similar with previous reports [79, 242]. With light scattering properties, AuNPs aggregates can be monitored using confocal microscopy. Figure 4.2 shows the confocal images of AuNP-aggregates with a 640 nm laser exposure after 6 h, 12 h and 24 h treatment of HeLa cells and the following chased times to 24 h. From the images, the AuNP-aggregates were clearly observed inside the cells for each time point.
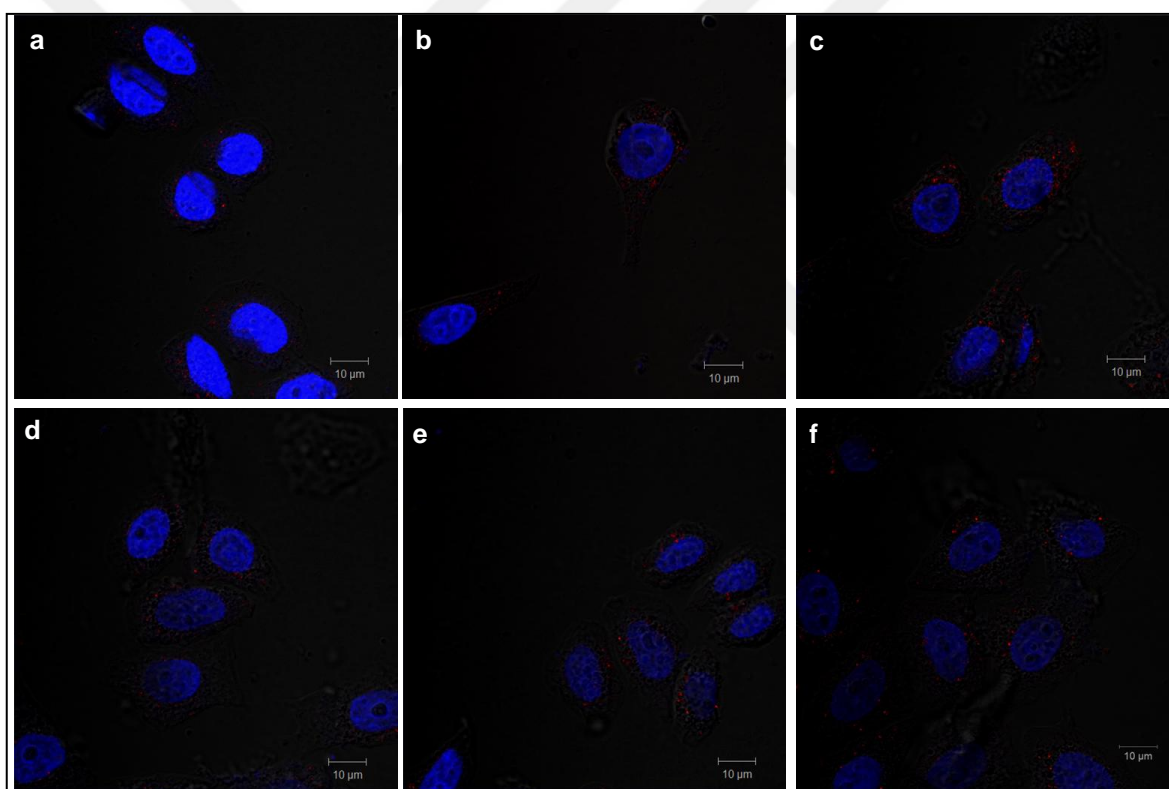
Figure 4.2. Confocal microscopy images of HeLa cells after (a) 6 h, (b) 12 h and (c) 24 h pulse with AuNPs and to 24 h chase times for each (d, e and f, respectively).

The confocal microscopy images give some clues about the cellular uptake of AuNPs but it is not sufficent to monitor the localization of the NPs. Thus, the intracellular location of the AuNPs and morphology of the aggregates were further evaluated with TEM imaging. Figure 4.3 shows TEM images of HeLa cells after exposed to the AuNPs in monolayer

culture for 24 h. As seen, the AuNPs aggregates were observed in endosomal vesicles and the average aggregation size was observed about 360±80 nm (n=5).

The reliability of SERS is determined by ensuring the observed spectra without any contribution of structural changes induced with toxic effect of AuNP on cells. Thus, the toxicity of the AuNPs was investigated by evaluating the cell viability through monitoring the mitochondrial activity using WST-1 assay and cell cycle function. HeLa cells were incubated with the medium containing AuNPs for 24 h, and then the culture medium replaced with fresh medium without AuNPs (post-incubation). Figure 4.4 shows (a) the viability and (b) the cycle phases of HeLa cells for 72 h of post-incubation. As seen, the AuNP-incubation did not change the viability and cycle function of HeLa cells during 72 h.
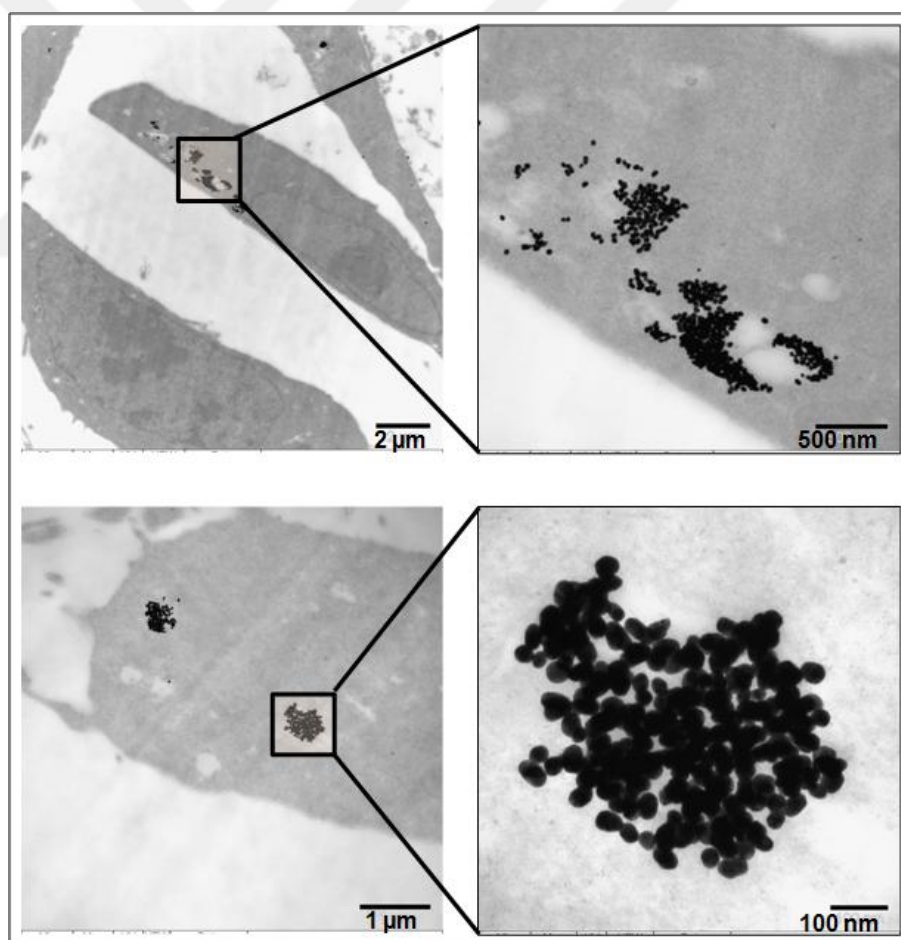
Figure 4.3. TEM images of AuNP-incubated HeLa cells in monolayer culture.
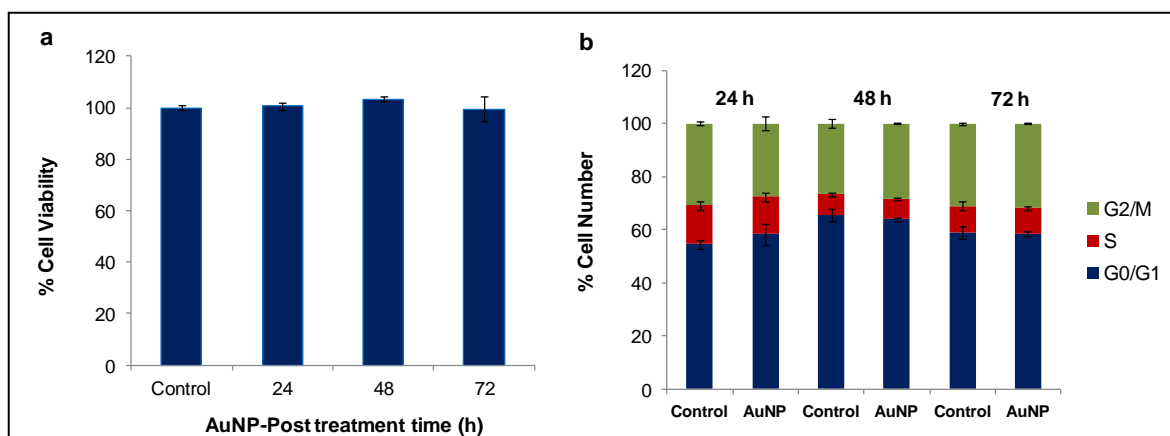
Figure 4.4. (a) Viability and (b) cycle analysis of HeLa cells post-treatment of AuNPs for 24, 48 and 72 h in monolayer culture. G0/G1 phase (first growth phase), S phase (DNA synthesis) and G2/M phase (growth phase for mitosis). Control shows the viability of non-treated cells.

4.2. DETERMINATION OF INSTRUMENTAL BASED PARAMETERS FOR LIVING CELL-SERS ANALYSIS

Once the SERS substrate is effectively placed in a particular intracellular location, the utilization of instrumental based parameters for living cell analysis is also crucial to obtain meaningful spectra. The spectral resolution principally depends on excitation wavelength of laser (λ) and numerical aperture (NA) of objective. In this study, a laser wavelength in NIR region, which was 830 nm, was selected in living cell analysis due to several reasons. One of the reasons is its low energy, which protects the cells from photo-induced damage [260-263]. The other one is that the laser in NIR region limits fluorescence contribution to the spectra [264]. The last one is that the use of NIR laser also helps to increase electromagnetic field enhancement by coupling with the plasmon absorption of aggregated AuNPs.

The acquiring of a high quality of SERS spectra from biological samples depends on the laser intensity impinging on a sample, which is determined by the laser power and NA of an objective. Optimization of laser power and exposure time are important to protect sample from radiation based damage. In order to determine the optimum laser power for living cell SERS analysis, a single cell was mapped with excitation of 830 nm laser with 3

mW, 15 mW, 30 mW and 150 mW power at 2 s exposure time using 20× objective. Figure 4.5 shows the average spectra obtained from a single cell with increasing laser powers. Each spectrum was represented after data pre-processing steps, which is explained in detail in Figure 4.8. As seen, the measurements with 3 mW and 15 mW laser power resulted with noisier spectra. The increasing the laser power to 30 mW increased the signal to noise (S/N) ratio, but the contribution of noise to the spectra was still observed. A 150 mW laser power provided a better S/N without harming the cell integrity [265].
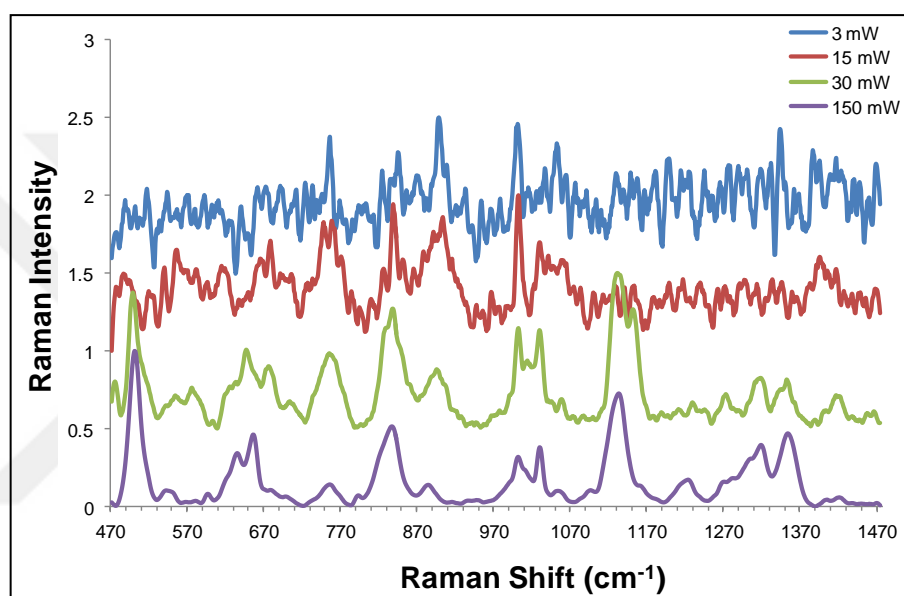
Figure 4.5. SERS spectra of a single cell measured with excitation of 3 mW, 15 mW, 30 mW and 150 mW power of 830 nm laser.

The objective magnification is other critical parameter influencing the spectral quality (S/N ratio), which has inverse relation with the laser spot size, and direct relation with the laser power density on sampling area. When a higher magnification objective is used, the spot size becomes smaller and the power density on the sampling spot increases resulting with increased S/N. In order to evaluate suitable objective magnification for living cell analysis, 20× and 50× long distance objectives were utilized. The laser spot size was calculated from the formula: diameter $=1.22\ \lambda/NA$. The spot size was found 2.5 µm for 20× objective (NA=0.4) and 1.35 µm for 50× (NA=0.75) objective. Figure 4.6 shows the comparison of SERS spectra obtained from HeLa cells using both objectives before and after the normalization. The spectra were acquired with 2 µm steps using 20× objective while 1.5 µm step was used for 50× objective. In total, 20 cells were analyzed and the average of the

spectra from the cells was used for the comparison. The difference in the intensity of the spectra obtained with different objectives was clearly seen in Figure 4.6-a. The spectra obtained using 50× objectives caused three times more intense spectra due to increased S/N with the increased laser intensity at the sampling area. The comparison of these spectra after normalization was shown in Figure 4.6-b. As seen, the similar spectral pattern was observed, but a decreased intensity was observed between 1250 cm^{-1} to 1400 cm^{-1} in Amide III region of the spectra obtained using 20× objective compared to the spectra obtained with 50× objective.
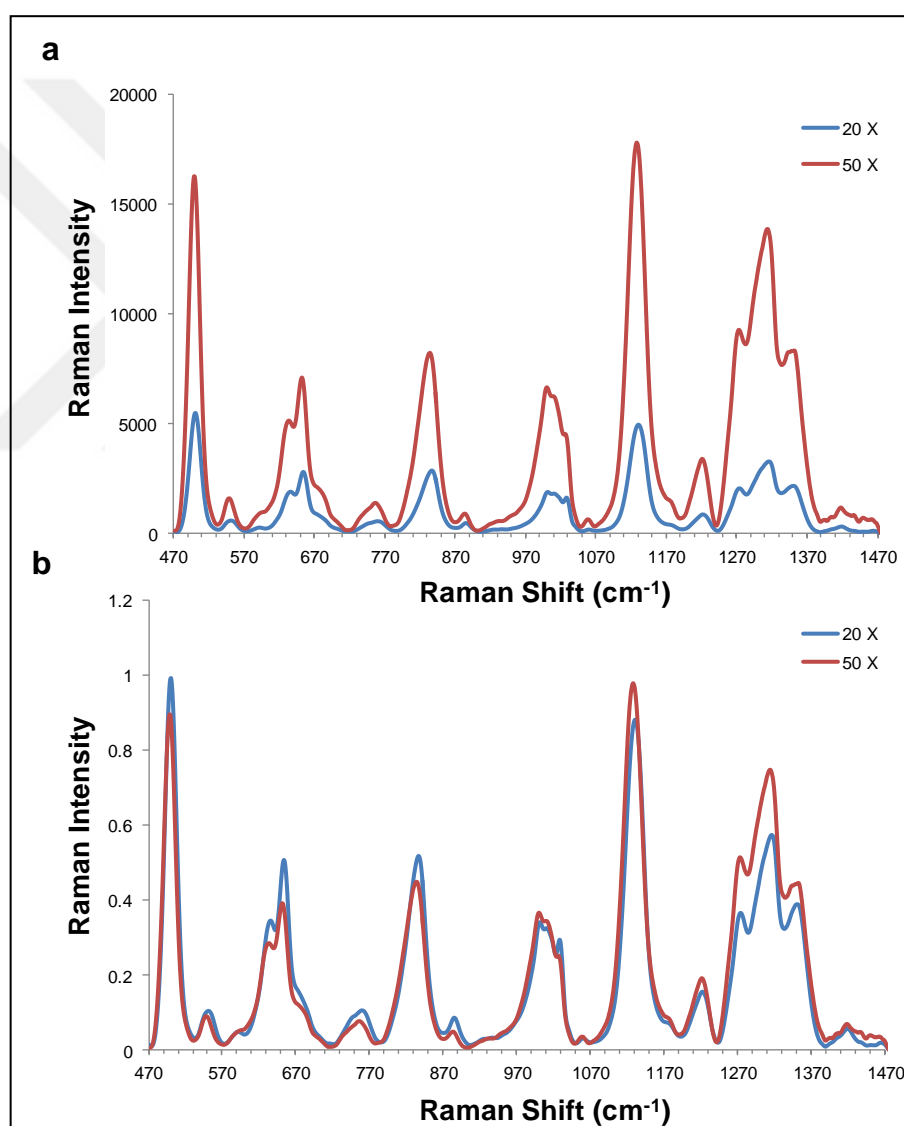
Figure 4.6. SERS spectra of HeLa cells obtained with 20× and 50× objectives (a) before and (b) after normalization.

The results indicated that although more intense SERS spectra was observed with 50× objective, the normalized spectra did not show any significant difference with the normalized spectra obtained with 20× objective. Since using 20× objective decreases the laser intensity on sampling area and thus, decreases the possibility of photo-induced damage, it was selected for the further investigations.

The mechanism of AuNPs uptake and aggregation, and influence on SERS spectra were previously demonstrated by Kneipp *et al.* [79]. In the study, they showed that the AuNPs were individually uptaken into the cells and the individual AuNPs formed small aggregates such as dimer or trimer by changing the endosomal environment. They observed that the AuNPs grew into multiple aggregates with different sizes in endosomal vesicles in a confined 3D structure, which provided different SERS spectra [266]. It was also reported that the distribution of AuNPs in different z-position in 3D cellular structure resulted in different Raman images [267]. Therefore, it is possible to obtain different spectral pattern in each measurement without adjusting an optical focus since AuNP-aggregates can locate between cell membrane and nucleus during transportation from the early endosomes to late endosomes [268]. In order to evaluate the objective focus based variations, a deeper focus was set on a single cells (0-stage). The single cell was mapped at different depths of focus starting from -5 µm deeper position to 5 µm upper position with one µm interval in z axis. Figure 4.7 shows the average SERS spectra (a) before and (b) after data normalization in each positions. Using the intensity at 500 cm^{-1} corresponding to disulfate (S-S) bond vibration as a reference peak of ensodomes, the intensity at optical focus (0-point) was observed about 11000 counts (black-spectrum) as seen in Figure 4.7-a. As the measurement was performed towards deeper position at -3 µm, the intensity increased to 12000 counts. When the measurements performed towards the upper positions of the focal point at 5 µm position, the intensity decreased to about 700 counts. As seen, the adjustment of a deeper the focal point can provide optimum spectral intensity. Figure 4.7-b shows the comparison of average SERS spectra from different focal points after the normalization step. As seen, no significant difference was observed on spectral pattern obtained in different depth positions. However, the intensity variations were clearly observed when the spectra collected from upper or deeper positions of the focal point.
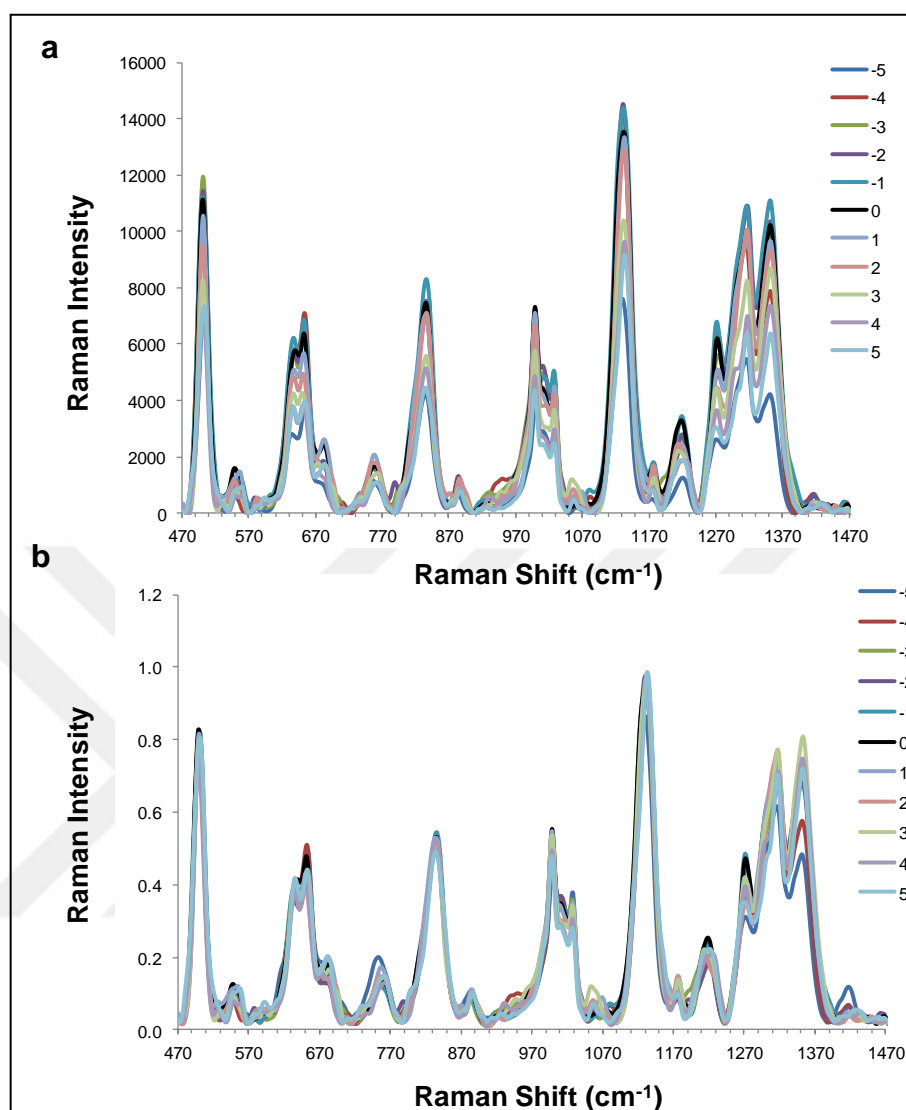
Figure 4.7. Comparison of average SERS spectra obtained from a single cell at objective focus (0) and at different depths of focus starting from -5 μm deeper position to 5 μm upper position with 1 μm interval (a) before and (b) after normalization.

4.3. SERS MEASUREMENTS ON MONOLAYER CELLS AND DATA PROCESSING

The demonstration of SERS measurement set up on a single cell and the data pre-processing steps are summarized in Figure 4.8. AuNPs treated HeLa cells in monolayer culture were detached from the cell culture flask and placed on the CaF_2 slide in a appropriate volume of cell culture medium. The cells were let for a while to settle down on CaF_2 slide surface before the SERS measurement. The image of objective focus on cells

under 20× magnification and the area to be scanned are shown in Figure 4.8-a. A raster scan with 2 μm steps was performed with 2 s excitation of 150 mW power of 830 nm laser. As seen, SERS measurement was performed in an area covering almost whole cell. An average of 36-64 spectra were collected from each cell. Data pre-processing was applied to the obtained spectra before the interpretation in order to minimize the irrelevant variations. Data pre-processing step was performed with Wire 4.1 software. Briefly, baseline subtraction was applied to flat the slopped spectra due to the fluorescence or thermal background by the utilization of automatic intelligent fitting algorithms. The overwhelming intense cosmic rays were removed. Smoothing was applied to obtained spectra to reduce the noise. After these steps, the obtained spectra were represented in Figure 4.8-b. The difference in the signal intensity and spectral pattern at different positions of the cell are clearly seen. The inevitable difference of the spectral intensity come up due to the heterogeneous distribution of AuNPs and AuNP-aggregates inside the cells. The intense spectra was probably originated from the molecules in endosomes. The spectra were averaged in 4th step as shown in Figure 4.8-c. The averaging of the spectra after smoothing enabled to eliminate spectral outliers with lower intensity. Then, the averaged spectrum was normalized between 0 and 1. The normalized spectrum shown in Figure 4.8-d was used as a signature of a single cell since the amount of internalized AuNPs and aggregates inside cell can vary and cause intensity difference between the cells in a batch. The average spectrum of 20 cells is used for the evaluation of a batch to decrease the variation. The average of the normalized spectra from 20 cells was used for the represent the profile of cells in a batch as shown in 7th step in Figure 4.8 f.

4.3.1. Effect of AuNPs Exposure and Post-incubation Times on SERS Spectra of Living Cells

As demonstrated previously, the spectral variations can occur due to both aggregation of particles and changes in biochemical composition of endosomes [79, 82]. The use of such unstable system causes uncertainty in experimental outcome and decrease the reliability for the evaluation of external stimuli. In order to assess uptake and aggregation based variations, the spectral outcome was monitored by using AuNPs pulse and chase approach as mentioned earlier.
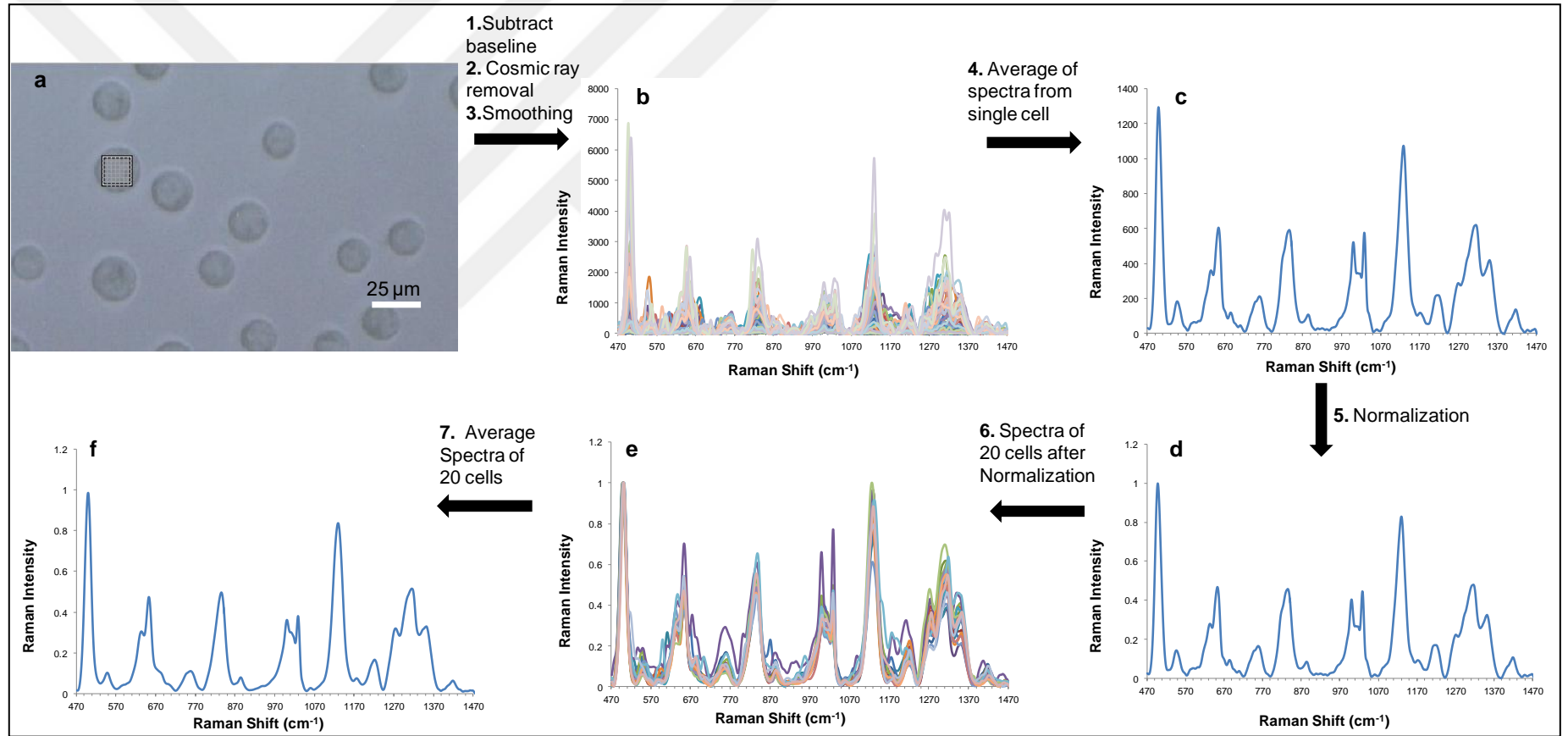
Figure 4.8. Data pre-processing steps applied for a single cell and assessment of spectral information in a batch.

HeLa cells were incubated with AuNPs containing culture medium for 6, 12 and 24 h (pulse). After each time point of incubation, the culture was replaced with a fresh medium and the incubation was completed to 24 h (chase time). Different pulse and chase times were investigated since the AuNPs can be localized on the surface or in endosomal vesicles close the membrane or in cytosol within different maturation steps.
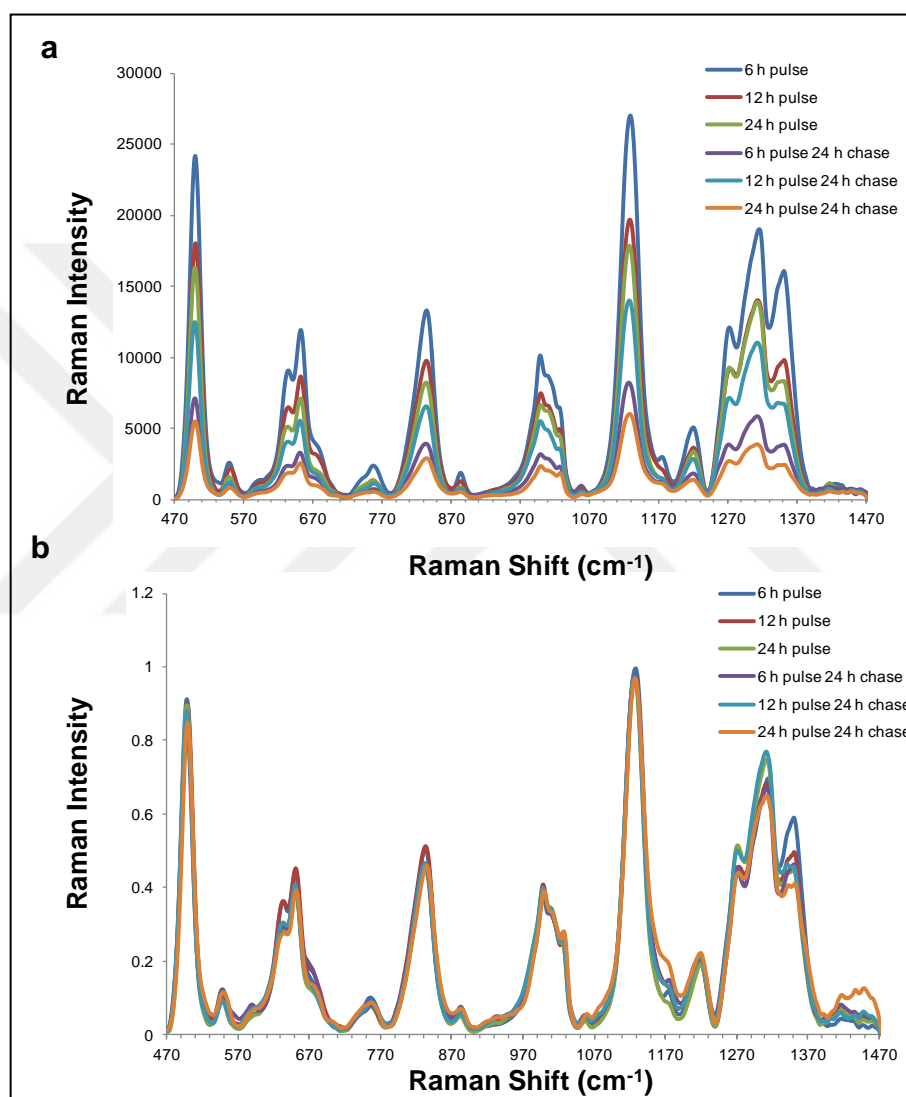
Figure 4.9. SERS spectra of HeLa cells incubated with AuNPs for 6, 12, 24 h (pulse) and 24 h post incubation (chase) (A) before and (B) after data normalization.

Figure 4.9 shows the spectra obtained in each time point of incubation (a) before and (b) after data normalization. The change in the spectral intensity during pulse and chase times is clear as seen in Figure 4.9-a. However, no linear response was observed from the spectral intensity as the AuNP-incubation time (pulse) increased. Although the SERS

spectrum after 6 h pulse has higher intensity, 24 h chase time significantly decreased the intensity due to the transfer of the AuNPs and AuNPs aggregates from the mother cell to daughter cells during mitosis. The same results were also obtained with 12 h and 24 h pulse and 24 h chase times. For 24 h pulse, the SERS intensity was seen higher compared to 24 h chase of 6 h and 12 h pulse, which may show that the intracellular uptake continue during 24 h. The data normalization for each time point showed that although intensity variances were observed with different pulse and chase durations, the SERS spectra from HeLa cells showed similar spectral pattern. As a result, the variations in spectral pattern after an external stimuli can be reflected without contribution of internal variations.

4.3.2. Evaluation of the Cellular Response to Anti-cancer Drugs Using SERS

The advantages over fluorescence based techniques with non-destructive and non-invasive nature make SERS as a potential tool for analysis of cellular response to external stimuli. New SERS based methodologies either by colloidal or non-colloidal substrates have been investigated to effectively explore the changes in the molecular structures [89, 90, 243, 246, 250, 253, 269]. AuNPs modified with NLS were intensively investigated to monitor molecular changes in nucleus for the evaluation of drug efficiency and cell death [89, 90, 243, 269]. The non-colloidal SERS substrates were also employed for the understanding of the molecular changes at cell nucleus and cytoplasm upon external stimuli [250, 253]. Compared to the previous reports, the cell death was monitored based on the changes in endosomal compartments upon external stimuli with model anti-cancer drugs, which were Doxorubicin (Dox) and Cisplatin in this study. As it was indicated above, AuNP-treatment did not influence the cell cycle function and cell viability. In addition, the AuNP-pulse/chase times did not cause any spectral changes as indicated above. As seen, the changes is neither related with the AuNP-toxicity nor the biochemical changes in endosomes, which cannot cause any confusion about the response to external stimuli. Before the SERS analysis, an effective concentration for Dox and Cisplatin were determined by monitoring the cell viability. During the evaluation, HeLa cells were first incubated with AuNPs for 24 h, and then treated with the drugs in a fresh cell culture medium for 24 h as it was used for SERS analysis. The results were compared with the drug-toxicity itself.
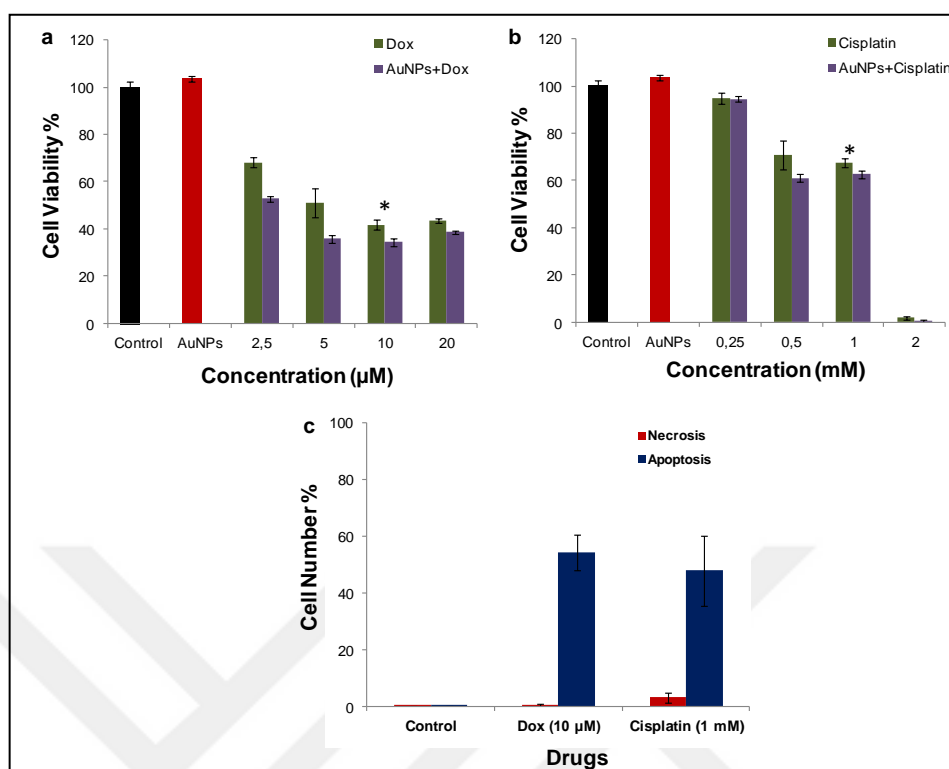
Figure 4.10. Evaluation of the effect of AuNPs and drug-treatment on cell viability and the effect of AuNP-pre-treatment on the drug toxicity. Cell viability after (a) Dox and (b) Cisplatin treatments. * shows EC50 value. (c) Annexin V/PI staining analysis at EC50 values of Dox and Cisplatin.

The effective concentration (EC50), at which the 50 per cent of cells died, was determined by analyzing the cell viability using WST-1 mitochondrial activity assay. At EC50 value, the apoptotic and necrotic cells were analyzed using Annexin V-PI staining. Figure 4.10-a shows the cell viability after exposure of Dox to HeLa cells in 2.5-20.0 μM concentration range. The pre-AuNP treatment influenced the effect of Dox by decreasing the viability of HeLa cells 7-10 per cent more than Dox itself. From the results, the viability was decreased to 50 per cent at 5 μM concentration and did not change significantly up to 20 μM concentration exposure. 10 μM concentration was selected to monitor the induced biochemical changes using SERS. The effect of Cisplatin on HeLa cell viability was demonstrated in Figure 4.10-b. 0.25 to 2 mM concentration range was used for the evaluation. The cell viability decreased 60 per cent up to 1 mM concentration while the cell viability lost completely at 2 mM concentration. Similarly, pre-AuNP treatment decreased the cell viability 5-10 per cent more than Cisplatin itself. One mM concentration was decided for SERS investigations. The induced death pathways were also analyzed in

order to conduct with the molecular changes reflected on SERS spectra. Annexin V/PI staining showed that both drugs induced about 50 per cent apoptosis in HeLa cells as seen Figure 4.10-c.
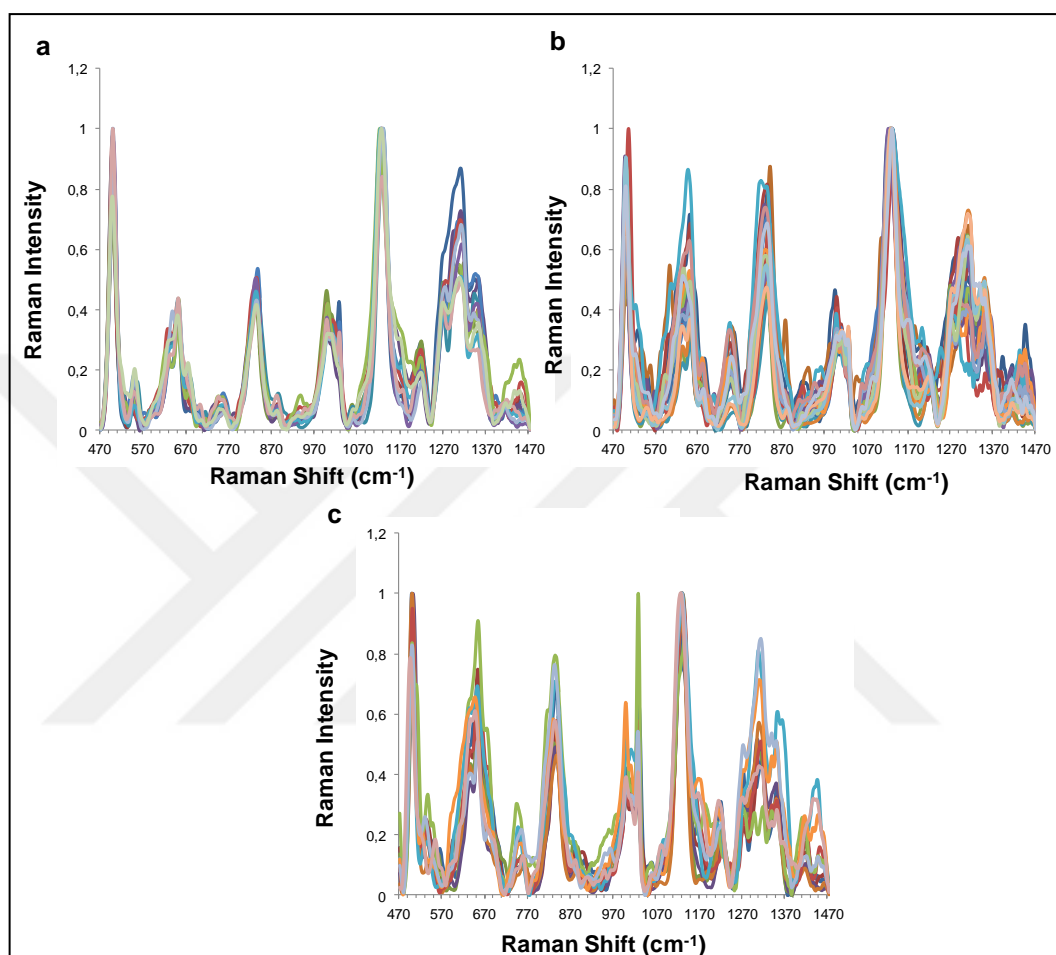
Figure 4.11. Reproducibility of SERS spectra obtained from (a) control and (b) Dox and (c) Cisplatin treated HeLa cells in monolayer cell culture. Insets show the CV values.

The comparison of average SERS spectra obtained from each control, and Dox and Cisplatin treated cells was demonstrated in Figure 4.12. The assumptions were made corresponding to the biochemical changes occuring in endosomal compartments upon apoptosis induction. The averaged spectra showed that the intensity of peaks corresponding to at 555 cm^{-1}, 590 cm^{-1} and 630 cm^{-1} originating from cholesterol, phosphotidylinositol and glycerol, respectively, in cytosolic membrane structure components increased after Dox and Cisplatin treatment. In addition, phospholipid peak at 1080 cm^{-1} arised. The intensity of CH_3CH_2 bending vibrations at 1310 cm^{-1} decreased. The overall changes in endosomal membrane structure can be due to the release of cholestrol and degradation of

phospholipid structure induced by caspase activation and increased cytosolic Ca^{2+} with the initiation of apoptotic cell death [270, 271]. The peak intensities corresponding to the hydrophobic side chains of proteins at 750 cm^{-1}, 1001 cm^{-1}, 1030 cm^{-1} and 1170 cm^{-1} increased, which attributed to the upregulation of protein structure in endosomes. The peak intensity at 680 cm^{-1} corresponding to nucleotides increased indicating the energy production in the endosomes [69].
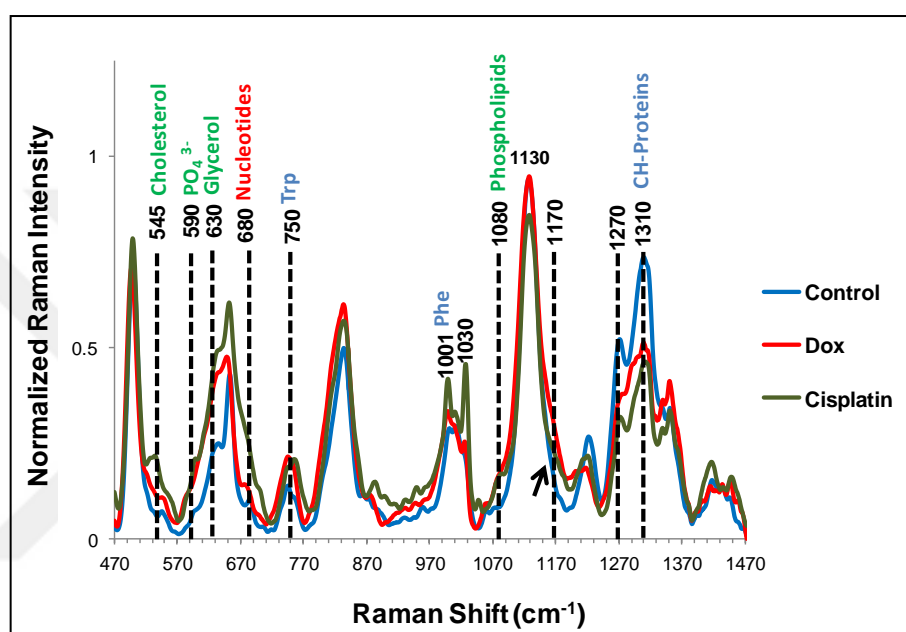
Figure 4.12. Comparison of SERS spectra obtained from HeLa cells after 24 h exposure to Dox (10 µM) and Cisplatin (1 mM).

It is difficult to identify major changes in multiple overlapping peaks in SERS spectra obtained from complex biological environment. The most observable variables from the large data set are extracted using principle component multivariate analysis (PCA). Therefore, PCA was utilized for the SERS spectra of each control, Dox and Cisplatin treated cells. The first 31 principle components (PCs) were found expressing 99 per cent of the total variance. The first (PC1), second (PC2) and third (PC3) PCs represented 40.0 per cent, 18.5 per cent and 10.4 per cent logical variation as demonstrated in Figure 4.13-a. Due to the heterogeneity in a culture system, Dox and Cisplatin treated cells cannot be separated distinctly from the control group with the three components as seen from dot plot. PC shows not only changes in a peak corresponding to a molecule but also the other accompanying peaks in a positive or negative contribution. Figure 4.13-b represents the spectra of PC1, PC2 and PC3 scores.

The detailed variations in PC1 was found due to negative contribution of endosomal membrane structure components and proteins, and positive contibution of nucleic acid structures. Particularly, the intense negative bonds at 500 cm^{-1} corresponding to S-S groups and 568 cm^{-1} corresponding to tryptophane side chain of proteins were observed, which could be due to to the release of endosomal proteases into cytoplasm. In addition, cholestrol peak at 550 cm^{-1}, phospholipid peak at 1130 cm^{-1} and CH$_2$ backbone deformation corresponding to lipids at 1305 cm^{-1} were also negatively contributed to the PC1 score, which is expected to be the deformation of endosomal membrane structure. The positive contribution of bands at 744 cm^{-1} and 814 cm^{-1} corresponding to nucleic acids and PO$_2^-$ stretch of nucleic acids are probably indication of energy production due to the endosomal acidification. In the case for PC2, negative contributions were observed from tryptophan (761 cm^{-1}) and COO$^-$ group of aminoacids (1406 cm^{-1}), and glycogen (1047 cm^{-1}), which can be associated with the change in the protein structures with the change of the acidic condition in endolysosomes. The positively accompanying bands were observed at 646 cm^{-1} and 818 cm^{-1} corresponding to C-C twisting mode of tyrosine and C-C twisting mode of proteins, respectively, and at 1131 cm^{-1} and 1305 cm^{-1} corresponding to phospholipids and CH$_2$ deformations of lipids. The negative bands of PC3 score were observed at 505 cm^{-1} (S-S), 651 cm^{-1} (C-S gauche vibrations of amino acids), 1027 cm^{-1} (glycogen) and 1133 cm^{-1} (fatty acids) while positive bonds were observed at 600 cm^{-1} (nucleotide), 760 cm^{-1} (trypthophane), 946 cm^{-1} (polysaccharides in skelatal structure) and 1048 cm^{-1} (glycogen). As a result, endosomal membrane destabilization, induced the regulation of protein structures and energy production were manifested in the PCs of the SERS spectra.

Linear discrimination analysis (LDA) is another statistical method for the classification, which maximize the intragroup variables and minimize the intergroup variables. LDA was utilized for 31 PC scores of the SERS spectra of the control, and Dox and Cisplatin treated cells in order to characterize and classify the groups. The each group was classified with 100 per cent accuracy and sensitivity. The classification of different groups with LDA indicated that the spectra obtained from Dox or Cisplatin treated cells were clearly separated from both control cells and each other.
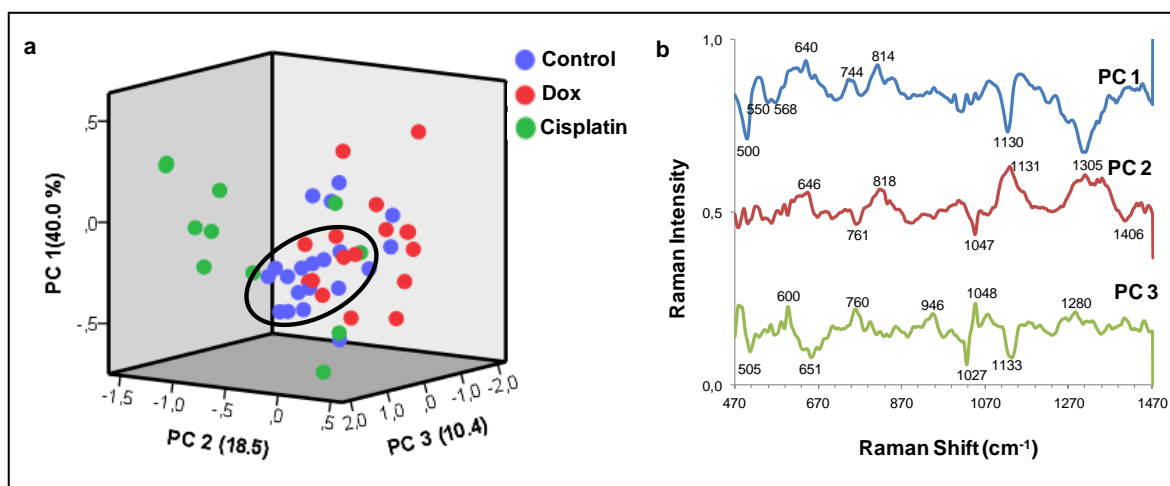
Figure 4.13. PCA of control and Dox (10 µM) and Cisplatin (1 mM) treated HeLa cells. (a) Scores plot of first three PCs; PC 1, PC 2 and PC 3 and (b) their loadings.
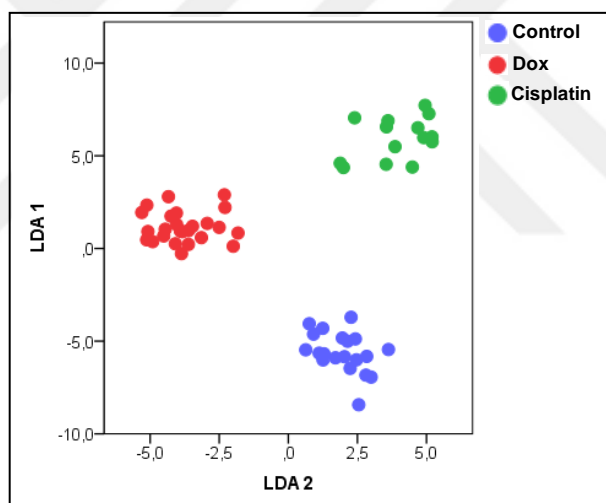
Figure 4.14. LDA of control, and Dox (10 µM) and Cisplatin (1 mM) treated HeLa cells from 31 PCs.

4.4. PREPARATION OF SERS BASED 3D CULTURE

3D cell culture models facilitate the progression in drug discovery studies and tissue engineering applications by mimicking *in vivo* systems in which the cells are in contact with neighboring cells. There have been many reports about the establishing of 3D culture models but it has been controversial which model is more likely mimicking the cells as they are in their natural environment [105]. Although preparation method determines the

quality of spheroids and the results of analytical techniques, the lack of techniques for analysis of the cells in their 3D environment culture is another issue leading confusion about understanding of prominent cellular response regardless of preparation methods. Scaffold free spheroid model is a rationale structures and generally recommended by the experts for drug discovery studies targeting solid tumor tissues. For the establishing of a model spheroid culture, reproducibility of the culturing model without disturbance of viability of cells, with similar volume and shape should be well characterized [91-93]. All of the parameters such as cell type, density of cells, incubation time and the 3D culture preparation method influence the characteristics of spheroids [107, 108]. In general, spheroids between 200 µm and 500 µm diameter in size without a secondary necrosis in central region are recommended to generate a clinically relevant culture model [103].
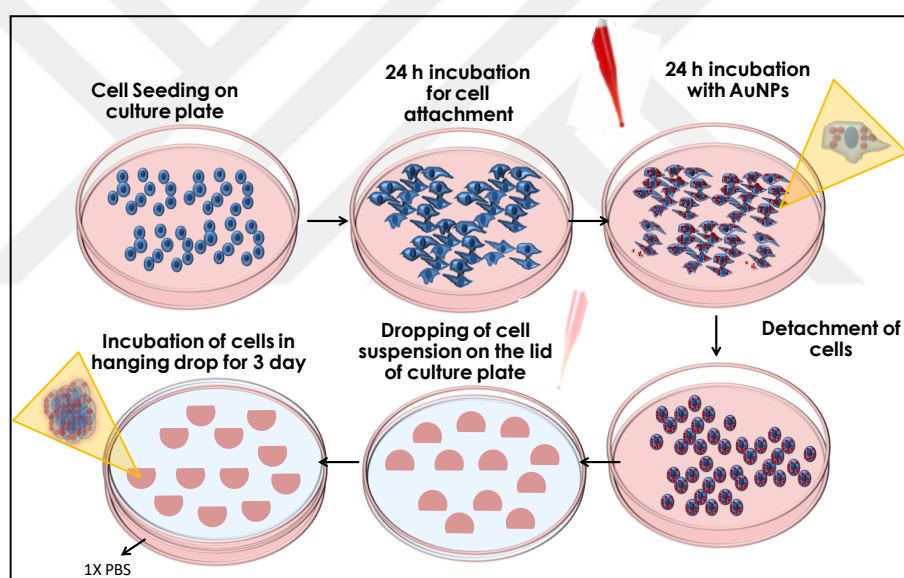
Figure 4.15. Schematic representation for preparation of SERS based 3D spheroid culture using hanging drop method.

In this study, hanging drop model was used due to the providing more uniform size of spheroids with a simple preparation approach. The experimental procedure for the preparation of SERS based 3D spheroid model was represented in Figure 4.15. Briefly, human cervical cancer (HeLa) cells, used a model cancer cell line forming tumors, were incubated with citrate reduced 50 nm AuNPs for 24 h in monolayer culture. Then, the cells were detached from the surface and 250, 500 and 1000 cells in 10 µl of fresh cell culture medium were dropped on a lid of cell culture plate and inverted on the top of plate, where PBS placed into the bottom of plate to provide the humidity and prevent the drops from

drying. The cells were incubated in hanging drops for 72 h, which were then transferred into culture plate coated with PDMS to prevent adhesion on surface for the following drug exposure procedure.
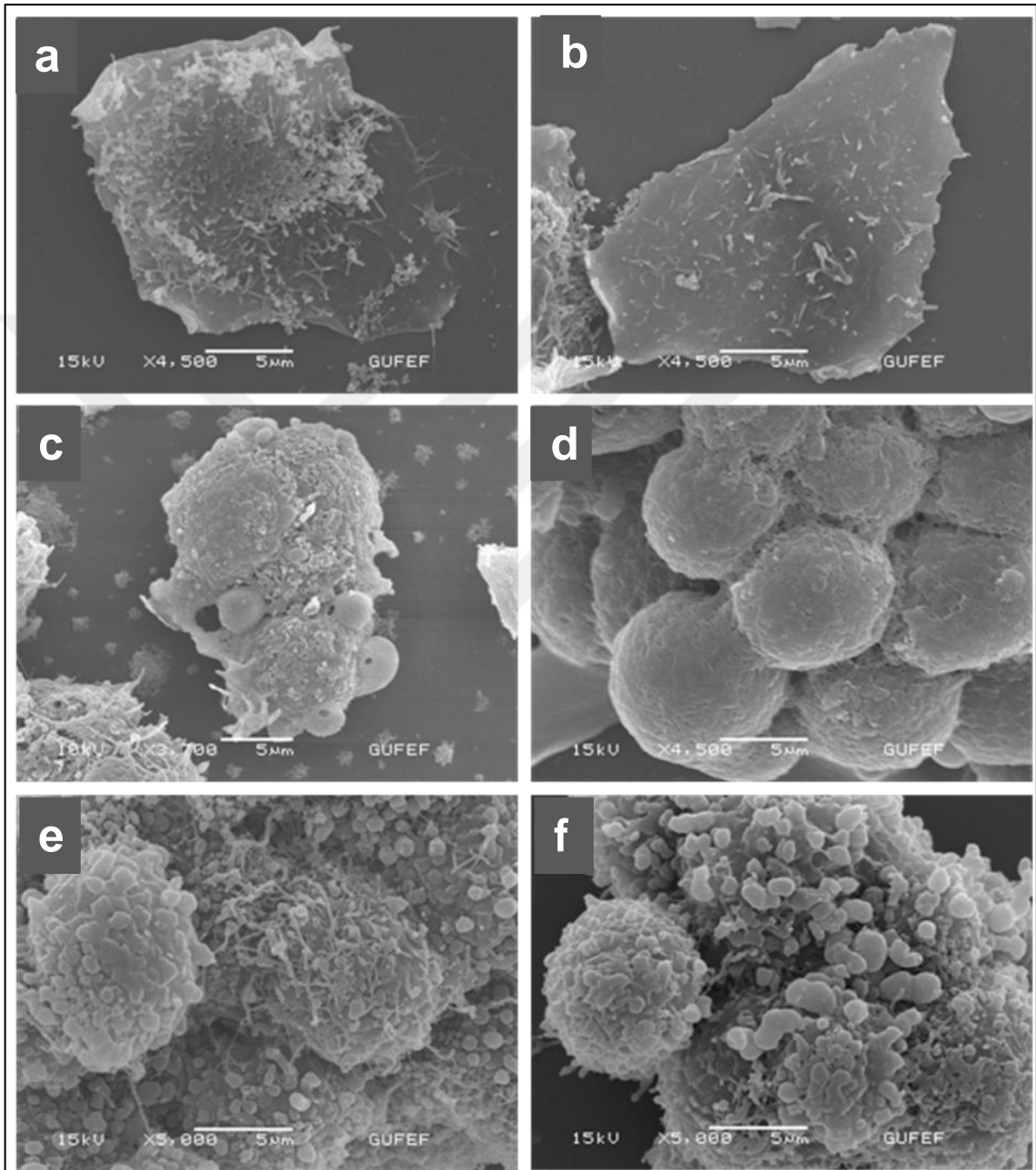
Figure 4.16. SEM images of control (a,c,e) and AuNPs treated (b,d,f) HeLa cells in monolayer (a and b, respectively) and 3D cultures after 72 h (c and d, respectively) and 120 h incubation (e and f, respectively). Scale bar is 5 μm.

Figure 4.16 shows SEM images of HeLa cells in monolayer culture and after hanging drop incubation for 72 h and 120 h. As seen Figure 4.16-a and b, both without/with AuNPs

incubated cells, respectively, have similar morphology in monolayer culture with thin and sheet like structure. After hanging drop incubation during 72 h, the cells in both group linked with each other and formed a 3D grape like shape spheroids as clearly seen in Figure 4.16-c and d. The smooth surface of spheroids with tight cell to cell junctions was clearly observed at 120 h incubation of without/with AuNPs incubated HeLa cells from SEM images in Figure 4.16-e and f, respectively.
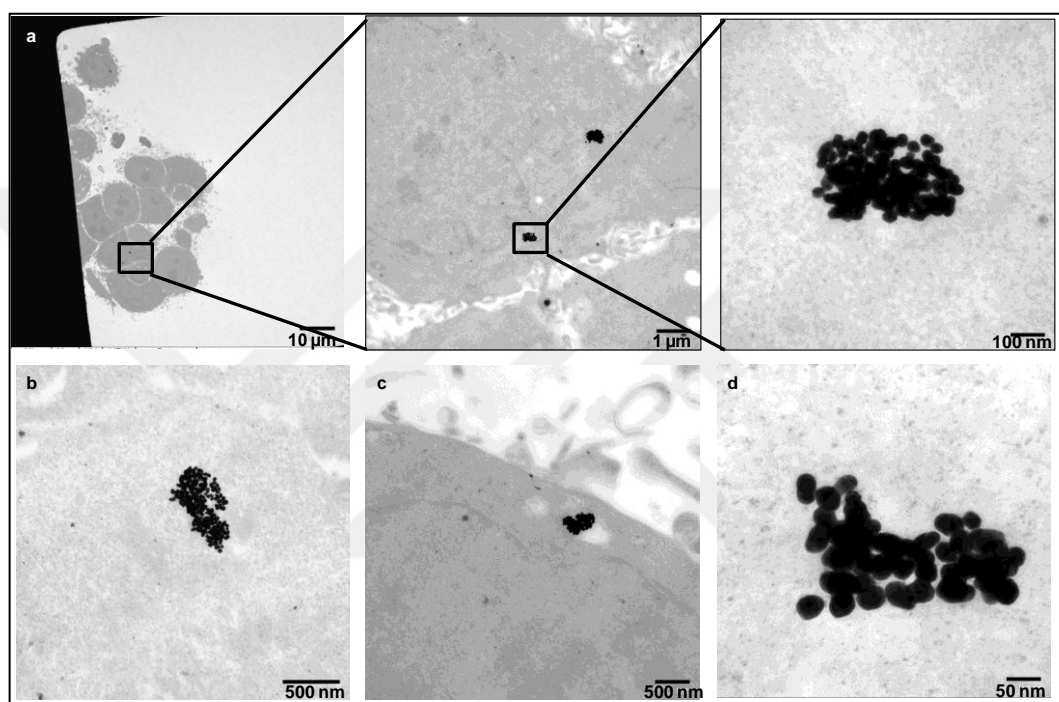
Figure 4.17. TEM images from cross-section of 3D-HeLa spheroids incubated for 72 h in hanging drop with showing intracellular AuNPs aggregates (a) increasing magnifications and (b-d) from different regions.

The localization of AuNPs inside the cells, aggregation status and shape can cause variation in the SERS spectra of living cells. Figure 4.17 shows the TEM images of the cross-sections of spheroids formed after 72 h hanging drop incubations, AuNPs aggregates inside the cells, and their distribution between the cells at the same cross-sections. As seen in Figure 4.17-a, the cells were arranged arbitrarily in a close contact each other within a spheroid. However, the AuNP-aggregates were not observed in each cells at same cross-section which might be the different localization of AuNP-aggregates in z-slices inside the cells caused distribution in different slices. The AuNP-aggregates were observed in different sizes and shapes in different cells from different cross-section of spheroids as

shown in TEM images in Figure 4.17-b, c and d. After post-incubation for 72 h, the average size of AuNP-aggregates was found 360±80 nm (n=5) similar to the aggregate size in monolayer culture, as shown in TEM images above in Figure 4.3.

Figure 4.18 shows TEM images of cross-sections of spheroids, and AuNP-aggregates in endosomal vesicles after 120 h incubation. The average AuNP-aggregate-size was measured 350±85 nm (n=5). However, the AuNP-aggregates were more compact in morphology compared to the aggregates as observed in the initial form incubation times.
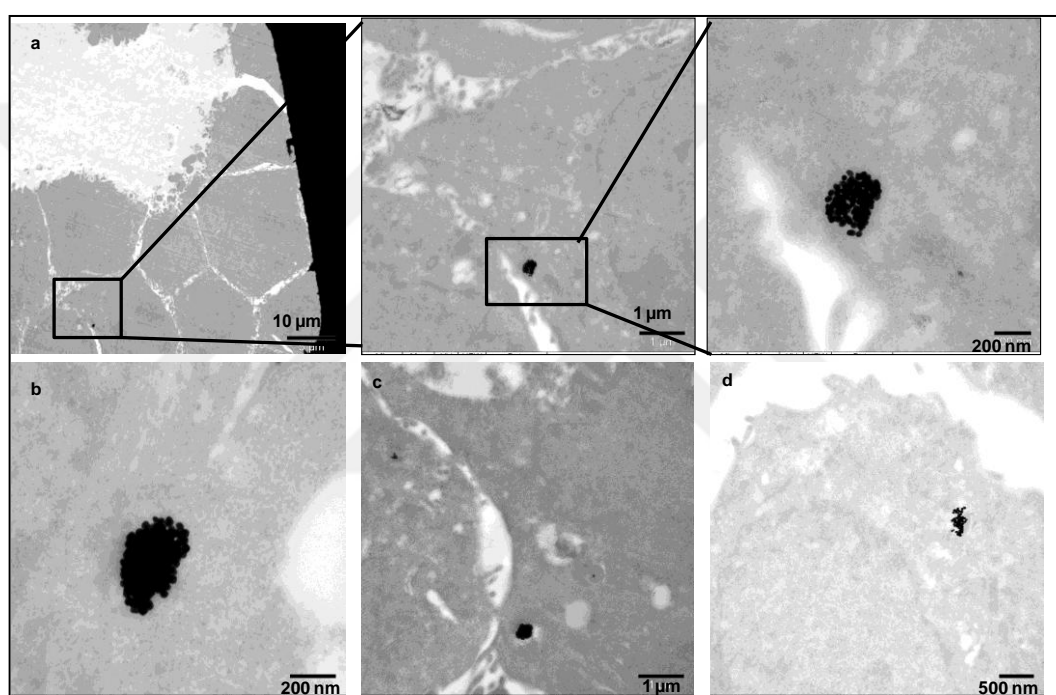
Figure 4.18. TEM images from different cross-sections of 3D-HeLa spheroids incubated for 120 h showing intracellular AuNPs aggregates (a) increasing magnifications and (b-d) from different regions.

Initial density of cells in a hanging drop suspension determine the size and densely package of spheroids. In order to obtain clinically relevant size of the spheroids, 250, 500 and 1000 HeLa cells in hanging drop were evaluated. After HeLa cells were incubated for 72 h, bright field images were acquired to monitor the shape and size of spheroids. Figure 4.19 shows the shape of spheroids and the comparison of spheroid-sizes formed by without/with AuNP incubated HeLa cells. As seen, the density of HeLa cells in spheroids influences the shape of spheroids. Although the spheroids prepared with 250 cells/drop seem more spherical, the 500 and 1000 cells/drop formed irregular shapes. Figure 4.19

shows the average sizes of the spheroids (n=10) and the comparison of the spheroid diameter prepared without/with AuNP incubated HeLa cells. Each of the spheroids had a clinically relevant size. In addition, no significant difference was observed between the spheroids prepared without/with AuNP incubated HeLa cells. Briefly, the average sizes were observed 300 μm for 250 cells/drop, 350 μm for 500 cells/drop and 400 μm for 1000 cells/drop. The spheroid size did not much increase as the increased in the initial cell density in hanging drop because the proliferation rate decrease as the number of cells increase in hanging drop [272].
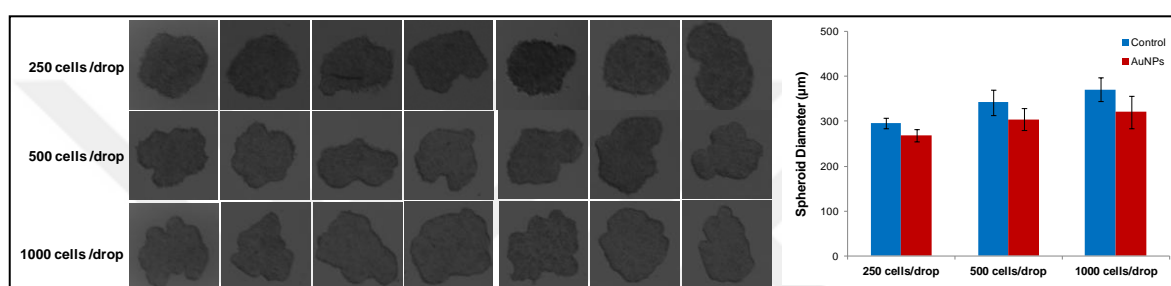
Figure 4.19. Bright field microscopy images of HeLa spheroids prepared with 250 cells/drop, 500 cells/drop and 1000 cells/drop after 72 h hanging drop incubation. Comparison of spheroid size prepared with 250, 500 and 1000 cells/drop without and with AuNP incubation.

For initial assessment of SERS on spheroids, a spheroid with 400 μm diameter size placed on CaF_2 slide. The image of spheroid under 5× magnification of Raman microscopy was shown in Figure 4.20-a. Then, the objective was turned on 20× magnification and the focus was adjusted on the outer surface of the spheroid, which was set as "0" position in z-axis. Then, spheroid was scanned towards the deeper regions after adjusting a scanning area or a slice on spheroid, as demonstrated in Figure 4.20-b. The scanning was performed by starting from the deepest depth position in z-axis towards to outer surface of the spheroid with 50 μm steps in z axis and 3 μm in x-y direction. The scanning was performed at 50, 100 and 150 μm in depth positions of the spheroid. The obtained spectra were pre-processed by removing background and cosmic rays. After smoothing and normalization steps, the sum of the spectra from each layer was used for the evaluation. CV values of the normalized spectra obtained from each cross-section were calculated in order to investigate the spectral reproducibility in a layer. Figure 4.20-c and d show SERS spectra obtained from the slice and area, respectively. As seen, although the spectral pattern was similar at

50 and 100 μm depth position, it changed at 150 μm depth position when the spheroid was scanned in a slice. CV value also increased from 60 to 67 per cent as the spectra were collected in the decreasing depth positions indicating that the reproducibility decreased when the spectra were collected in deeper position. When a volume was scanned by selecting an area on the outer surface of a spheroid, the average spectrum obtained at 50 μm depth position showed different pattern compared to the spectra obtained from 100 μm and 150 μm depth positions. However, CV values of spectra were obtained about 40 per cent from 50 μm and 100 μm depth positions while the value at the deepest point was observed 69 per cent. The results indicated that the scanning a large area decreased variations obtained from a cross-section inside a spheroid. However, the spectral reproducibility obtained from the deepest point was very low.

The physiological characteristics of spheroids, which depend on cell type, initial cell density and incubation time, determine outcomes of analysis [107]. In order to understand the influence of initial density of cells on the spheroid characteristics and the results of SERS spectra, the spheroids prepared with 250, 500 and 1000 cells/drop initial cell density for 72 h incubation. As it was demonstrated above, the spheroids formed with different cellular density were in clinically relevant size. The measurement was performed as demonstrated in Figure 4.21-a. Briefly, the focused area on the outer shell of spheroid was adjusted to "0" position in *z*-axis. An area in x-y direction was selected (45μm-60μm with 3 μm steps) and the measurements were started from the deepest point in *z*-axis where the SERS signals were observed. The measurement was ended approximately 20 μm below the outer surface by decreasing the depth with 10 μm scale. The scanning was stopped at that position due to the arbitrary orientation of the cells resulted in a rough topography on the spheroid surface. SERS spectra obtained from the different layers of spheroids formed by with 250, 500 and 1000 cells/drop were demonstrated in Figure 4.21-b, c and d, respectively. When the average of the average of intra-layer spectra was compared within interlayer spectra of a spheroid, the similar spectral pattern was clearly observed from outer surface to inner zone, but the spectral pattern was changed until a certain depth point. The changes in the spectral pattern were observed at 70 μm depth (orange spectrum), at 90 μm depth (pink spectrum) and at 120 μm depth (light blue spectrum) of the spheroids prepared with initial cell density 250, 500 and 1000 cells/drop, respectively.
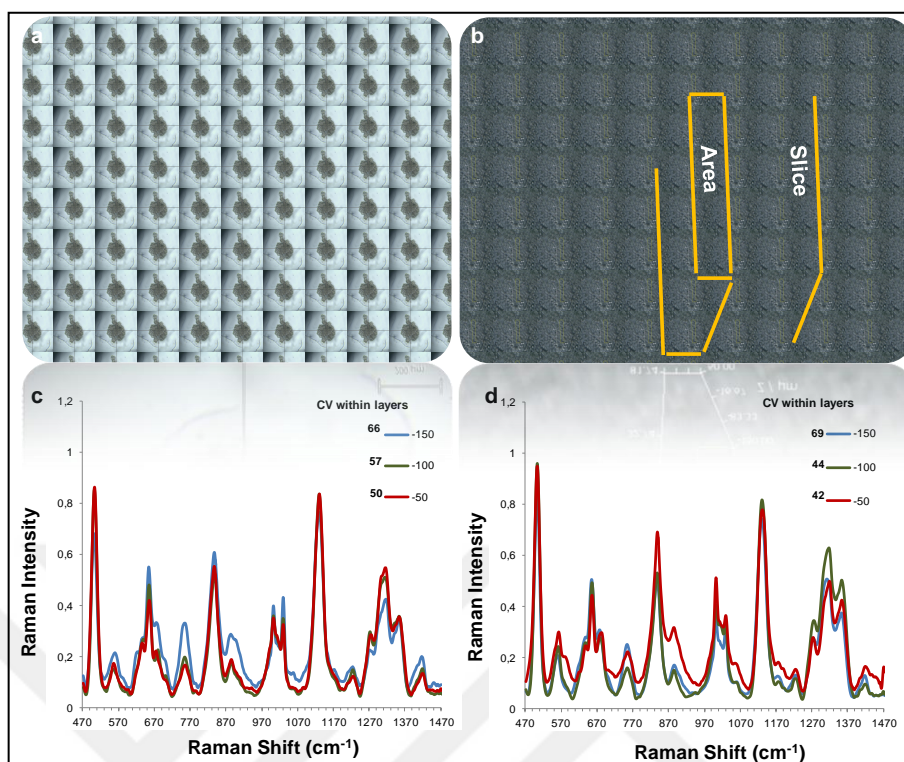
Figure 4.20. (a) Bright field microscopy image of HeLa spheroid cells after 72 h hanging drop incubation under 5× magnification and (b) representation of area and slice adjusted for SERS measurement, on a spheroid image under 20× magnification. SERS spectra obtained from the different depth layers of spheroid HeLa-cells obtained from the selected (c) slice and (d) area. Insets show CV values of the spectra obtained from each layer of spheroids.

Since it is not possible to separate the experimental variations from the response when an external stimuli is monitored, the acceptable variations of spectra from the deepest point of spheroid should be first evaluated before the experimental set up. CV values were calculated to observe the variations in the spectra obtained from each layer as shown in Table 4.1. The variation in the spectra obtained from the same layer increased as the spectra were collected from the deeper zones. It is clearly seen that average spectra of the layers with CV values lower that 55 per cent showed the similar spectral pattern with each layers. The results indicate that the characteristics of spheroid can change with the initial cell density, dependently influence SERS spectral outcome. The change in spectral pattern is estimated due to the heterogeneous distribution AuNPs in a cross-section of a spheroid as observed from TEM images. The decreased S/N may also cause the increase in CV values of spectra from deeper zones.
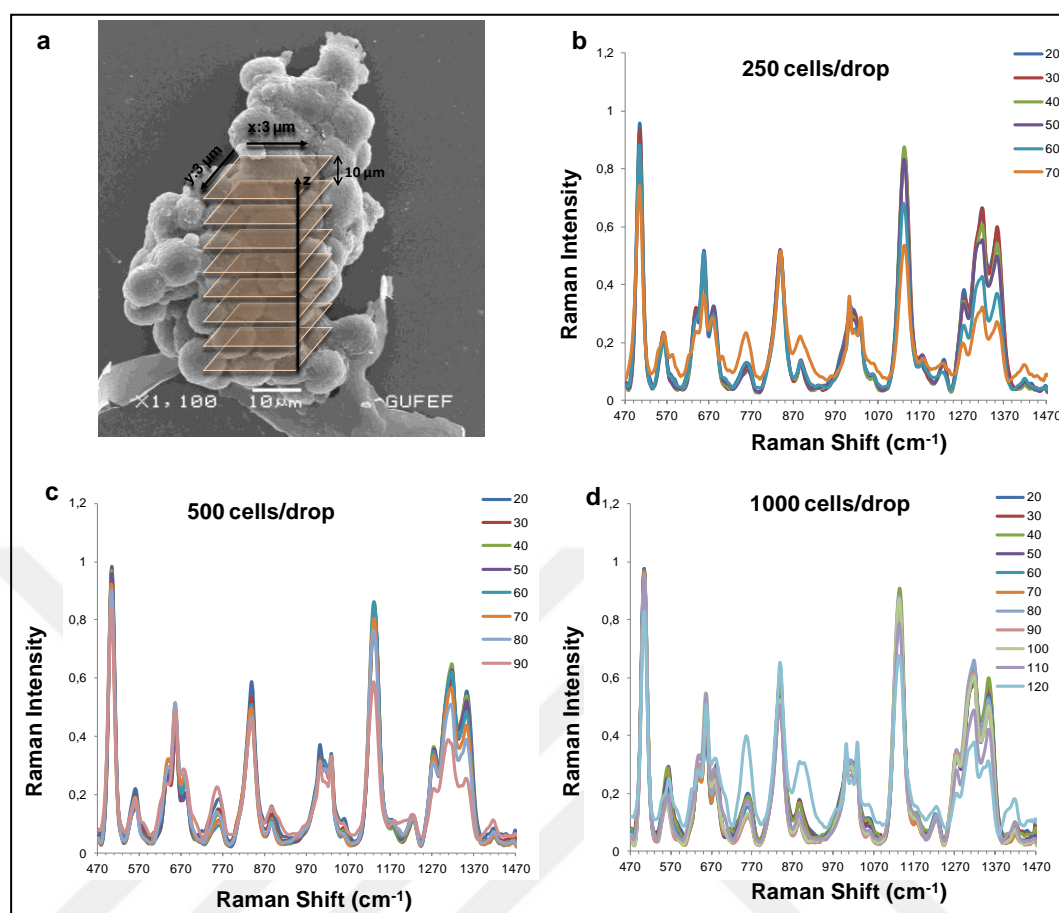
Figure 4.21. (a) Representation of volume of a spheroid on a SEM image of spheroid where SERS spectra collected. SERS spectra collected from increasing depth of spheroids prepared with (b) 250 cells/drop, (c) 500 cells/drop and (d) 1000 cells/drop in hanging drop for 72 h incubation.

Table 4.1. CV values of different layers of spheroids prepared with 250, 500 and 1000 cells /drop.

Layers	CV										
	20	30	40	50	60	70	80	90	100	110	120
250 cells/ drop	44.35	48.98	53.99	**59.91**	**63.64**	**72.83**	-	-	-	-	-
500 cells/ drop	33.25	35.20	39.36	48.34	54.53	**60.25**	**59.88**	**73.59**	-	-	-
1000 cells/ drop	35.18	41.66	40.55	43.50	51.63	48.23	53.51	52.37	52.95	53.42	**55.6**
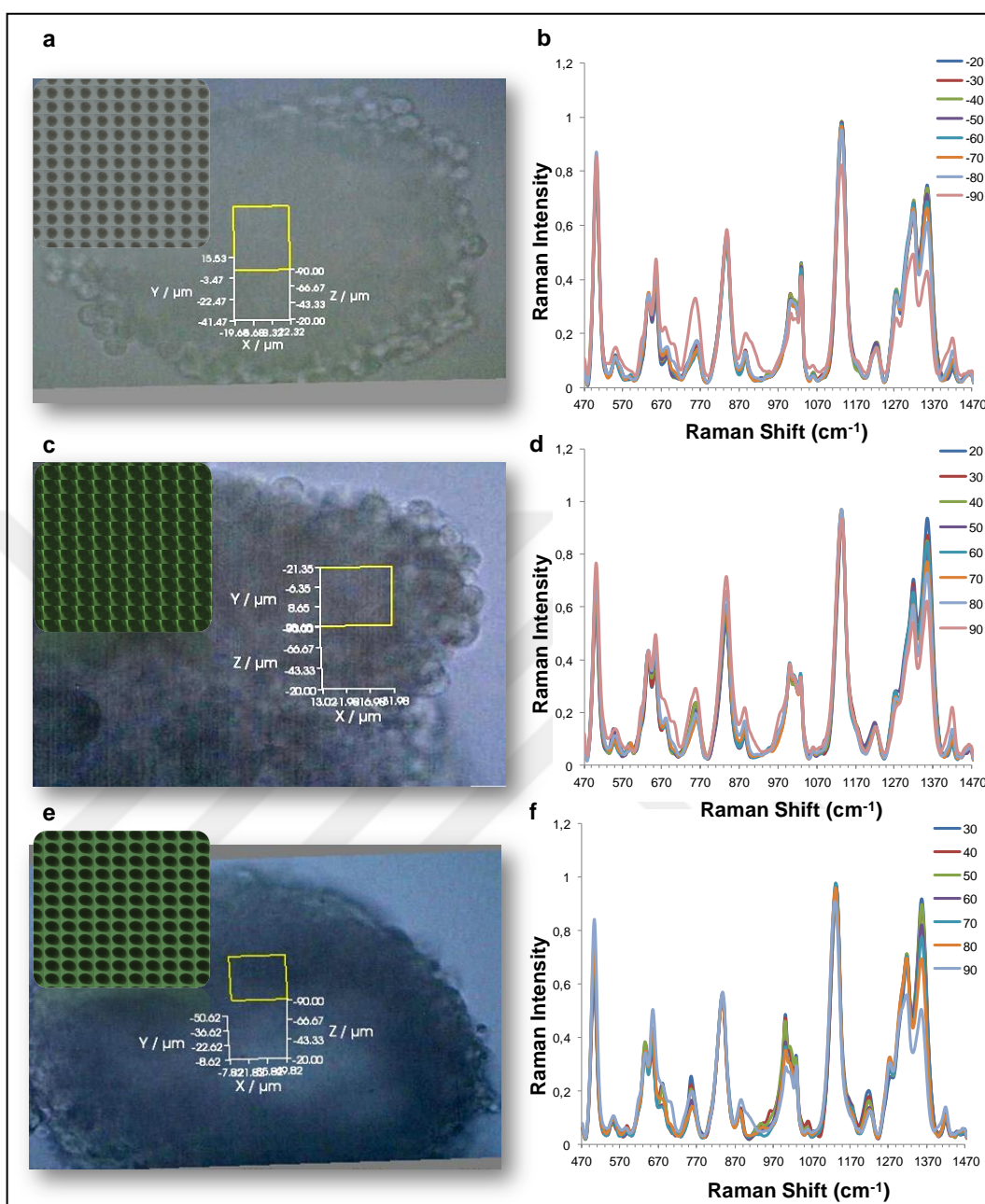
Figure 4.22. Bright field images of (a) HUVEC, (c) U87MG, (e) U373MG spheroid cells after 72 h hanging drop incubation under 20× magnification. The marked volume on the image of spheroids shows the regions selected for SERS measurement. Insets show the bright field microscopy images under 5× magnification. The comparision of SERS spectra obtained from the different depth layers of (b) HUVEC, (d) U87MG and (f) U373MG spheroids.

The approach was also analyzed on the spheroids prepared with different cell lines. Human umbilical vein endothelial cells (HUVEC), U87MG and U373MG human glioblastoma cell

lines were used for the evaluation. Figure 4.22 shows bright field microscopy images of the spheroids and the volume of the spheroid marked on the image used for the SERS measurements, and the comparison of SERS spectra obtained from the different layers of spheroids. As seen in Figure 4.22-a, 500 initial density of HUVEC cells formed spherical shape of spheroids with an average 250 µm in diameter after 72 h incubation. When an area (30 µm-45 µm in x-y axis) was selected for the spectral evaluation and scanned through the increased depth position (z-axis), the spectral pattern changed at 90 µm depth. The spheroids of both glioblastoma cell lines were prepared with 2000 cells/drop initial cell density. The shape of U87MG spheroids was observed elliptical after 48 h incubation as seen in the inset image of Figure 4.22-c. The average spectra obtained from eight different layers of U87MG spheroids were shown in Figure 4.22-d. The change in the spectral pattern was observed at 90 µm depth from the outer surface. U373MG cells formed spherical shaped spheroids as seen in Figure-e. When the average spectra from each layer compared, spectral pattern changed at 90 µm depth. As seen, different cell lines formed different physiological characteristics of spheroids. Therefore, SERS based spheroid model has to be well characterized according to used cell type, initial cell density with its shape and the depth position providing acceptable spectral variation before used in drug testing.

4.5. EVALUATION OF DRUG PERFORMANCE USING SERS BASED 3D SPHEROID MODEL

After optimization of the SERS based spheroid model and evaluation the experimental bias that can arise during the assessment, the drug testing performance of the approach was investigated by monitoring the spectral changes after exposure of a model anti-cancer drug, Dox. The expectation was to observe the biochemical changes reflected on SERS spectra, induced by the apoptotic cell death that occur to endolysosomal compartments. The spheroids were prepared by using 500 cells/drop for 72 h hanging drop incubation. After spheroids were formed, they were transferred into PDMS coated 24 well plate, where the Dox treatment (5 µM) was performed. Figure 4.23 shows the spectra obtained from the different layers of control (without treatment) and Dox-treated spheroids. No significant variations were observed from the spectra obtained from the different depth positions of the control spheroid as seen in Figure 4.23-a. After Dox treatment, significant changes in

the spectral pattern especially at the layers close to the outer shell were observed as seen in Figure 4.23-b. Briefly, peak intensities at 555 and 590 cm^{-1} originating from cholesterol and phosphotidylinositol, respectively, from cytosolic membrane components and 1060 cm^{-1} corresponding to C-C stretching of lipids apparently increased from 20 μm to 30 μm depth positions of spheroid. In addition, the peak corresponding to cholesterol at 710 cm^{-1} also raised. The changes might be due to the initiation of apoptotic cell death, at which caspase activation and increased high cytosolic Ca^{2+} cause the cholestrol release and degradation of phospholipid in endolysosomal membrane structure [270]. The increased peak intensities corresponding to the CH$_2$ (886 cm^{-1}), hydrophobic side chains of the proteins (755, 1000, 1180 cm^{-1}) and CH deformation (1450 cm^{-1}) were attributed to the CH residues of proteins in Amide III region can be sign of the changes in protein structures in endosomes. The overall changes in SERS spectral pattern can be explained with the apoptotic cell death. The significant changes in spectral pattern from outer shell towards 30 μm depth may be due to the rate of penetration of Dox through the depth regions of spheroids [273].
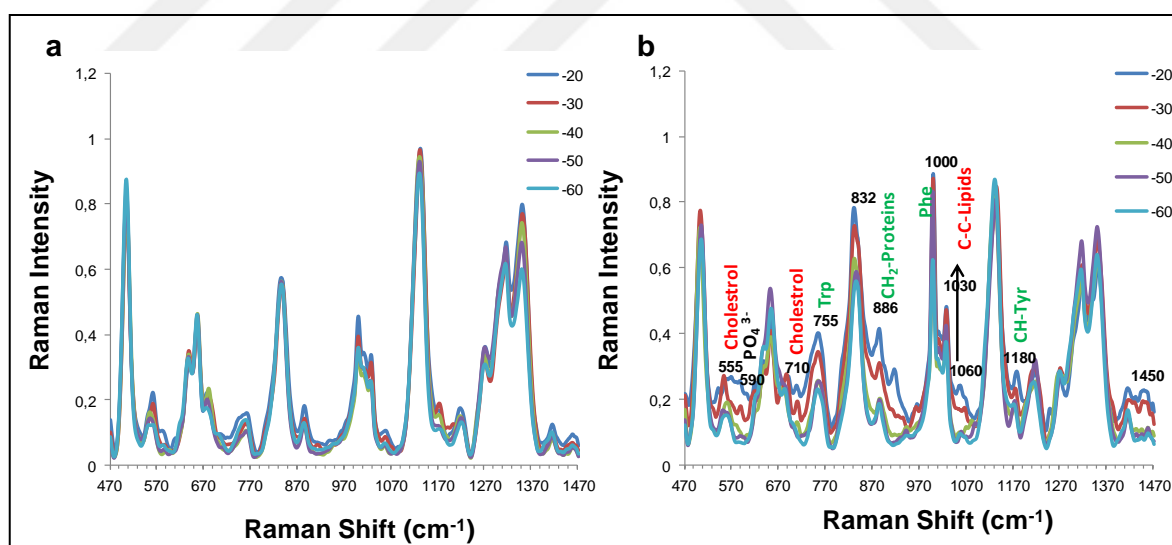
Figure 4.23. SERS spectra obtained from the different layers of (a) control and (b) Dox treated HeLa spheroids prepared with 500 cell/drop.

The most overwhelming variables of SERS spectra obtained from different cross-section of each control and Dox treated spheroids were analyzed with PCA. The first 72 PCs accounting for 95.5 per cent of total variance of SERS spectra were extracted in the case of control spheroids. The first (PC1) and second (PC2) PCs expressed 31.5 per cent and 14.0

per cent of reasonable variation, respectively. As seen in PCA plot in Figure 4.24-a, the dots representing the spectra obtained from different layers of control spheroid cannot be well separated with each other. A few spectra corresponding to 20 μm and 30 μm depth layers of control spheroid were separated. In the case for the spectra obtained from Dox treated spheroids, the first 95 PCs with 93.9 per cent of total variance of spectra were obtained. Figure 4.24-b shows the variables in the spectra of Dox treated spheroids. The most of them were obtained from the PC1 and PC2 calculated as 27.3 and 17.9 per cent, respectively. The PC1 and PC2 of spectra obtained from 20 μm and 30 μm depth layers of Dox treated spheroid were clearly separated from other layers.

Figure 4.25 represents comparison of the major variations of first and second PCs of control or Dox treated spheroids. The comparison of PC1 scores of control and Dox treated spheroids was demonstrated in Figure 4.25-a. The major changes after Dox treatment were observed with positive contribution of peaks corresponding to the S-S bonds (510 cm^{-1}), hydrophobic side chains of proteins (637 cm^{-1}, 1030 cm^{-1}) and carbohydrates (1040 cm^{-1}, 1177 cm^{-1}) while negative contributions were observed from the peaks corresponding to membrane lipid structures (875 cm^{-1}, 910 cm^{-1}, 1195 cm^{-1}). Figure 4.25-b shows the comparison of PC2 scores of each control and Dox treated spheroids. The significant difference in the peak positions was clearly seen. The positively dominating variables of control spheroids were observed corresponding to hydrophobic amino acids at 565 cm^{-1} and 1360 cm^{-1} (Trypthophane), 850 cm^{-1} (Tyrosine) while O-P-O stretch at 826 cm^{-1} and cytosine at 1292 cm^{-1} most probably due to the energy production and phospholipid structure of endolysosomal membrane at 1270 cm^{-1} were negatively contributed. PC2 scores of Dox treated spheroids were observed corresponding to glycerol at 592 cm^{-1}, C-S trans amino acids at 695 cm^{-1}, and Amide III region of proteins at 1233 cm^{-1}, 1251 cm^{-1} and 1280 cm^{-1} with positive contribution while the hydrophobic trypthophane residue of proteins at 1350 cm^{-1} negatively contributed. As it is clearly seen from the PCs scores, the variables of the spectra from control and Dox treated spheroids were independent. PC1 of spectra from Dox treated spheroid differentiated from the spectra of control spheroid mostly with the increase in hydrophobic side chains of proteins and carbohydrate contents of endolysosomes and decrease in the membrane structure contents. However, the PC2 scores showed the variances in opposite direction. While the variables of control spheroid corresponding to the hydrophobic side chains of proteins, phosphate and nucleic acid

structures increased and residues on membrane structures decreased, the secondary structure of proteins and endolysosomal membrane structure increased and hydrophobic residues decreased in Dox treated spheroid.
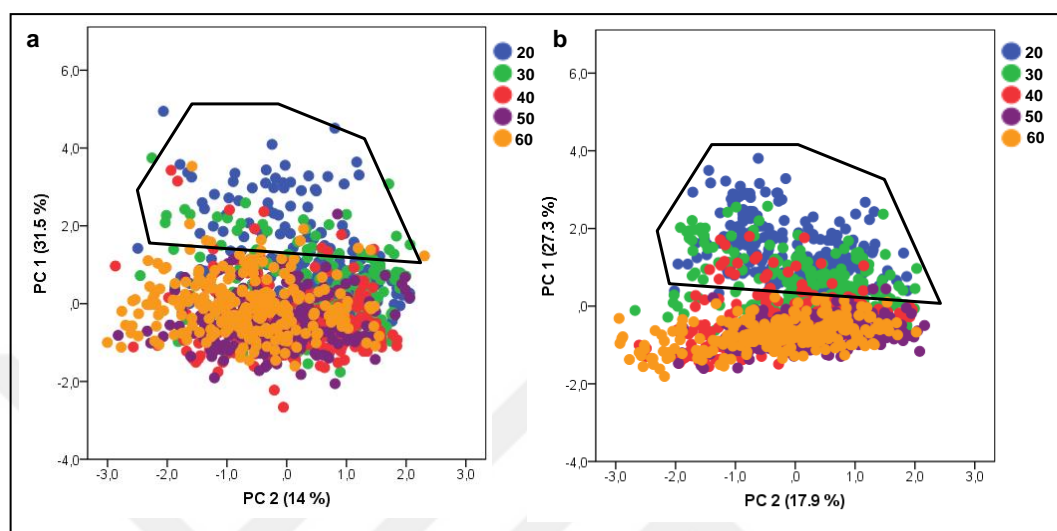
Figure 4.24. PCA plots for the first and second components of SERS spectra obtained from the different layers of (a) control and (b) Dox treated HeLa spheroids prepared with 500 cells/drop.
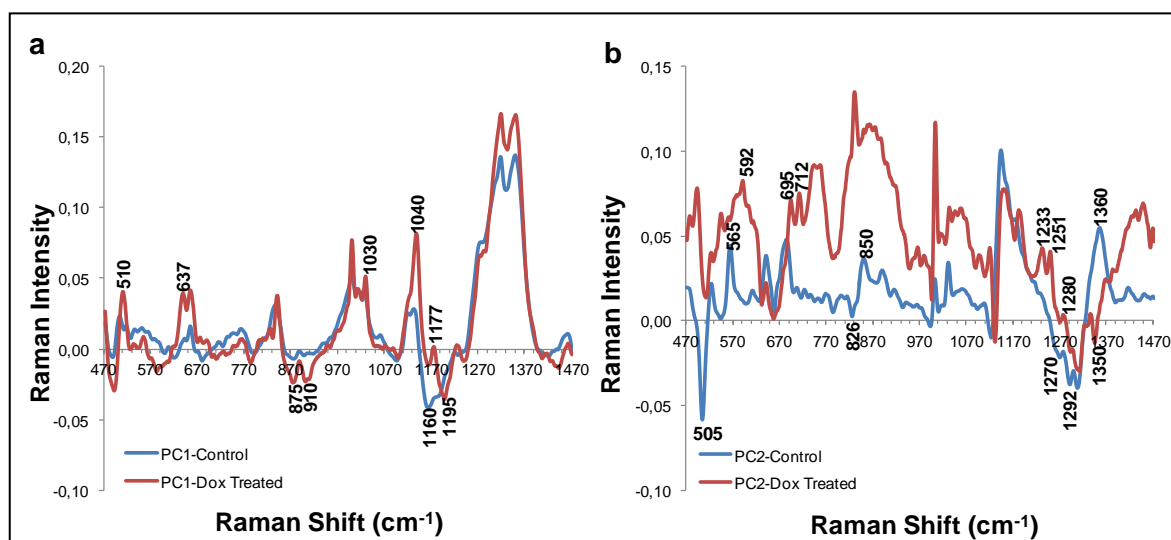
Figure 4.25 Comparison of (a) first and (b) second PCs of control and Dox treated HeLa spheroids with 1000 cells/drop.

LDA was applied to the PCs of the spectra from each control and Dox treated spheroids in order to monitor the spectral similarities intra-layer and compare with the inter-layers of

the spheroids. Figure 4.26-a shows the LDA loading plot according to the different layers of the control spheroid. The PCs of the control spheroids were classified the different layers with 89.6 per cent accuracy. As seen from the plot, the spectra obtained from starting 20 μm to 60 μm depth positions of control spheroid were separated with 96.0, 92.4, 84.0, 82.4, 80.8 per cent of specificity, respectively. LDA loading plot of the different layers of Dox treated spheroid was demonstrated in Figure 4.26-b. The variables of layers were classified with 93.4 per cent accuracy with 97.2, 91.2, 91.2, 90.8, 90.4 per cent specificity starting from 20 μm to 60 μm depth positions.
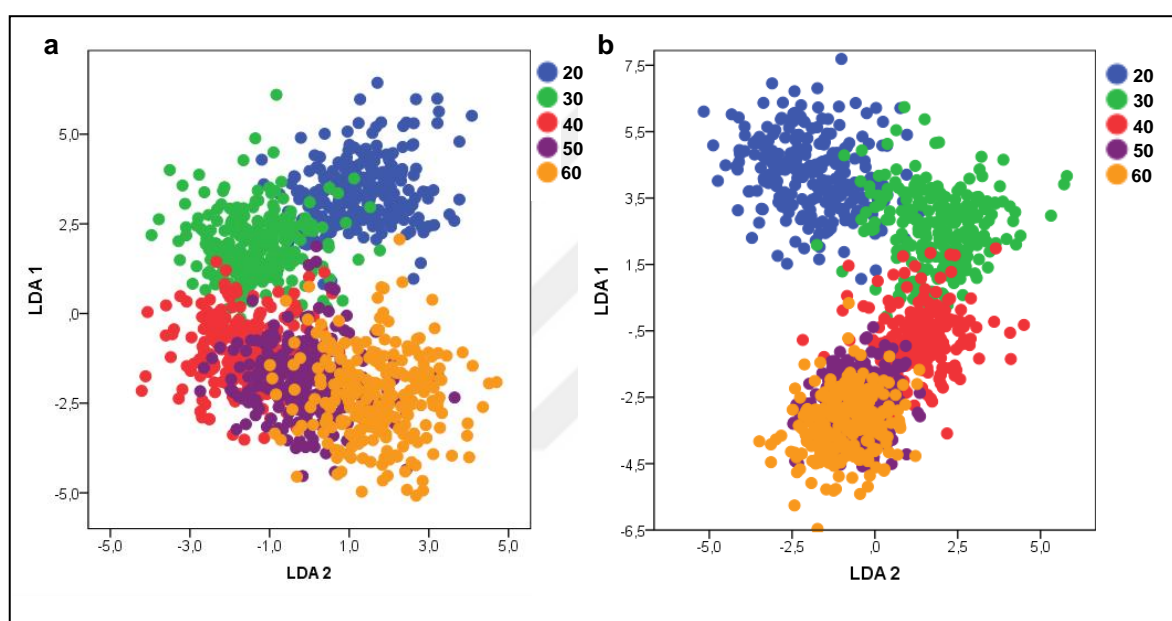
Figure 4.26. LDA plots for the PC components of SERS spectra obtained from the different layers of (a) control and (b) Dox treated HeLa spheroids.

The discrimination of the spectra from the layers of control and Dox treated spheroids were evaluated together using PC-LDA analysis. First of all, the PCs of both group was found. Then, LDA was applied. The first 81 PCs were obtained with 94 per cent of total variance. These PCs were classified with 89.6 per cent of accuracy and the layers of control spheroids starting from 20 μm to 60 μm depth positions were separated with 96.0, 92.4, 84.0, 82.4, 80.8 per cent of specificity while the layers of Dox treated spheroid were classified with 97.2, 91.2, 91.2, 90.8, 90.4 specificity. As seen, the spectra from control and Dox treated spheroids were classified separately in LDA plot in Figure 4.27. The separation of the layers at 20 μm and 30 μm depth positions of Dox treated spheroids from both the other layers and the layers of the control spheroid were clearly observed.
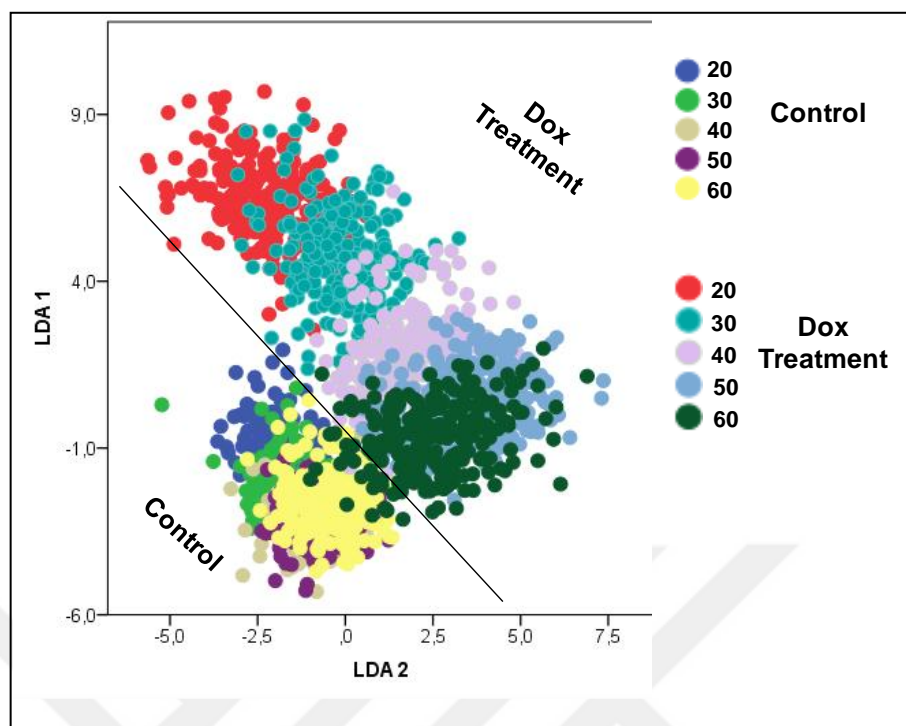
Figure 4.27. LDA plots for the PCs of SERS spectra obtained from the different layers of control and Dox treated HeLa spheroids.

The performance of SERS based spheroid model was also evaluated using the spheroid prepared with 1000 cells/drop in 72 h hanging drop incubation. Similarly, the drug exposure was performed after the spheroids were transferred into the culture plates coated with PDMS. Figure 4.28 shows the spectra obtained from different layers of control and Dox-treated spheroids spheroid. Each spectrum from different layers represents the average of 250 spectra. In the case of control spheroid, minor intensity variations were observed from the spectra obtained from the layers close to the surface between 20 μm to 40 μm depth positions of spheroids while the spectra obtained from the deeper positions were quite similar as seen in Figure 4.28-a. After Dox treatment, the spectral changes were observed especially at the layers close to the outer surface up to 40 μm depth as seen in Figure 4.28-b. However, a few nm shift in some of the peak positions were observed. Briefly, peak intensities at 555 and 581 cm^{-1} originating from cholesterol and phosphotidylinositol, respectively, from cytosolic membrane components and 1055 cm^{-1} corresponding to C-C stretching of lipids apparently increased from 20 μm to 40 μm depth positions of spheroid. In addition, the peak corresponding to cholesterol at 707 cm^{-1} also raised. The changes might be due to the initiation of apoptotic cell death, at which caspase

activation and increased high cytosolic Ca^{2+} cause the cholestrol release and degradation of phospholipid in endosomal membrane structure. The increased peak intensities corresponding to the CH_2 (884 cm^{-1}), hydrophobic side chains of the proteins (755, 1000, 1178 cm^{-1}) and CH deformation (1449 cm^{-1}) were attributed to CH residues of proteins in Amide III region can be sign of the changes in protein structures in endolysosomes. The overall changes in SERS spectral pattern can be explained with the apoptotic cell death. The significant changes in spectral pattern from outer shell towards 40 μm depth may be due to the rate of penetration of Dox through the depth regions of spheroids [273].

Figure 4.28. SERS spectra obtained from different layers of (a) control and (b) Dox treated HeLa spheroids prepared with 1000 cell/drop.

PCs of the spectra obtained from the layers of the each control and Dox treated HeLa spheroids prepared with 1000 cell/drop were evaluated. In case of control spheroids, the first 82 principal components, accounting for 93.8 per cent of the total variance of the original SERS spectra obtained from eight different layers were obtained. The reasonable 29.1, 20.1 and 5.0 per cent variations were observed for PC1, PC2 and PC3, respectively. As seen in PCA plot in Figure 4.29-a, the spectral variables from each layers cannot be well separated with the first three components although the layers close to the outer surface up to 40 μm depth slightly separated from the deeper layers. In case of Dox treated spheroid, the first 80 PCs were obtained from the SERS spectra of eight different layers with the contribution of 93.6 per cent variance. The first, second and third PCs showed 40.4, 16.8 and 4.2 per cent reasonable variations. The separate clustering of the spectra

obtained from the surface towards the 40 µm depth with these three components was clearly seen in Figure 4.29-b.

Figure 4.29. PCA plots for first, second and third components of SERS spectra obtained from different layers of (a) control and (b) Dox treated HeLa spheroids prepared with 1000 cells/drop.

Comparison of PC1 and PC2 scores obtained from each control or Dox treated spheroids prepared with 1000 cells/drop was demonstrated in Figure 4.30. The PC1 of the spectra from control and Dox treated spheroids were compared in Figure 4.30-a. The major variations observed corresponding to the protein, membrane and nucleotide structures at 640 cm^{-1} (C-S stretching and C-C twist mode of proteins), 1142 cm^{-1} (lipids) and 1357 cm^{-1} (guanine) with positive contribution while the peaks at 790 cm^{-1} (O-P-O stretching), 1275 cm^{-1} (Amide III) and 1300 cm^{-1} (fatty acids) were negatively contributed. The major changes after Dox treatment were observed with positive contributions of protein structures at 1160 cm^{-1} (C-C/C-N stretching of proteins), 1200 cm^{-1} (Amide III) and 1238 cm^{-1} (Amide III) and negative contribution of peaks corresponding to membrane structures at 820 cm^{-1} (C-C stretch of proline), 1130 cm^{-1} (phospholipids) and 1310 cm^{-1} (CH$_3$/CH$_2$ twisting or bending mode of lipid). Figure 4.30-a shows the comparison of PC2 scores of control and Dox treated spheroids. Significant difference of the spectra of Dox treated spheroids was observed with the positive contribution of membrane and nucleotide structures at 1130 cm^{-1} (phospholipid), 1140 cm^{-1} (lipids) and 1352 cm^{-1} (guanine) peak positions. The PCs scores demonstrate the difference of the variables of control and Dox treated spheroids. Similar to the comparison of the PCs of control and Dox treated HeLa spheroids, Dox treated spheroid differentiated from the control mostly with the positive

contribution of the peaks corresponding to protein structure while negative contribution of the peaks corresponding to the structural contents of endolysosomal membrane.
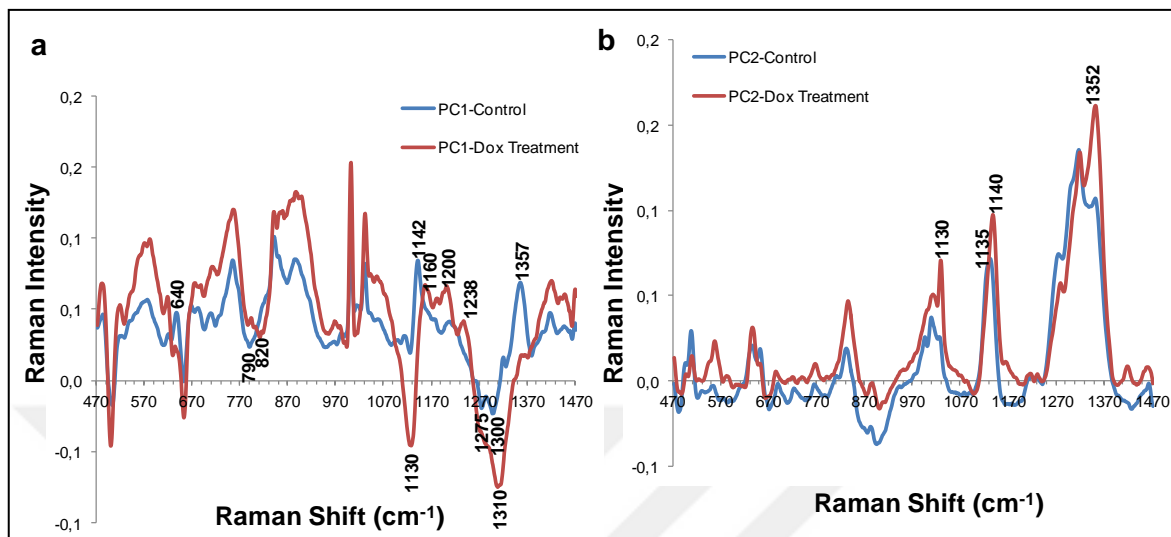
Figure 4.30. Comparison of (a) first and (b) second PCs of the SERS spectra obtained from different layers of control and Dox treated HeLa spheroids prepared with 1000 cells/drop.

LDA was applied to PCs scores of the SERS spectra obtained from eight different layers of each control and Dox treated spheroids. The spectra from the layers of control spheroids were classified with 81.8 per cent accuracy. The classification of the spectra obtained from each layer of control spheroid was shown in Figure 4.31-a. The layers starting from 20 μm to 90 μm were classified with sensitivities of 89.6, 87.6, 87.2, 74.4, 70.8 and 75.9 per cent, respectively. It is clearly seen that the spectra from the layers closer to outer surface up to 40 μm depth are clustered separately while the spectra from the deeper positions of spheroids are not clearly separated. The arbitrary arrangements of AuNP-aggregates throughout the layers of the cells located on the outer surface of a spheroid might be the reason for the spectral variations towards the outer surface. LDA for the first 80 PCs of the spectra from Dox treated spheroid was shown in Figure 4.31-b. The PCs scores of spectra were classified with 77.7 per cent accuracy and the layers starting from 20 μm to 90 μm were separated with 85.6, 77.6, 88.0, 82.0, 80.0, 65.6, 66.2 and 77.9 per cent sensitivity. As seen, similar results were also observed with Dox treated spheroid. The layers close to the surface up to 40 μm depth separated with LDA while the sensitivity of separation decreased as the spectra was collected from the deeper layers of the spheroid.

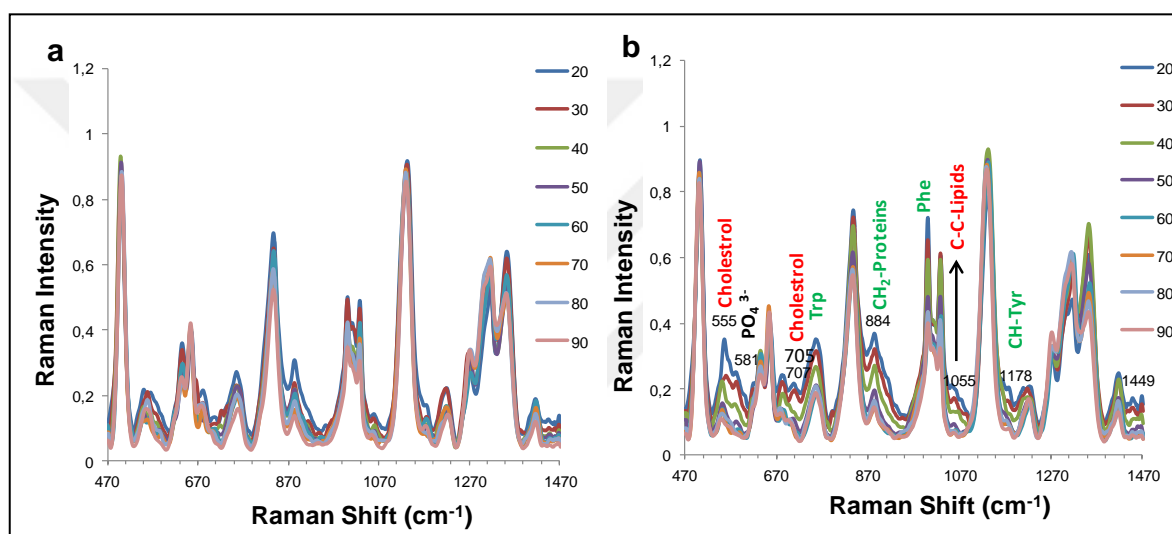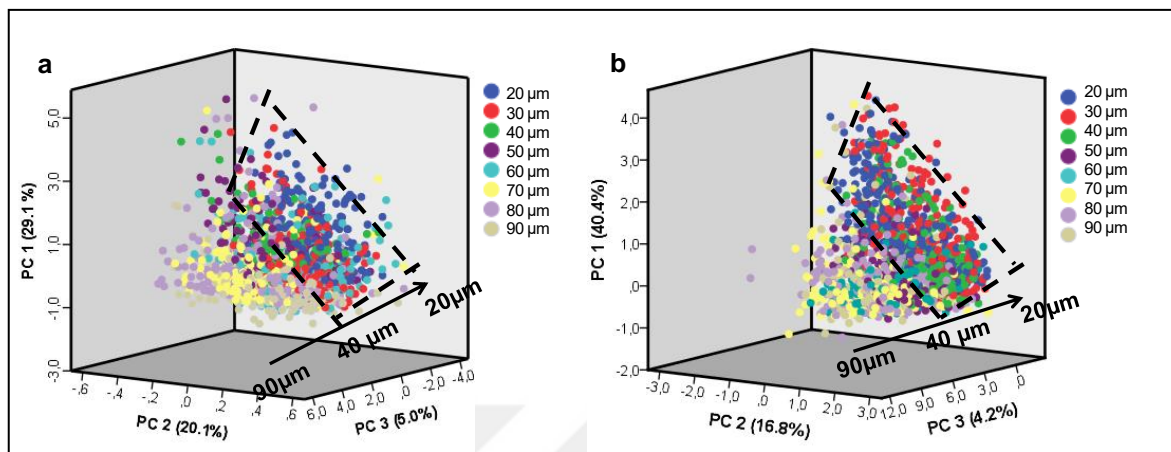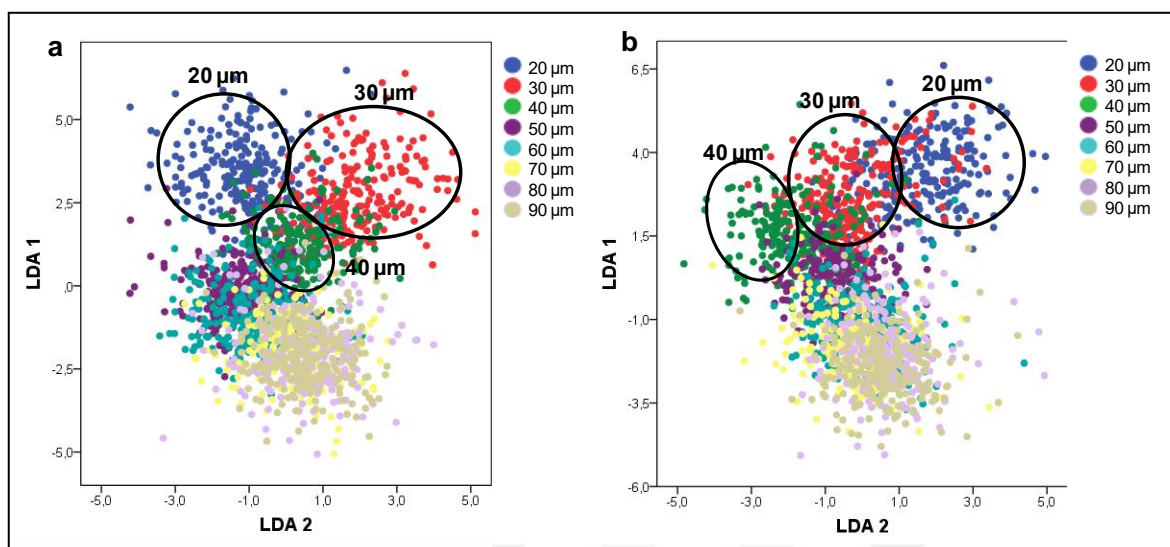Figure 4.31. LDA plots for PC components of SERS spectra obtained from the different layers of (a) control and (b) Dox treated HeLa spheroids prepared with 1000 cells/drop.
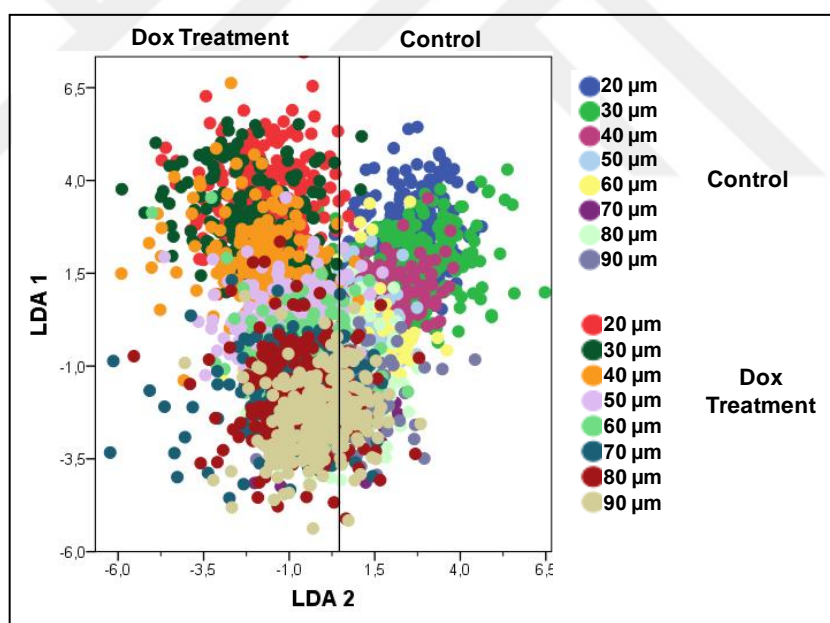
Figure 4.32. LDA plot for the PCs of SERS spectra obtained from the analysis of different layers of control and Dox treated HeLa spheroids prepared with 1000 cells/drop.

LDA was applied for the PCs of SERS spectra obtained from the analysis of different layers of both control and Dox treated HeLa spheroids prepared with 1000 cells/drop. When they were both analyzed, the first 82 PCs were obtained accounting for 93.4 per cent of total variance. The PCs were classified with 72.6 per cent accuracy with 86.4, 82.0, 78.0, 81.2, 71.6, 66.4, 70.3 per cent sensitivity of the control spheroids and 83.2, 72.0,

82.4, 80.0, 69.2, 52.4, 68.4 per cent sensitivity of Dox treated spheroids starting from 20 μm to 90 μm depth positions as seen in Figure 4.32. Although the spectral variations were higher at outer surface, the SERS spectra of the Dox treated spheroids clearly separated from the control.

The performance of SERS based spheroid model on drug testing was also analyzed using HUVEC spheroids. As mentioned above in Figure 4.23-a, HUVEC cells generated more compact and spherical shape of 3D cell aggregates compared to HeLa cells. The spheroids were prepared by using 250 cells/drop initial cell density. After 72 h hanging drop incubation, the spheroids were treated with 5 μM Dox for 24 h, 48 h and 72 h. In each time point, SERS spectra were collected by using same experimental setup as used for HeLa spheroids. Briefly, an area was set with 30 μm in *x*-axis and 45 μm in *y* axis and scanned with 3 μm steps while 80 μm in *z*-axis was set from 20 μm to 90 μm depth with 10 μm intervals for SERS measurements.
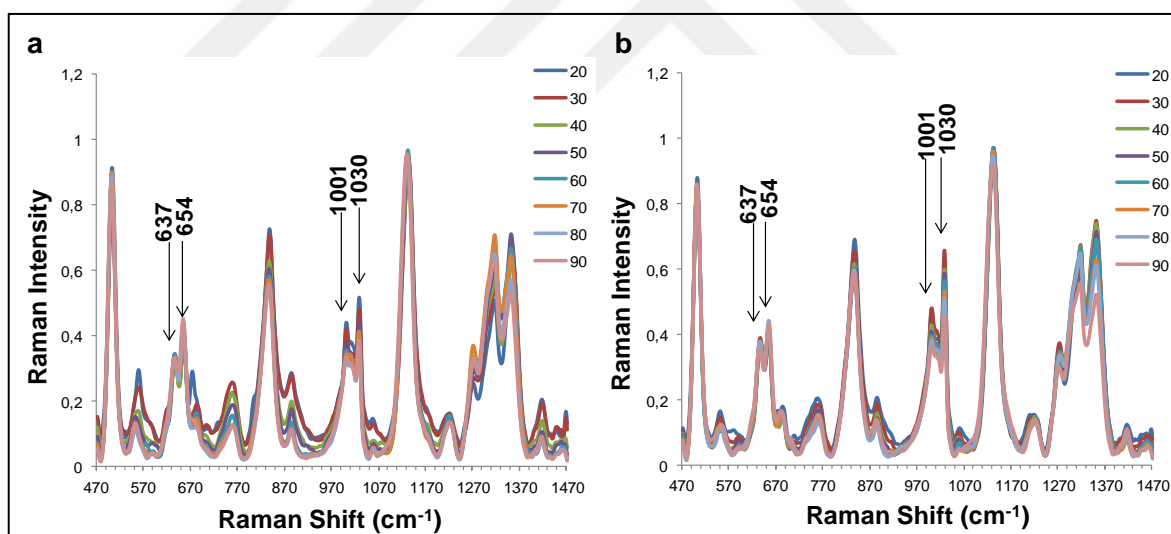
Figure 4.33. SERS spectra from the different layers of (a) control and (b) 24 h Dox treated HUVEC spheroids.

The spectra of each layer of control and 24 h Dox treated HUVEC spheroid were compared with each other as shown in Figure 4.33. The intensity variation of the spectra obtained from the layers close to outer surface of control spheroid was clearly seen in Figure 4.33-a, similarly as the results obtained from HeLa spheroids. However, the spectral pattern throughout the layers were similar. The spectra obtained from the different layers of Dox treated HUVEC spheroid were shown in Figure 4.33-b. The spectral pattern was

similar between the layers. However, the intensities of peaks at 637 cm^{-1} (C-S stretching and C-C twisting mode) and 1030 cm^{-1} (phenylalanine) increased relatively to peaks at 654 cm^{-1} and 1001 cm^{-1}, respectively, indicating the changes in protein structures.

The spectra obtained from different layers of control and 48 h Dox treated HUVEC spheroids were shown in Figure 4.34. As seen in Figure 4.34-a, the spectra obtained from the different layer of control spheroid were quite similar. The spectra of Dox treated spheroids also showed similar pattern throughout the layers. However, the intensities of peaks at 637 cm^{-1}, 1001 cm^{-1} and 1030 cm^{-1} relatively increased.
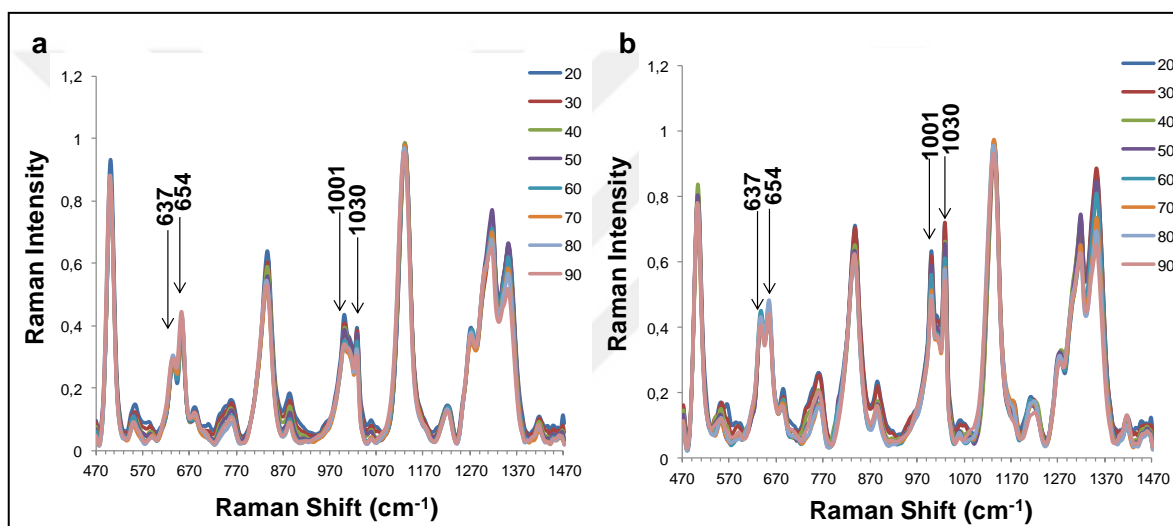
Figure 4.34. SERS spectra from the different layers of (a) control and (b) 48 h Dox treated HUVEC spheroids.

The comparison of SERS spectra from different layers of HUVEC spheroid after 72 h Dox exposure were given in Figure 4.35. The spectra obtained from different layers of control spheroid were shown in Figure 4.35-a. The SERS spectra expressed similar pattern except the 80 μm depth position, which might start to die due to metabolite accumulation or not sufficient nutrient delivery inner zones. After Dox treatment, the spectral pattern obtained from the different layers significantly changed as seen in Figure 4.35-b. The changes in peak positions were similar with the results obtained with Dox treated HeLa spheroids. Briefly, 581 cm^{-1} originating from phosphotidylinositol and 1060 cm^{-1} corresponding to C-C stretching of lipids from cytosolic membrane components increased. The peak corresponding to cholesterol at 709 cm^{-1} also raised while the intensity of phospholipid at 1131 cm^{-1} decreased. The increased peak intensities corresponding to the CH$_2$ (884 cm^{-1}),

hydrophobic side chains of the proteins (1000 cm^{-1}) and CH residues (in Amide III region) deformation (1449 cm^{-1}) can be sign of the changes in protein structures in endolysosomes.

Time dependent overwhelming spectral variables of control and Dox treated HUVEC spheroids for 24, 48 and 72 h depending on the different depth layers were evaluated with PCA. For the first 82 PCs accounting for 94.56 varience was found for 24 h. The PC1 and PC2 were found 26.5 and 20.9 per cent, respectively. In the case for 48 h treatment, the first 72 PCs were found with 94.1 per cent variations. PC1 and PC2 were found 32.5 and 19.7 per cent, respectively. The values of PC1 and PC2 were found 46.2 and 16.4 per cent from 72 PCs accounting for 92.8 per cent of variations. The time dependent comparison of PC1 and PC2 were demonstrated in Figure 4.36. The PC1 scores after 24 and 48 h Dox exposure were similar as seen in Figure 4.36-a. At the 72 h, the major changes were observed with positive contibution of peaks corresponding to membrane structures at 575 cm^{-1} (phosphatidylinositol), 709 cm^{-1} (cholestrol), hydrophobic amino acids at 872 cm^{-1} (Trypthophane), 1001 cm^{-1} (phenylalanine) and secondary structures of proteins at 1197 cm^{-1} (Amide III) and 1240 cm^{-1} (Amide III). The negative contibutions were observed corresponding to disulphate bridges of proteins at 501 cm^{-1} (S-S), membrane structures at 1135 cm^{-1} (fatty acids) and nucleotides attributed to the energy production at 1316 cm^{-1} and 1350 cm^{-1} (Guanine). The time dependent comparison of PC2 scores was demonstrated in Figure 4.36-b. Compared to the 24 h, positive contribution of peak at 1000 cm^{-1} (phenylalanine) was increased at 48 h Dox exposure due to the denaturation of proteins while C-C skelatal structures were negatively contributed. At 72 h, the variations observed due to the positive contribution of peaks at 504 cm^{-1} (S-S), 653 cm^{-1} (Tyrosine), 1135 cm^{-1} (fatty acids) and 1319 cm^{-1} (Guanine) and negative contribution of peaks at 580 cm^{-1} (phosphatidylinositol), 709 cm^{-1} (cholestrol) and 1000 cm^{-1} (phenylalanine).

LDA of the SERS spectra obtained from different depth layers of control and time dependent Dox treatment of HUVEC spheroids was demonstrated in Figure 4.37. As seen, the spectra from the different layers of control and Dox treated spheroids were separately clustered upto 40 µm depth after 24 h treatment. The results indicated that Dox penetrated into about 60 µm depth for 24 h. However, the spectra from layers of the control and Dox treated spheroids seperately clustered further incubations to 48 h probably due to complete diffusion of Dox into the spheroid. For 72 h exposure, the spectral changes caused not only

seperation from the control spheroids but also the layers of the Dox treated spheroids upto 60 µm depth.
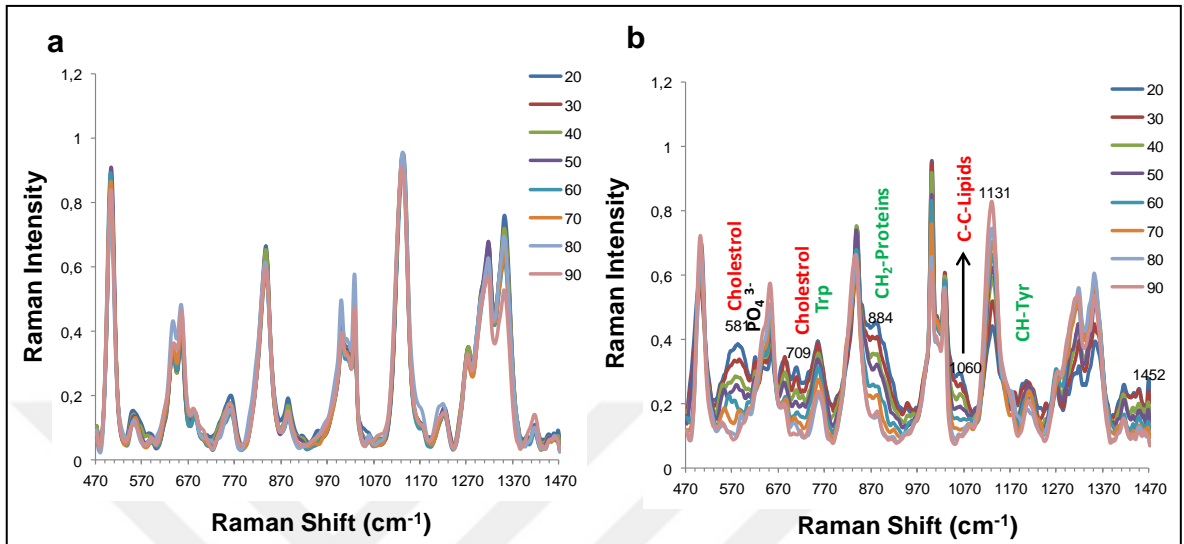
Figure 4.35. SERS spectra from the different layers of (a) control and (b) 72 h Dox treated HUVEC spheroids.
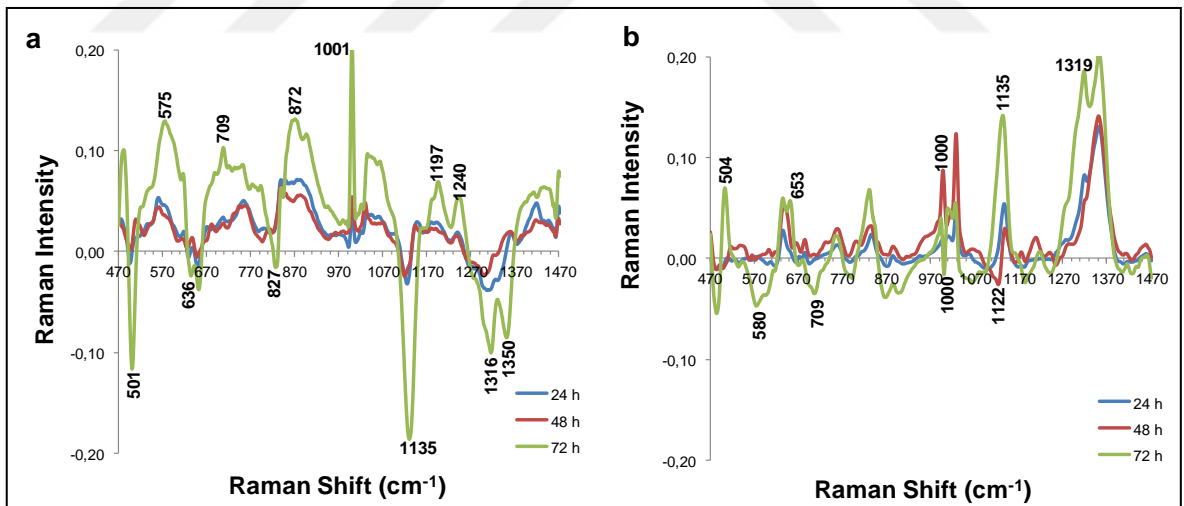
Figure 4.36. Comparison of (a) PC1 and (b) PC2 scores produced by the analysis of SERS spectra obtained from different layers of control and Dox treated HUVEC spheroids for 24 h, 48 h and 72 h incubation times.
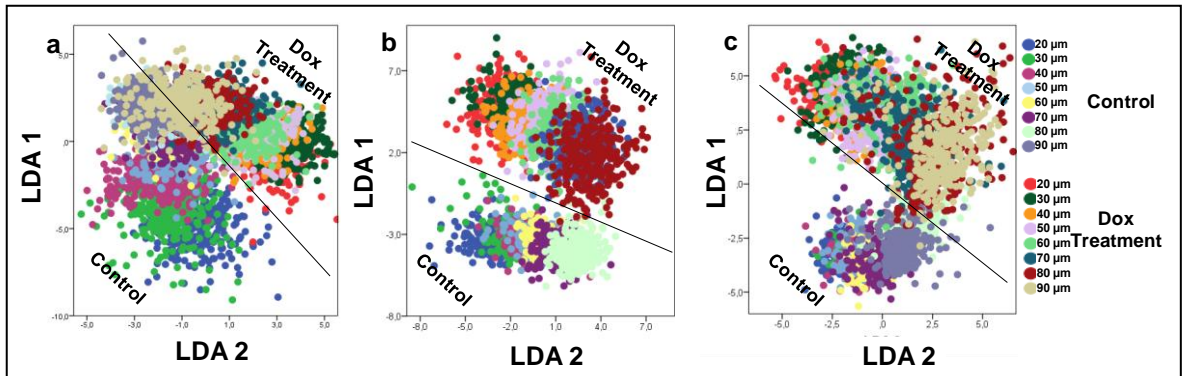
Figure 4.37. LDA for PCs of SERS spectra obtained from the analysis of different layers of control and Dox treated HUVEC spheroids for (a) 24 h, (b) 48 h and (c) 72 h incubation times.

5. CONCLUSIONS AND FUTURE PERSPECTIVES

Current methods used to analyze 3D tissue cultures do not permit to gather biochemical information from 3D culture systems without destruction, which limits observing spatial and temporal biochemical information. SERS is evolving as novel and attractive technique for living cell analysis due to higher sensitivity and nondestructive nature. Although it may not possible to obtain the signal from targeted molecule, dynamic changes in molecular structures in the close vicinity of SERS substrates can provide voluble information about the cellular processes. In this study, a label free and non-destructive SERS based approach for the analysis of 3D culture model is demonstrated. The optimization of SERS based experimental parameters for living cell analysis is critical to escape from the experimental based variations and to obtain reliable spectral information. Therefore, the measurement based parameters of SERS such as laser power, objective selection and focus adjustment for living cell are first optimized in monolayer culture. A 150 mW laser power with 2 s of 830 nm excitation laser wavelength by focusing 20×long distance objective is decided for the living cell acquisitions due to increased S/N and to decrease the possible effect of photo-induced damage on cells for longer times of analysis. However, it is important to adjust a deeper focus on cell surface during SERS measurement since the above or below of the focal point cause intensity based variations. The aggregation of AuNPs, localization and endolysosomal processes may also cause spectral variations. Increased incubation times and post-incubation times showed that the AuNPs trapped in endolysosomal compartments provided the same spectral information . The statistically significant spectral changes are observed when the cells are induced to death upon treatment with anticancer drugs indicating that the SERS based living cell analysis provides information about the biochemical changes without any contribution of instrumental or substrate based bias.

The preparation of SERS based 3D culture is quite simple. First, AuNPs with 50 nm in average size are introduced into cells by simply addition into the cell culture medium in monolayer culture. Then, 3D spheroid culture is formed in hanging drop without using any special equipment. The AuNPs are found accumulated in the endolysosomal vesicles of the cells and transferred from the mother cell to daughter cell during formation of 3D culture.

SERS based 3D culture provided spectral information from the cells residing in different layers of the spheroids and gave information about the apoptotic cell death induced biochemical changes in endolysosomal compartments upon Dox treatment. The increased peak intensities corresponding to cholesterol and phosphotidylinositol components of membrane at 555 cm^{-1}, 590 cm^{-1}, 705 cm^{-1} and 1060 cm^{-1} were attributed to the endolysosomal membrane destabilization due to caspase activation and high cytosolic Ca^{2+}. The upregulation of proteins in endosomes inducing the changes in the peak intensities at 882 cm^{-1}, 756 cm^{-1}, 1001 cm^{-1}, 1352 cm^{-1} and 1450 cm^{-1} were also observed. The spectral changes were observed mostly from the layers close to the outer surface of the spheroids due to the penetration rate of Dox. The changes in spectral pattern differentiated statistically with PC-LDA. The analysis showed that the spectra from different layer of a same spheroid change due to the possibility of different spatial arrangements of AuNPs aggregates at the different same layers. Notwithstanding the statistical differences in the spectra of the same spheroid, the control and Dox treated spheroids were effectively classified. The spectral changes were also statistically responsive to the different layers of spheroid according to drug penetration depth in a time dependent manner and increased drug accumulation towards the surface of the spheroids.

In conclusion, SERS based 3D culture model can be useful to test not only cancer but also other types of drugs. It is nondestructive, easy to utilize and fast. With this approach experimental deviations resulting from human errors are expected to be lower than the other molecular techniques have, which heavily involve human based experimental procedures. One should note that the proposed approach is not limited to monitoring cell death. SERS based 3D culture can be extended for the evaluation of other cellular functions upon external stimuli as well. The cellular differentiation, metastasis or disease progression can also be monitored. In such cases, it is important to realize the relation between biochemical processes in other cellular compartments and an endolysosomal system. In this study, 50 nm of spherical AuNPs are used as SERS substrates. However, it is also possible to use different shape and size of AuNPs for customized plasmonic properties or to modify the surface chemistry of the AuNPs for organelle or molecular targeted use. A new instrument can also be built for continues monitoring of spheroids by combining a Raman spectrometer and a CO_2 incubator to extend the use of the approach.

Although the approach has the above mentioned advantages and futuristic uses, it has also challenges pertaining to both the 3D sample preparation and spectral interpretation. First of all, AuNPs accommodating in endolysosomes when the cells are exposed to anti-cancer drug can change the action of drug by the interaction. For example, in our study, the cytotoxicity of doxorubicin and cisplatin increased the cytotoxicity about 7-10%. Second, the size and shape of spheroids have a strong role in the interaction of drug with spheroid surface and penetration rate, which can change the spectral outcome at depth positions. Therefore, similar size and shape must be selected for evaluation. For example, spectral results obtained from spherical or elliptical shaped spheroids can change due to the diffusion rate of drugs. The other challenge is the reproducibility of spectra obtained from each layers, which strongly depends on the number of obtained spectra. Since the spectra were collected without fixation of the spheroid, the prolonged measurement time can cause heat-induced damage on a spheroid, evaporation of culture medium and crystallization of the spheroid. In order to overcome the limitations, scanned depth can be reduced or minimum number of spectra should be collected. Another challenge is the interpretation of the SERS spectra after drug exposure. It is necessary to figure out the spectral signatures for autophagic or necrotic cell death in order to conclude that the observed result is cell death. Another important point to pay attention is possible spectral interference originating from the tested drug. Finally, the difference in endolysosomal pathway in different diseases. Depending on the disease type, gene expression level of cell membrane components varies. This may influence the endolysosome content, where we think that SERS signal originates. Thus, the cell type dependent changes may affect corresponding cell death spectral pattern.

REFERENCES

1.   Jacobson MD, Weil M, Raff MC. Programmed cell death in animal development. Cell. 1997;88(3):347-54.

2.   Vaux DL, Korsmeyer SJ. Cell death in development. Cell. 1999;96(2):245-54.

3.   Horvitz HR. Genetic control of programmed cell death in the nematode Caenorhabditis elegans. Cancer research. 1999;59(7 Supplement):1701s-6s.

4.   Levine B, Kroemer G. Autophagy in the pathogenesis of disease. Cell. 2008;132(1):27-42.

5.   Kroemer G, Galluzzi L, Vandenabeele P, Abrams J, Alnemri E, Baehrecke E, et al. Classification of cell death: recommendations of the Nomenclature Committee on Cell Death 2009. Cell Death & Differentiation. 2009;16(1):3-11.

6.   Vandenabeele P, Galluzzi L, Berghe TV, Kroemer G. Molecular mechanisms of necroptosis: an ordered cellular explosion. Nature reviews Molecular cell biology. 2010;11(10):700-14.

7.   Grumati P, Coletto L, Sabatelli P, Cescon M, Angelin A, Bertaggia E, et al. Autophagy is defective in collagen VI muscular dystrophies, and its reactivation rescues myofiber degeneration. Nature medicine. 2010;16(11):1313-20.

8.   Obeid M, Tesniere A, Ghiringhelli F, Fimia GM, Apetoh L, Perfettini J-L, et al. Calreticulin exposure dictates the immunogenicity of cancer cell death. Nature medicine. 2007;13(1):54-61.

9.   Zitvogel L, Kepp O, Kroemer G. Decoding cell death signals in inflammation and immunity. Cell. 2010;140(6):798-804.

10.   Ricci MS, Zong W-X. Chemotherapeutic approaches for targeting cell death pathways. The oncologist. 2006;11(4):342-57.

11.   Parrino J, Hotchkiss RS, Bray M. Prevention of immune cell apoptosis as potential therapeutic strategy for severe infections. Emerg Infect Dis. 2007;13(2):191-8.

12.   Gottlieb RA. Cell death pathways in acute ischemia/reperfusion injury. Journal of cardiovascular pharmacology and therapeutics. 2011;16(3-4):233-8.

13.   Wong RS. Apoptosis in cancer: from pathogenesis to treatment. Journal of Experimental & Clinical Cancer Research. 2011;30(1):87.

14.   Toscano M, Palumbo S, Tini P, Miracco C, Gravina GL, Comincini S. Cell Death Pathways, with Special Regard to Ionizing Radiation and Temozolomide. Radiobiology of Glioblastoma: Springer; 2016. p. 209-24.

15.   Ocana A, Pandiella A. Novel Synthetic Lethality Approaches for Drug Combinations and Early Drug Development. Current cancer drug targets. 2017;17(1):48-52.

16.   Czeizler E, Gratie C, Chiu WK, Kanhaiya K, Petre I, editors. Target Controllability of Linear Networks. International Conference on Computational Methods in Systems Biology; 2016: Springer.

17.   Kerr JF, Wyllie AH, Currie AR. Apoptosis: a basic biological phenomenon with wide-ranging implications in tissue kinetics. British journal of cancer. 1972;26(4):239.

18.   Kerr JF. History of the events leading to the formulation of the apoptosis concept. Toxicology. 2002;181:471-4.

19.   Elmore S. Apoptosis: a review of programmed cell death. Toxicologic pathology. 2007;35(4):495-516.

20.	Häcker G. The morphology of apoptosis. Cell and tissue research. 2000;301(1):5-17.

21.	Aree K. Clearance of apoptotic cells by phagocytes. Thammasat Medical Journal. 2013;13(1):89-97.

22.	Liu Y, Levine B. Autosis and autophagic cell death: the dark side of autophagy. Cell Death & Differentiation. 2015;22(3):367-76.

23.	Sibirny A, Subramani S, Thumm M, Veenhuis M, Ohsumi Y. A unified nomenclature for yeast autophagy-related genes. Dev Cell. 2003;5:539545Klionsky.

24.	Mizushima N, Levine B, Cuervo AM, Klionsky DJ. Autophagy fights disease through cellular self-digestion. Nature. 2008;451(7182):1069-75.

25.	Rabinowitz JD, White E. Autophagy and metabolism. Science. 2010;330(6009):1344-8.

26.	Mizushima N, Yamamoto A, Matsui M, Yoshimori T, Ohsumi Y. In vivo analysis of autophagy in response to nutrient starvation using transgenic mice expressing a fluorescent autophagosome marker. Molecular biology of the cell. 2004;15(3):1101-11.

27.	Murrow L, Debnath J. Autophagy as a stress-response and quality-control mechanism: implications for cell injury and human disease. Annual Review of Pathology: Mechanisms of Disease. 2013;8:105-37.

28.	Tanida I, Ueno T, Kominami E. LC3 and Autophagy. Autophagosome and Phagosome. 2008:77-88.

29.	Golstein P, Kroemer G. Cell death by necrosis: towards a molecular definition. Trends in biochemical sciences. 2007;32(1):37-43.

30. Festjens N, Berghe TV, Vandenabeele P. Necrosis, a well-orchestrated form of cell demise: signalling cascades, important mediators and concomitant immune response. Biochimica et Biophysica Acta (BBA)-Bioenergetics. 2006;1757(9):1371-87.

31. Hirsch T, Marchetti P, Susin SA, Dallaporta B, Zamzami N, Marzo I, et al. The apoptosis-necrosis paradox. Apoptogenic proteases activated after mitochondrial permeability transition determine the mode of cell death. Oncogene. 1997;15(13):1573-81.

32. Zeiss C. The apoptosis-necrosis continuum: insights from genetically altered mice. Veterinary Pathology. 2003;40(5):481-95.

33. Berghe TV, Vanlangenakker N, Parthoens E, Deckers W, Devos M, Festjens N, et al. Necroptosis, necrosis and secondary necrosis converge on similar cellular disintegration features. Cell Death & Differentiation. 2010;17(6):922-30.

34. Berghe TV, Linkermann A, Jouan-Lanhouet S, Walczak H, Vandenabeele P. Regulated necrosis: the expanding network of non-apoptotic cell death pathways. Nature reviews Molecular cell biology. 2014;15(2):135-47.

35. Whitehurst AW, Bodemann BO, Cardenas J, Ferguson D, Girard L, Peyton M, et al. Synthetic lethal screen identification of chemosensitizer loci in cancer cells. Nature. 2007;446(7137):815.

36. Melzer S, Nunes CSM, Endringer DC, de Andrade TU, Tarnok A, Lenz D. Trypan blue as an affordable marker for automated live-dead cell analysis in image cytometry. Scanning. 2016;38(6):857-63.

37. MacIntyre HL, Cullen JJ. Classification of phytoplankton cells as live or dead using the vital stains fluorescein diacetate and 5-chloromethylfluorescein diacetate. Journal of phycology. 2016;52(4):572-89.

38. Gillissen M, Yasuda E, de Jong G, Levie S, Go D, Spits H, et al. The modified FACS calcein AM retention assay: A high throughput flow cytometer based method to measure cytotoxicity. Journal of immunological methods. 2016;434:16-23.

39.   Crowley LC, Scott AP, Marfell BJ, Boughaba JA, Chojnowski G, Waterhouse NJ. Measuring cell death by propidium iodide uptake and flow cytometry. Cold Spring Harbor Protocols. 2016;2016(7):pdb. prot087163.

40.   Kepp O, Galluzzi L, Lipinski M, Yuan J, Kroemer G. Cell death assays for drug discovery. Nature reviews Drug discovery. 2011;10(3):221-37.

41.   Galluzzi L, Vitale I, Abrams J, Alnemri E, Baehrecke E, Blagosklonny M, et al. Molecular definitions of cell death subroutines: recommendations of the Nomenclature Committee on Cell Death 2012. Cell Death & Differentiation. 2012;19(1):107-20.

42.   Vermes I, Haanen C, Steffens-Nakken H, Reutellingsperger C. A novel assay for apoptosis flow cytometric detection of phosphatidylserine expression on early apoptotic cells using fluorescein labelled annexin V. Journal of immunological methods. 1995;184(1):39-51.

43.   Galluzzi L, Aaronson S, Abrams J, Alnemri E, Andrews D, Baehrecke E, et al. Guidelines for the use and interpretation of assays for monitoring cell death in higher eukaryotes. Cell Death & Differentiation. 2009;16(8):1093-107.

44.   Steff AM, Fortin M, Arguin C, Hugo P. Detection of a decrease in green fluorescent protein fluorescence for the monitoring of cell death: An assay amenable to high-throughput screening technologies. Cytometry Part A. 2001;45(4):237-43.

45.   Resch-Genger U, Grabolle M, Cavaliere-Jaricot S, Nitschke R, Nann T. Quantum dots versus organic dyes as fluorescent labels. Nature methods. 2008;5(9):763-75.

46.   Luo S, Zhang E, Su Y, Cheng T, Shi C. A review of NIR dyes in cancer targeting and imaging. Biomaterials. 2011;32(29):7127-38.

47.   Riss TL, Moravec RA, Niles AL, Duellman S, Benink HA, Worzella TJ, et al. Cell viability assays. 2016.

48.   Simeonov A, Davis MI. Interference with fluorescence and absorbance. 2015.

49.   Smilkstein M, Sriwilaijaroen N, Kelly JX, Wilairat P, Riscoe M. Simple and inexpensive fluorescence-based technique for high-throughput antimalarial drug screening. Antimicrobial agents and chemotherapy. 2004;48(5):1803-6.

50.   Niles AL, Moravec RA, Riss TL. In vitro viability and cytotoxicity testing and same-well multi-parametric combinations for high throughput screening. Curr Chem Genomics. 2009;3(33):e41.

51.   Boydston-White S, Gopen T, Houser S, Bargonetti J, Diem M. Infrared spectroscopy of human tissue. V. Infrared spectroscopic studies of myeloid leukemia (ML-1) cells at different phases of the cell cycle. Biospectroscopy. 1999;5(4):219-27.

52.   Holman HYN, Martin MC, Blakely EA, Bjornstad K, McKinney WR. IR spectroscopic characteristics of cell cycle and cell death probed by synchrotron radiation based Fourier transform IR spectromicroscopy. Biopolymers. 2000;57(6):329-35.

53.   Holman H-YN, Goth-Goldstein R, Martin MC, Russell ML, McKinney WR. Low-dose responses to 2, 3, 7, 8-tetrachlorodibenzo-p-dioxin in single living human cells measured by synchrotron infrared spectromicroscopy. Environmental science & technology. 2000;34(12):2513-7.

54.   Raman C, Krishnan K. hv o hv. Nature. 1928;121:501.

55.   Movasaghi Z, Rehman S, Rehman IU. Raman spectroscopy of biological tissues. Applied Spectroscopy Reviews. 2007;42(5):493-541.

56.   Downes A, Elfick A. Raman spectroscopy and related techniques in biomedicine. Sensors. 2010;10(3):1871-89.

57.   Ellis DI, Cowcher DP, Ashton L, O'Hagan S, Goodacre R. Illuminating disease and enlightening biomedicine: Raman spectroscopy as a diagnostic tool. Analyst. 2013;138(14):3871-84.

58. Fleischmann M, Hendra PJ, McQuillan AJ. Raman spectra of pyridine adsorbed at a silver electrode. Chemical Physics Letters. 1974;26(2):163-6.

59. Jeanmaire DL, Van Duyne RP. Surface Raman spectroelectrochemistry: Part I. Heterocyclic, aromatic, and aliphatic amines adsorbed on the anodized silver electrode. Journal of Electroanalytical Chemistry and Interfacial Electrochemistry. 1977;84(1):1-20.

60. Stiles PL, Dieringer JA, Shah NC, Van Duyne RP. Surface-enhanced Raman spectroscopy. Annu Rev Anal Chem. 2008;1:601-26.

61. Jensen L, Aikens CM, Schatz GC. Electronic structure methods for studying surface-enhanced Raman scattering. Chemical Society Reviews. 2008;37(5):1061-73.

62. Morton SM, Jensen L. Understanding the molecule− surface chemical coupling in SERS. Journal of the American Chemical Society. 2009;131(11):4090-8.

63. Doering WE, Nie S. Single-molecule and single-nanoparticle SERS: examining the roles of surface active sites and chemical enhancement. The Journal of Physical Chemistry B. 2002;106(2):311-7.

64. Qian X-M, Nie S. Single-molecule and single-nanoparticle SERS: from fundamental mechanisms to biomedical applications. Chemical Society Reviews. 2008;37(5):912-20.

65. Zrimsek AB, Wong NL, Van Duyne RP. Single Molecule surface-enhanced raman spectroscopy: a critical analysis of the bianalyte versus isotopologue proof. The Journal of Physical Chemistry C. 2016;120(9):5133-42.

66. Lee HM, Jin SM, Kim HM, Suh YD. Single-molecule surface-enhanced Raman spectroscopy: a perspective on the current status. Physical Chemistry Chemical Physics. 2013;15(15):5276-87.

67.   Israelsen ND, Hanson C, Vargis E. Nanoparticle properties and synthesis effects on surface-enhanced Raman scattering enhancement factor: an introduction. The Scientific World Journal. 2015;2015.

68.   Connor EE, Mwamuka J, Gole A, Murphy CJ, Wyatt MD. Gold nanoparticles are taken up by human cells but do not cause acute cytotoxicity. Small. 2005;1(3):325-7.

69.   Kneipp K, Kneipp H, Kneipp J. Surface-enhanced Raman scattering in local optical fields of silver and gold nanoaggregates from single-molecule Raman spectroscopy to ultrasensitive probing in live cells. Accounts of chemical research. 2006;39(7):443-50.

70.   Kneipp K, Haka AS, Kneipp H, Badizadegan K, Yoshizawa N, Boone C, et al. Surface-enhanced Raman spectroscopy in single living cells using gold nanoparticles. Applied Spectroscopy. 2002;56(2):150-4.

71.   Kang B, Austin LA, El-Sayed MA. Real-time molecular imaging throughout the entire cell cycle by targeted plasmonic-enhanced Rayleigh/Raman spectroscopy. Nano letters. 2012;12(10):5369-75.

72.   Palonpon AF, Ando J, Yamakoshi H, Dodo K, Sodeoka M, Kawata S, et al. Raman and SERS microscopy for molecular imaging of live cells. Nature protocols. 2013;8(4):677-92.

73.   Levy R, Shaheen U, Cesbron Y, See V. Gold nanoparticles delivery in mammalian live cells: a critical review. Nano reviews. 2010;1(1):4889.

74.   Zhang S, Li J, Lykotrafitis G, Bao G, Suresh S. Size-dependent endocytosis of nanoparticles. Advanced materials. 2009;21(4):419-24.

75.   Cho EC, Zhang Q, Xia Y. The effect of sedimentation and diffusion on cellular uptake of gold nanoparticles. Nature nanotechnology. 2011;6(6):385-91.

76.   Alkilany AM, Nagaria PK, Hexel CR, Shaw TJ, Murphy CJ, Wyatt MD. Cellular uptake and cytotoxicity of gold nanorods: molecular origin of cytotoxicity and surface effects. Small. 2009;5(6):701-8.

77.   Chithrani BD, Ghazani AA, Chan WC. Determining the size and shape dependence of gold nanoparticle uptake into mammalian cells. Nano letters. 2006;6(4):662-8.

78.   Kneipp J. Nanosensors based on SERS for applications in living cells. Surface-Enhanced Raman Scattering: Springer; 2006. p. 335-49.

79.   Kneipp J, Kneipp H, McLaughlin M, Brown D, Kneipp K. In vivo molecular probing of cellular compartments with gold nanoparticles and nanoaggregates. Nano letters. 2006;6(10):2225-31.

80.   Kneipp J, Kneipp H, Wittig B, Kneipp K. Novel optical nanosensors for probing and imaging live cells. Nanomedicine: Nanotechnology, Biology and Medicine. 2010;6(2):214-26.

81.   Kneipp J, Kneipp H, Wittig B, Kneipp K. Following the dynamics of pH in endosomes of live cells with SERS nanosensors. The Journal of Physical Chemistry C. 2010;114(16):7421-6.

82.   Huefner A, Kuan W-L, Barker RA, Mahajan S. Intracellular SERS nanoprobes for distinction of different neuronal cell types. Nano letters. 2013;13(6):2463-70.

83.   Kang JW, So PT, Dasari RR, Lim D-K. High resolution live cell Raman imaging using subcellular organelle-targeting SERS-sensitive gold nanoparticles with highly narrow intra-nanogap. Nano letters. 2015;15(3):1766-72.

84.   Huang X, Kang B, Qian W, Mackey MA, Chen PC, Oyelere AK, et al. Comparative study of photothermolysis of cancer cells with nuclear-targeted or cytoplasm-targeted gold nanospheres: continuous wave or pulsed lasers. Journal of biomedical optics. 2010;15(5):058002--7.

85.   Candeloro P, Tirinato L, Malara N, Fregola A, Casals E, Puntes V, et al. Nanoparticle microinjection and Raman spectroscopy as tools for nanotoxicology studies. Analyst. 2011;136(21):4402-8.

86.   Wang Y, Seebald JL, Szeto DP, Irudayaraj J. Biocompatibility and biodistribution of surface-enhanced Raman scattering nanoprobes in zebrafish embryos: in vivo and multiplex imaging. Acs Nano. 2010;4(7):4039-53.

87.   Lin J, Chen R, Feng S, Li Y, Huang Z, Xie S, et al. Rapid delivery of silver nanoparticles into living cells by electroporation for surface-enhanced Raman spectroscopy. Biosensors and Bioelectronics. 2009;25(2):388-94.

88.   Yu Y, Lin J, Wu Y, Feng S, Li Y, Huang Z, et al. Optimizing electroporation assisted silver nanoparticle delivery into living C666 cells for surface-enhanced Raman spectroscopy. Journal of Spectroscopy. 2011;25(1):13-21.

89.   Austin LA, Kang B, El-Sayed MA. A new nanotechnology technique for determining drug efficacy using targeted plasmonically enhanced single cell imaging spectroscopy. Journal of the American Chemical Society. 2013;135(12):4688-91.

90.   Aioub M, El-Sayed MA. A Real-Time Surface Enhanced Raman Spectroscopy Study of Plasmonic Photothermal Cell Death Using Targeted Gold Nanoparticles. Journal of the American Chemical Society. 2016;138(4):1258-64.

91.   Thoma CR, Zimmermann M, Agarkova I, Kelm JM, Krek W. 3D cell culture systems modeling tumor growth determinants in cancer target discovery. Advanced drug delivery reviews. 2014;69:29-41.

92.   Kimlin LC, Casagrande G, Virador VM. In vitro three-dimensional (3D) models in cancer research: an update. Molecular carcinogenesis. 2013;52(3):167-82.

93.   Baker BM, Chen CS. Deconstructing the third dimension–how 3D culture microenvironments alter cellular cues. J Cell Sci. 2012;125(13):3015-24.

94.   Wartenberg M, Ling FC, Müschen M, Klein F, Acker H, Gassmann M, et al. Regulation of the multidrug resistance transporter P-glycoprotein in multicellular tumor spheroids by hypoxia-inducible factor (HIF-1) and reactive oxygen species. The FASEB journal. 2003;17(3):503-5.

95.   Thakor FK, Wan K-W, Welsby PJ, Welsby G. Pharmacological effects of asiatic acid in glioblastoma cells under hypoxia. Molecular and Cellular Biochemistry. 2017;430(1):179.

96.   Minchinton AI, Tannock IF. Drug penetration in solid tumours. Nature Reviews Cancer. 2006;6(8):583-92.

97.   Waite CL, Roth CM. Nanoscale drug delivery systems for enhanced drug penetration into solid tumors: current progress and opportunities. Critical Reviews™ in Biomedical Engineering. 2012;40(1).

98.   Tung Y-C, Hsiao AY, Allen SG, Torisawa Y-s, Ho M, Takayama S. High-throughput 3D spheroid culture and drug testing using a 384 hanging drop array. Analyst. 2011;136(3):473-8.

99.   Chen S-F, Chang Y-C, Nieh S, Liu C-L, Yang C-Y, Lin Y-S. Nonadhesive culture system as a model of rapid sphere formation with cancer stem cell properties. PloS one. 2012;7(2):e31864.

100.   Lovitt CJ, Shelper TB, Avery VM. Advanced cell culture techniques for cancer drug discovery. Biology. 2014;3(2):345-67.

101.   Hongisto V, Jernström S, Fey V, Mpindi J-P, Sahlberg KK, Kallioniemi O, et al. High-throughput 3D screening reveals differences in drug sensitivities between culture models of JIMT1 breast cancer cells. PloS one. 2013;8(10):e77232.

102.   Pampaloni F, Reynaud EG, Stelzer EH. The third dimension bridges the gap between cell culture and live tissue. Nature reviews Molecular cell biology. 2007;8(10):839-45.

103.   Friedrich J, Seidel C, Ebner R, Kunz-Schughart LA. Spheroid-based drug screen: considerations and practical approach. Nature protocols. 2009;4(3):309-24.

104.   Wen Z, Liao Q, Hu Y, You L, Zhou L, Zhao Y. A spheroid-based 3-D culture model for pancreatic cancer drug testing, using the acid phosphatase assay. Brazilian journal of medical and biological research. 2013;46(7):634-42.

105.   Costa EC, Moreira AF, de Melo-Diogo D, Gaspar VM, Carvalho MP, Correia IJ. 3D tumor spheroids: an overview on the tools and techniques used for their analysis. Biotechnology advances. 2016;34(8):1427-41.

106.   Celli JP, Rizvi I, Blanden AR, Massodi I, Glidden MD, Pogue BW, et al. An imaging-based platform for high-content, quantitative evaluation of therapeutic response in 3D tumour models. Scientific reports. 2014;4:3751.

107.   Zanoni M, Piccinini F, Arienti C, Zamagni A, Santi S, Polico R, et al. 3D tumor spheroid models for in vitro therapeutic screening: a systematic approach to enhance the biological relevance of data obtained. Scientific reports. 2016;6.

108.   Kim T-H, Mount CW, Gombotz WR, Pun SH. The delivery of doxorubicin to 3-D multicellular spheroids and tumors in a murine xenograft model using tumor-penetrating triblock polymeric micelles. Biomaterials. 2010;31(28):7386-97.

109.   Ichim G, Tait SW. A fate worse than death: apoptosis as an oncogenic process. Nature Reviews Cancer. 2016.

110.   Czabotar PE, Lessene G, Strasser A, Adams JM. Control of apoptosis by the BCL-2 protein family: implications for physiology and therapy. Nature reviews Molecular cell biology. 2014;15(1):49-63.

111.   Kurz EU, Lees-Miller SP. DNA damage-induced activation of ATM and ATM-dependent signaling pathways. DNA repair. 2004;3(8):889-900.

112.   Schuler M, Green D. Mechanisms of p53-dependent apoptosis. Portland Press Limited; 2001.

113.   Oda E, Ohki R, Murasawa H, Nemoto J, Shibue T, Yamashita T, et al. Noxa, a BH3-only member of the Bcl-2 family and candidate mediator of p53-induced apoptosis. Science. 2000;288(5468):1053-8.

114.   Liu F-T, Newland AC, Jia L. Bax conformational change is a crucial step for PUMA-mediated apoptosis in human leukemia. Biochemical and biophysical research communications. 2003;310(3):956-62.

115. Tait SW, Green DR. Mitochondria and cell death: outer membrane permeabilization and beyond. Nature reviews Molecular cell biology. 2010;11(9):621-32.

116.   Chinnaiyan AM. The apoptosome: heart and soul of the cell death machine. Neoplasia. 1999;1(1):5-15.

117.   Newmeyer D, Bossy-Wetzel E, Kluck R, Wolf B, Beere H, Green D. Bcl-xL does not inhibit the function of Apaf-1. Cell death and differentiation. 2000;7(4):402.

118.   Ashkenazi A, Dixit VM. Death receptors: signaling and modulation. Science. 1998;281(5381):1305-8.

119.   Wajant H. The Fas signaling pathway: more than a paradigm. Science. 2002;296(5573):1635-6.

120.   Kischkel F, Hellbardt S, Behrmann I, Germer M, Pawlita M, Krammer P, et al. Cytotoxicity-dependent APO-1 (Fas/CD95)-associated proteins form a death-inducing signaling complex (DISC) with the receptor. The EMBO journal. 1995;14(22):5579.

121.   Slee EA, Adrain C, Martin SJ. Executioner caspase-3,-6, and-7 perform distinct, non-redundant roles during the demolition phase of apoptosis. Journal of biological Chemistry. 2001;276(10):7320-6.

122.   Kroemer G, Galluzzi L, Brenner C. Mitochondrial membrane permeabilization in cell death. Physiological reviews. 2007;87(1):99-163.

123.   Galluzzi L, Zamzami N, de La Motte Rouge T, Lemaire C, Brenner C, Kroemer G. Methods for the assessment of mitochondrial membrane permeabilization in apoptosis. Apoptosis. 2007;12(5):803-13.

124.   Martin S, Reutelingsperger C, McGahon AJ, Rader JA, Van Schie R, LaFace DM, et al. Early redistribution of plasma membrane phosphatidylserine is a general feature of apoptosis regardless of the initiating stimulus: inhibition by overexpression of Bcl-2 and Abl. Journal of Experimental Medicine. 1995;182(5):1545-56.

125.   Goldstein JC, Waterhouse NJ, Juin P, Evan GI, Green DR. The coordinate release of cytochrome c during apoptosis is rapid, complete and kinetically invariant. Nature cell biology. 2000;2(3):156-62.

126.   Zamzami N, Marchetti P, Castedo M, Decaudin D, Macho A, Hirsch T, et al. Sequential reduction of mitochondrial transmembrane potential and generation of reactive oxygen species in early programmed cell death. Journal of Experimental Medicine. 1995;182(2):367-77.

127.   Berg J, Hung YP, Yellen G. A genetically encoded fluorescent reporter of ATP: ADP ratio. Nature methods. 2009;6(2):161-6.

128.   Imamura H, Nhat KPH, Togawa H, Saito K, Iino R, Kato-Yamada Y, et al. Visualization of ATP levels inside single living cells with fluorescence resonance energy transfer-based genetically encoded indicators. Proceedings of the National Academy of Sciences. 2009;106(37):15651-6.

129.   Berridge MV, Herst PM, Tan AS. Tetrazolium dyes as tools in cell biology: new insights into their cellular reduction. Biotechnology annual review. 2005;11:127-52.

130. Tyas L, Brophy VA, Pope A, Rivett AJ, Tavaré JM. Rapid caspase-3 activation during apoptosis revealed using fluorescence-resonance energy transfer. EMBO reports. 2000;1(3):266-70.

131. Shimizu S, Kanaseki T, Mizushima N, Mizuta T, Arakawa-Kobayashi S, Thompson CB, et al. Role of Bcl-2 family proteins in a non-apoptotic programmed cell death dependent on autophagy genes. Nature cell biology. 2004;6(12):1221-8.

132. Hara T, Nakamura K, Matsui M, Yamamoto A, Nakahara Y, Suzuki-Migishima R, et al. Suppression of basal autophagy in neural cells causes neurodegenerative disease in mice. Nature. 2006;441(7095):885-9.

133. Mizushima N, Levine B. Autophagy in mammalian development and differentiation. Nature cell biology. 2010;12(9):823-30.

134. Xie Z, Klionsky DJ. Autophagosome formation: core machinery and adaptations. Nature cell biology. 2007;9(10):1102-9.

135. Pankiv S, Clausen TH, Lamark T, Brech A, Bruun J-A, Outzen H, et al. p62/SQSTM1 binds directly to Atg8/LC3 to facilitate degradation of ubiquitinated protein aggregates by autophagy. Journal of biological Chemistry. 2007;282(33):24131-45.

136. Kimura S, Fujita N, Noda T, Yoshimori T. Monitoring autophagy in mammalian cultured cells through the dynamics of LC3. Methods in enzymology. 2009;452:1-12.

137. Lipinski MM, Hoffman G, Ng A, Zhou W, Py BF, Hsu E, et al. A genome-wide siRNA screen reveals multiple mTORC1 independent signaling pathways regulating autophagy under normal nutritional conditions. Developmental cell. 2010;18(6):1041-52.

138. Hoffman GR, Moerke NJ, Hsia M, Shamu CE, Blenis J. A high-throughput, cell-based screening method for siRNA and small molecule inhibitors of mTORC1 signaling using the In Cell Western technique. Assay and drug development technologies. 2010;8(2):186-99.

139. Sawai H, Domae N. Discrimination between primary necrosis and apoptosis by necrostatin-1 in Annexin V-positive/propidium iodide-negative cells. Biochemical and biophysical research communications. 2011;411(3):569-73.

140. Galluzzi L, Kroemer G. Necroptosis: a specialized pathway of programmed necrosis. Cell. 2008;135(7):1161-3.

141. Jorgensen I, Rayamajhi M, Miao EA. Programmed cell death as a defence against infection. Nature Reviews Immunology. 2017.

142. Savill J, Fadok V. Corpse clearance defines the meaning of cell death. Nature. 2000;407(6805):784-8.

143. Silva MT. Secondary necrosis: the natural outcome of the complete apoptotic program. FEBS letters. 2010;584(22):4491-9.

144. Scaffidi P, Misteli T, Bianchi ME. Release of chromatin protein HMGB1 by necrotic cells triggers inflammation. Nature. 2002;418(6894):191-5.

145. Christofferson DE, Yuan J. Cyclophilin A release as a biomarker of necrotic cell death. Cell death and differentiation. 2010;17(12):1942.

146. Li J, Zhang J, Chen J, Luo X, Zhu W, Shen J, et al. Strategy for discovering chemical inhibitors of human cyclophilin A: focused library design, virtual screening, chemical synthesis and bioassay. Journal of combinatorial chemistry. 2006;8(3):326-37.

147. Arcamone F, Cassinelli G, Fantini G, Grein A, Orezzi P, Pol C, et al. Adriamycin, 14-hydroxydaimomycin, a new antitumor antibiotic from S. Peucetius var. caesius. Biotechnology and bioengineering. 1969;11(6):1101-10.

148. Thorn CF, Oshiro C, Marsh S, Hernandez-Boussard T, McLeod H, Klein TE, et al. Doxorubicin pathways: pharmacodynamics and adverse effects. Pharmacogenetics and genomics. 2011;21(7):440.

149.   Florea A-M, Büsselberg D. Cisplatin as an anti-tumor drug: cellular mechanisms of activity, drug resistance and induced side effects. Cancers. 2011;3(1):1351-71.

150.   Shen D-W, Pouliot LM, Hall MD, Gottesman MM. Cisplatin resistance: a cellular self-defense mechanism resulting from multiple epigenetic and genetic changes. Pharmacological reviews. 2012;64(3):706-21.

151.   Paul I, Chacko A, Stasik I, Busacca S, Crawford N, McCoy F, et al. Acquired differential regulation of caspase-8 in cisplatin-resistant non-small-cell lung cancer. Cell death & disease. 2012;3(12):e449.

152.   Stegehuis J, De Wilt L, De Vries E, Groen H, De Jong S, Kruyt F. TRAIL receptor targeting therapies for non-small cell lung cancer: current status and perspectives. Drug resistance updates. 2010;13(1):2-15.

153.   Raman CV, Krishnan KS. A new type of secondary radiation. Nature. 1928;121(3048):501-2.

154.   Masters BR. CV Raman and the Raman effect. Optics and Photonics News. 2009;20(3):40-5.

155.   Maiman TH. Stimulated optical radiation in ruby. Nature. 1960;187(4736):493-4.

156.   Krishnan R, Shankar R. Raman effect: History of the discovery. Journal of Raman Spectroscopy. 1981;10(1):1-8.

157.   Optical O. Raman Spectroscopy. 2017.

158.   Smekal A. Zur quantentheorie der dispersion. Naturwissenschaften. 1923;11(43):873-5.

159.   Brauchle E, Schenke-Layland K. Raman spectroscopy in biomedicine–non-invasive in vitro analysis of cells and extracellular matrix components in tissues. Biotechnol J. 2013;8(3):288-97.

160. Pahlow S, Meisel S, Cialla-May D, Weber K, Rösch P, Popp J. Isolation and identification of bacteria by means of Raman spectroscopy. Advanced drug delivery reviews. 2015;89:105-20.

161. Stöckel S, Kirchhoff J, Neugebauer U, Rösch P, Popp J. The application of Raman spectroscopy for the detection and identification of microorganisms. Journal of Raman Spectroscopy. 2016;47(1):89-109.

162. Kloß S, Rösch P, Pfister W, Kiehntopf M, Popp Jr. Toward culture-free Raman spectroscopic identification of pathogens in ascitic fluid. Analytical chemistry. 2014;87(2):937-43.

163. Espagnon I, Ostrovskii D, Mathey R, Dupoy M, Joly PL, Novelli-Rousseau A, et al. Direct identification of clinically relevant bacterial and yeast microcolonies and macrocolonies on solid culture media by Raman spectroscopy. Journal of biomedical optics. 2014;19(2):027004-.

164. Almarashi JF, Kapel N, Wilkinson TS, Telle HH. Raman spectroscopy of bacterial species and strains cultivated under reproducible conditions. Journal of Spectroscopy. 2012;27(5-6):361-5.

165. Stöckel S, Meisel S, Elschner M, Rosch P, Popp J. Identification of Bacillus anthracis via Raman spectroscopy and chemometric approaches. Analytical chemistry. 2012;84(22):9873-80.

166. Kong K, Kendall C, Stone N, Notingher I. Raman spectroscopy for medical diagnostics—From in-vitro biofluid assays to in-vivo cancer detection. Advanced drug delivery reviews. 2015;89:121-34.

167. Austin LA, Osseiran S, Evans CL. Raman technologies in cancer diagnostics. Analyst. 2016;141(2):476-503.

168. Kourkoumelis N, Balatsoukas I, Moulia V, Elka A, Gaitanis G, Bassukas ID. Advances in the in vivo Raman spectroscopy of malignant skin tumors using portable instrumentation. International journal of molecular sciences. 2015;16(7):14554-70.

169. Popp J, Windbergs M. Preface: Pharmaceutical applications of Raman spectroscopy—From diagnosis to therapeutics. Advanced drug delivery reviews. 2015(89):1-2.

170. Bergner N, Medyukhina A, Geiger KD, Kirsch M, Schackert G, Krafft C, et al. Hyperspectral unmixing of Raman micro-images for assessment of morphological and chemical parameters in non-dried brain tumor specimens. Analytical and bioanalytical chemistry. 2013;405(27):8719-28.

171. Haka AS, Shafer-Peltier KE, Fitzmaurice M, Crowe J, Dasari RR, Feld MS. Diagnosing breast cancer by using Raman spectroscopy. Proceedings of the National Academy of Sciences of the United States of America. 2005;102(35):12371-6.

172. Stone N, Matousek P. Advanced transmission Raman spectroscopy: a promising tool for breast disease diagnosis. Cancer research. 2008;68(11):4424-30.

173. Yang Y, Li F, Gao L, Wang Z, Thrall MJ, Shen SS, et al. Differential diagnosis of breast cancer using quantitative, label-free and molecular vibrational imaging. Biomedical optics express. 2011;2(8):2160-74.

174. Magee ND, Beattie JR, Carland C, Davis R, McManus K, Bradbury I, et al. Raman microscopy in the diagnosis and prognosis of surgically resected nonsmall cell lung cancer. Journal of biomedical optics. 2010;15(2):026015.

175. Lieber CA, Majumder SK, Ellis DL, Billheimer DD, Mahadevan-Jansen A. In vivo nonmelanoma skin cancer diagnosis using Raman microspectroscopy. Lasers in surgery and medicine. 2008;40(7):461-7.

176. Crow P, Stone N, Kendall C, Uff J, Farmer J, Barr H, et al. The use of Raman spectroscopy to identify and grade prostatic adenocarcinoma in vitro. British journal of cancer. 2003;89(1):106.

177. Huang Z, McWilliams A, Lui H, McLean DI, Lam S, Zeng H. Near-infrared Raman spectroscopy for optical diagnosis of lung cancer. International journal of cancer. 2003;107(6):1047-52.

178. McGregor HC, Short MA, McWilliams A, Shaipanich T, Ionescu DN, Zhao J, et al. Real-time endoscopic Raman spectroscopy for in vivo early lung cancer detection. Journal of biophotonics. 2017;10(1):98-110.

179. Notingher I, Verrier S, Haque S, Polak J, Hench L. Spectroscopic study of human lung epithelial cells (A549) in culture: living cells versus dead cells. Biopolymers. 2003;72(4):230-40.

180. Notingher I, Hench LL. Raman microspectroscopy: a noninvasive tool for studies of individual living cells in vitro. Expert review of medical devices. 2006;3(2):215-34.

181. Kunapareddy N, Freyer JP, Mourant JR. Raman spectroscopic characterization of necrotic cell death. Journal of biomedical optics. 2008;13(5):054002--9.

182. Okada M, Smith NI, Palonpon AF, Endo H, Kawata S, Sodeoka M, et al. Label-free Raman observation of cytochrome c dynamics during apoptosis. Proceedings of the National Academy of Sciences. 2012;109(1):28-32.

183. Notingher I, Green C, Dyer C, Perkins E, Hopkins N, Lindsay C, et al. Discrimination between ricin and sulphur mustard toxicity in vitro using Raman spectroscopy. Journal of the Royal Society Interface. 2004;1(1):79-90.

184. Ong YH, Lim M, Liu Q. Comparison of principal component analysis and biochemical component analysis in Raman spectroscopy for the discrimination of apoptosis and necrosis in K562 leukemia cells. Optics express. 2012;20(20):22158-71.

185.   Pyrgiotakis G, Kundakcioglu OE, Finton K, Pardalos PM, Powers K, Moudgil BM. Cell death discrimination with Raman spectroscopy and support vector machines. Annals of biomedical engineering. 2009;37(7):1464-73.

186.   Brauchle E, Thude S, Brucker SY, Schenke-Layland K. Cell death stages in single apoptotic and necrotic cells monitored by Raman microspectroscopy. Scientific reports. 2014;4.

187.   Notingher I, Verrier S, Romanska H, Bishop A, Polak J, Hench L. In situ characterisation of living cells by Raman spectroscopy. Journal of Spectroscopy. 2002;16(2):43-51.

188.   Parekh SH, Lee YJ, Aamer KA, Cicerone MT. Label-free cellular imaging by broadband coherent anti-Stokes Raman scattering microscopy. Biophysical journal. 2010;99(8):2695-704.

189.   Zumbusch A, Holtom GR, Xie XS. Three-dimensional vibrational imaging by coherent anti-Stokes Raman scattering. Physical review letters. 1999;82(20):4142.

190.   Krafft C, Dietzek B, Popp J. Raman and CARS microspectroscopy of cells and tissues. Analyst. 2009;134(6):1046-57.

191.   Evans CL, Potma EO, Puoris' haag M, Côté D, Lin CP, Xie XS. Chemical imaging of tissue in vivo with video-rate coherent anti-Stokes Raman scattering microscopy. Proceedings of the National Academy of Sciences of the United States of America. 2005;102(46):16807-12.

192.   Le TT, Huff TB, Cheng J-X. Coherent anti-Stokes Raman scattering imaging of lipids in cancer metastasis. BMC cancer. 2009;9(1):42.

193.   Gao L, Zhou H, Thrall MJ, Li F, Yang Y, Wang Z, et al. Label-free high-resolution imaging of prostate glands and cavernous nerves using coherent anti-Stokes Raman scattering microscopy. Biomedical optics express. 2011;2(4):915-26.

194.   Schuster KC, Reese I, Urlaub E, Gapes JR, Lendl B. Multidimensional information on the chemical composition of single bacterial cells by confocal Raman microspectroscopy. Analytical chemistry. 2000;72(22):5529-34.

195.   Majzner K, Kaczor A, Kachamakova-Trojanowska N, Fedorowicz A, Chlopicki S, Baranska M. 3D confocal Raman imaging of endothelial cells and vascular wall: perspectives in analytical spectroscopy of biomedical research. Analyst. 2013;138(2):603-10.

196.   Caspers P, Lucassen G, Puppels G. Combined in vivo confocal Raman spectroscopy and confocal microscopy of human skin. Biophysical journal. 2003;85(1):572-80.

197.   Choi J, Choo J, Chung H, Gweon DG, Park J, Kim HJ, et al. Direct observation of spectral differences between normal and basal cell carcinoma (BCC) tissues using confocal Raman microscopy. Biopolymers. 2005;77(5):264-72.

198.   Yu C, Gestl E, Eckert K, Allara D, Irudayaraj J. Characterization of human breast epithelial cells by confocal Raman microspectroscopy. Cancer detection and prevention. 2006;30(6):515-22.

199.   Haka AS, Shafer-Peltier KE, Fitzmaurice M, Crowe J, Dasari RR, Feld MS. Identifying microcalcifications in benign and malignant breast lesions by probing differences in their chemical composition using Raman spectroscopy. Cancer research. 2002;62(18):5375-80.

200.   Morris MD, Matousek P, Towrie M, Parker AW, Goodship AE, Draper ER. Kerr-gated time-resolved Raman spectroscopy of equine cortical bone tissue. Journal of biomedical optics. 2005;10(1):014014-0140147.

201.   Prieto MCH, Matousek P, Towrie M, Parker AW, Wright M, Ritchie AW, et al. Use of picosecond Kerr-gated Raman spectroscopy to suppress signals from both surface and deep layers in bladder and prostate tissue. Journal of biomedical optics. 2005;10(4):044006--6.

202. Baker R, Matousek P, Ronayne KL, Parker AW, Rogers K, Stone N. Depth profiling of calcifications in breast tissue using picosecond Kerr-gated Raman spectroscopy. Analyst. 2007;132(1):48-53.

203. Xie C, Li Y-q. Confocal micro-Raman spectroscopy of single biological cells using optical trapping and shifted excitation difference techniques. Journal of Applied Physics. 2003;93(5):2982-6.

204. Sowoidnich K, Kronfeldt H-D. Fluorescence rejection by shifted excitation Raman difference spectroscopy at multiple wavelengths for the investigation of biological samples. ISRN Spectroscopy. 2012;2012.

205. da Silva Martins MA, Ribeiro DG, dos Santos EAP, Martin AA, Fontes A, da Silva Martinho H. Shifted-excitation Raman difference spectroscopy for in vitro and in vivo biological samples analysis. Biomedical optics express. 2010;1(2):617-26.

206. Krafft C, Neudert L, Simat T, Salzer R. Near infrared Raman spectra of human brain lipids. Spectrochimica Acta Part A: Molecular and Biomolecular Spectroscopy. 2005;61(7):1529-35.

207. Matousek P, Stone N. Prospects for the diagnosis of breast cancer by noninvasive probing of calcifications using transmission Raman spectroscopy. Journal of biomedical optics. 2007;12(2):024008--8.

208. Keller MD, Vargis E, de Matos Granja N, Wilson RH, Mycek M-A, Kelley MC, et al. Development of a spatially offset Raman spectroscopy probe for breast tumor surgical margin evaluation. Journal of biomedical optics. 2011;16(7):077006--8.

209. Ma K, Yuen JM, Shah NC, Walsh Jr JT, Glucksberg MR, Van Duyne RP. In vivo, transcutaneous glucose sensing using surface-enhanced spatially offset Raman spectroscopy: multiple rats, improved hypoglycemic accuracy, low incident power, and continuous monitoring for greater than 17 days. Analytical chemistry. 2011;83(23):9146-52.

210. Yuen JM, Shah NC, Walsh Jr JT, Glucksberg MR, Van Duyne RP. Transcutaneous glucose sensing by surface-enhanced spatially offset Raman spectroscopy in a rat model. Analytical chemistry. 2010;82(20):8382-5.

211. Xie Hn, Stevenson R, Stone N, Hernandez-Santana A, Faulds K, Graham D. Tracking Bisphosphonates through a 20 mm Thick Porcine Tissue by Using Surface-Enhanced Spatially Offset Raman Spectroscopy. Angewandte Chemie International Edition. 2012;51(34):8509-11.

212. Sharma B, Ma K, Glucksberg MR, Van Duyne RP. Seeing through bone with surface-enhanced spatially offset Raman spectroscopy. Journal of the American Chemical Society. 2013;135(46):17290-3.

213. Zhang X, Roeffaers MB, Basu S, Daniele JR, Fu D, Freudiger CW, et al. Label-Free Live-Cell Imaging of Nucleic Acids Using Stimulated Raman Scattering Microscopy. ChemPhysChem. 2012;13(4):1054-9.

214. Albrecht MG, Creighton JA. Anomalously intense Raman spectra of pyridine at a silver electrode. Journal of the American Chemical Society. 1977;99(15):5215-7.

215. Kreibig U, Vollmer M. Cluster materials. Springer-Verlag: Heidelberg, Germany; 1995.

216. Maier SA. Plasmonics: fundamentals and applications: Springer Science & Business Media; 2007.

217. Hutter E, Fendler JH. Exploitation of localized surface plasmon resonance. Advanced materials. 2004;16(19):1685-706.

218. Underwood S, Mulvaney P. Effect of the solution refractive index on the color of gold colloids. Langmuir. 1994;10(10):3427-30.

219. Mulvaney P. Surface plasmon spectroscopy of nanosized metal particles. Langmuir. 1996;12(3):788-800.

220.   Link S, El-Sayed MA. Size and temperature dependence of the plasmon absorption of colloidal gold nanoparticles. The Journal of Physical Chemistry B. 1999;103(21):4212-7.

221.   McFarland AD, Young MA, Dieringer JA, Van Duyne RP. Wavelength-scanned surface-enhanced Raman excitation spectroscopy. The Journal of Physical Chemistry B. 2005;109(22):11279-85.

222.   Sharma B, Frontiera RR, Henry A-I, Ringe E, Van Duyne RP. SERS: materials, applications, and the future. Materials today. 2012;15(1):16-25.

223.   Kosuda K, Bingham J, Wustholz K, Van Duyne R. Nanostructures and surface-enhanced Raman spectroscopy. Handbook of Nanoscale Optics and Electronics. 2010:309.

224.   Grasseschi D, Toma HE. The SERS effect in coordination chemistry. Coordination Chemistry Reviews. 2016.

225.   Kelly KL, Coronado E, Zhao LL, Schatz GC. The optical properties of metal nanoparticles: the influence of size, shape, and dielectric environment. ACS Publications; 2003.

226.   Haynes CL, Van Duyne RP. Plasmon-sampled surface-enhanced Raman excitation spectroscopy. The Journal of Physical Chemistry B. 2003;107(30):7426-33.

227.   Nie S, Emory SR. Probing single molecules and single nanoparticles by surface-enhanced Raman scattering. Science. 1997;275(5303):1102-6.

228.   Sharma B, Cardinal MF, Kleinman SL, Greeneltch NG, Frontiera RR, Blaber MG, et al. High-performance SERS substrates: Advances and challenges. MRS bulletin. 2013;38(08):615-24.

229.   McNay G, Eustace D, Smith WE, Faulds K, Graham D. Surface-enhanced Raman scattering (SERS) and surface-enhanced resonance Raman scattering (SERRS): a review of applications. Applied Spectroscopy. 2011;65(8):825-37.

230. Haynes CL, McFarland AD, Duyne RPV. Surface-enhanced Raman spectroscopy. ACS Publications; 2005.

231. Le Ru E, Etchegoin P. Principles of Surface-Enhanced Raman Spectroscopy: and related plasmonic effects: Elsevier; 2008.

232. Vendrell M, Maiti KK, Dhaliwal K, Chang Y-T. Surface-enhanced Raman scattering in cancer detection and imaging. Trends in biotechnology. 2013;31(4):249-57.

233. Kneipp J. Interrogating Cells, Tissues, and Live Animals with New Generations of Surface-Enhanced Raman Scattering Probes and Labels. Acs Nano. 2017;11(2):1136-41.

234. Jaworska A, Wojcik T, Malek K, Kwolek U, Kepczynski M, Ansary AA, et al. Rhodamine 6G conjugated to gold nanoparticles as labels for both SERS and fluorescence studies on live endothelial cells. Microchimica Acta. 2015;182(1-2):119-27.

235. Jaworska A, Jamieson LE, Malek K, Campbell CJ, Choo J, Chlopicki S, et al. SERS-based monitoring of the intracellular pH in endothelial cells: the influence of the extracellular environment and tumour necrosis factor-α. Analyst. 2015;140(7):2321-9.

236. Fujita K, Ishitobi S, Hamada K, Smith NI, Taguchi A, Inouye Y, et al. Time-resolved observation of surface-enhanced Raman scattering from gold nanoparticles during transport through a living cell. Journal of biomedical optics. 2009;14(2):024038--7.

237. Nabiev I, Morjani H, Manfait M. Selective analysis of antitumor drug interaction with living cancer cells as probed by surface-enhanced Raman spectroscopy. European biophysics journal. 1991;19(6):311-6.

238. Kneipp K, Wang Y, Kneipp H, Perelman LT, Itzkan I, Dasari RR, et al. Single molecule detection using surface-enhanced Raman scattering (SERS). Physical review letters. 1997;78(9):1667.

239. Fujita K, Ando J, Ishitobi S, Hamada K, Smith NI, Inouye Y, et al., editors. Observation of living cells with gold nanoparticles by using surface-enhanced Raman

scattering. SPIE BiOS: Biomedical Optics; 2009: International Society for Optics and Photonics.

240. Fujitaa K, Andoa J, Smithb NI, Kawataa S, editors. Dynamic SERS imaging with gold nanoparticles transported in a living cell. Proc of SPIE Vol; 2013.

241. Ando J, Fujita K, Smith NI, Kawata S. Dynamic SERS imaging of cellular transport pathways with endocytosed gold nanoparticles. Nano letters. 2011;11(12):5344-8.

242. Huefner A, Kuan W-L, Müller KH, Skepper JN, Barker RA, Mahajan S. Characterization and Visualization of Vesicles in the Endo-Lysosomal Pathway with Surface-Enhanced Raman Spectroscopy and Chemometrics. Acs Nano. 2015;10(1):307-16.

243. Kang B, Austin LA, El-Sayed MA. Observing real-time molecular event dynamics of apoptosis in living cancer cells using nuclear-targeted plasmonically enhanced Raman nanoprobes. Acs Nano. 2014;8(5):4883-92.

244. Ali MR, Wu Y, Han T, Zang X, Xiao H, Tang Y, et al. Simultaneous Time-Dependent Surface-Enhanced Raman Spectroscopy, Metabolomics, and Proteomics Reveal Cancer Cell Death Mechanisms Associated with Gold Nanorod Photothermal Therapy. Journal of the American Chemical Society. 2016;138(47):15434-42.

245. Panikkanvalappil SR, Hira SM, Mahmoud MA, El-Sayed MA. Unraveling the biomolecular snapshots of mitosis in healthy and cancer cells using plasmonically-enhanced Raman spectroscopy. Journal of the American Chemical Society. 2014;136(45):15961-8.

246. Panikkanvalappil SR, Hira SM, El-Sayed MA. Elucidation of ultraviolet radiation-induced cell responses and intracellular biomolecular dynamics in mammalian cells using surface-enhanced Raman spectroscopy. Chemical Science. 2016;7(2):1133-41.

247. Panikkanvalappil SR, James M, Hira SM, Mobley J, Jilling T, Ambalavanan N, et al. Hyperoxia Induces Intracellular Acidification in Neonatal Mouse Lung Fibroblasts:

Real-Time Investigation Using Plasmonically Enhanced Raman Spectroscopy. Journal of the American Chemical Society. 2016;138(11):3779-88.

248.	Büchner T, Drescher D, Merk V, Traub H, Guttmann P, Werner S, et al. Biomolecular environment, quantification, and intracellular interaction of multifunctional magnetic SERS nanoprobes. Analyst. 2016;141(17):5096-106.

249.	Yu KN, Lee S-M, Han JY, Park H, Woo M-A, Noh MS, et al. Multiplex targeting, tracking, and imaging of apoptosis by fluorescent surface enhanced Raman spectroscopic dots. Bioconjugate chemistry. 2007;18(4):1155-62.

250.	Jiang X, Jiang Z, Xu T, Su S, Zhong Y, Peng F, et al. Surface-enhanced Raman scattering-based sensing in vitro: facile and label-free detection of apoptotic cells at the single-cell level. Analytical chemistry. 2013;85(5):2809-16.

251.	El-Said WA, Kim T-H, Kim H, Choi J-W. Analysis of intracellular state based on controlled 3D nanostructures mediated surface enhanced Raman scattering. PloS one. 2011;6(2):e15836.

252.	Jin Q, Li M, Polat B, Paidi SK, Dai A, Zhang A, et al. Mechanical Trap Surface-Enhanced Raman Spectroscopy for Three-Dimensional Surface Molecular Imaging of Single Live Cells. Angewandte Chemie. 2017;129(14):3880-4.

253.	Vitol EA, Orynbayeva Z, Bouchard MJ, Azizkhan-Clifford J, Friedman G, Gogotsi Y. In situ intracellular spectroscopy with surface enhanced Raman spectroscopy (SERS)-enabled nanopipettes. Acs Nano. 2009;3(11):3529-36.

254.	Turkevich J, Stevenson PC, Hillier J. A study of the nucleation and growth processes in the synthesis of colloidal gold. Discussions of the Faraday Society. 1951;11:55-75.

255.	Kuku G, Saricam M, Akhatova F, Danilushkina A, Fakhrullin R, Culha M. Surface-enhanced Raman scattering to evaluate nanomaterial cytotoxicity on living cells. Analytical chemistry. 2016;88(19):9813-20.

256.   Glauert AM, Glauert R. Araldite as an embedding medium for electron microscopy. The Journal of biophysical and biochemical cytology. 1958;4(2):191-4.

257.   Reynolds ES. The use of lead citrate at high pH as an electron-opaque stain in electron microscopy. The Journal of cell biology. 1963;17(1):208.

258.   Adar F, Lee E, Mamedov S, Whitley A. Experimental evaluation of the depth resolution of a Raman microscope. Microsc Microanal. 2010;16(2):361.

259.   El-Sayed IH, Huang X, El-Sayed MA. Surface plasmon resonance scattering and absorption of anti-EGFR antibody conjugated gold nanoparticles in cancer diagnostics: applications in oral cancer. Nano letters. 2005;5(5):829-34.

260.   Draux F, Jeannesson P, Beljebbar A, Tfayli A, Fourre N, Manfait M, et al. Raman spectral imaging of single living cancer cells: a preliminary study. Analyst. 2009;134(3):542-8.

261.   Creely CM, Volpe G, Singh GP, Soler M, Petrov DV. Raman imaging of floating cells. Optics express. 2005;13(16):6105-10.

262.   Swain R, Stevens M. Raman microspectroscopy for non-invasive biochemical analysis of single cells. Portland Press Limited; 2007.

263.   Zoladek A, Pascut FC, Patel P, Notingher I. Non-invasive time-course imaging of apoptotic cells by confocal Raman micro-spectroscopy. Journal of Raman Spectroscopy. 2011;42(3):251-8.

264.   Moss D. Biomedical Applications of Synchrotron Infrared Microspectroscopy: A Practical Approach: Royal Society of Chemistry; 2011.

265.   Butler HJ, Ashton L, Bird B, Cinque G, Curtis K, Dorney J, et al. Using Raman spectroscopy to characterize biological materials. Nature protocols. 2016;11(4):664-87.

266. Chithrani BD, Chan WC. Elucidating the mechanism of cellular uptake and removal of protein-coated gold nanoparticles of different sizes and shapes. Nano lett. 2007;7(6):1542-50.

267. Chen Y, Bai X, Su L, Du Z, Shen A, Materny A, et al. Combined labelled and label-free SERS probes for triplex three-dimensional cellular imaging. Scientific reports. 2016;6:19173.

268. Pálfy M, Reményi A, Korcsmáros T. Endosomal crosstalk: meeting points for signaling pathways. Trends in cell biology. 2012;22(9):447-56.

269. Liang L, Huang D, Wang H, Li H, Xu S, Chang Y, et al. In situ surface-enhanced raman scattering spectroscopy exploring molecular changes of drug-treated cancer cell nucleus. Analytical chemistry. 2015;87(4):2504-10.

270. Repnik U, Česen MH, Turk B. The endolysosomal system in cell death and survival. Cold Spring Harbor perspectives in biology. 2013;5(1):a008755.

271. Johansson A-C, Appelqvist H, Nilsson C, Kågedal K, Roberg K, Öllinger K. Regulation of apoptosis-associated lysosomal membrane permeabilization. Apoptosis. 2010;15(5):527-40.

272. Cui X, Dini S, Dai S, Bi J, Binder B, Green J, et al. A mechanistic study on tumour spheroid formation in thermosensitive hydrogels: experiments and mathematical modelling. RSC Advances. 2016;6(77):73282-91.

273. Gong X, Lin C, Cheng J, Su J, Zhao H, Liu T, et al. Generation of multicellular tumor spheroids with microwell-based agarose scaffolds for drug testing. PloS one. 2015;10(6):e0130348.